Energetic descriptors of steric hindrance in real space: an improved IQA picture †

Miguel Gallegos González[a], Aurora Costales Castro[a,*], Ángel Martín Pendás[a,*]

[a]*Department of Analytical and Physical Chemistry, University of Oviedo, E-33006, Oviedo, Spain.*

Abstract

Steric hindrance (SH) plays a central role in the modern chemical narrative, lying at the core of chemical intuition. As it however happens with many successful *chemical concepts*, SH lacks an underlying physically sound root, and multiple mutually inconsistent approximations have been devised to relate this fuzzy concept to computationally derivable descriptors. We here argue that being SH related to spatial as well as energetic features of interacting systems, SH can be properly handled if we chose a real space energetic stance like the Interacting Quantum Atoms (IQA) approach. Drawing on previous work by Popelier and coworkers (*ChemistryOpen* **8**, 560, 2019) we build an energetic estimator of SH, referred to as E_{ST}. We show that the rise in the self-energy of a fragment that accompanies steric congestion is a faithful proxy for the chemist's SH concept if we remove the effect of charge transfer. This can be done rigorously, and the E_{ST} here defined provides correct sterics even for hydrogen atoms, where the plain use of deformation energies leads to non-chemical results. The applicability of E_{ST} is validated in several chemical scenarios, going from atomic compressions to archetypal S_N2 reactions. E_{ST} is shown to be a robust steric hindrance descriptor.

Keywords:

Steric repulsion, Quantum theory of atoms in molecules, Interacting quantum atoms

Introduction

Chemical intuition and steric hindrance.

Chemistry, being fundamentally an experimental science, has been extensively built from empirical laws. This fact has inevitably led to the proliferation of a wide variety of "chemical

*To whom correspondence should be addressed : Prof. Ángel Martín Pendás: ampendas@uniovi.es; Prof. Aurora Costales Castro: costalesmaria@uniovi.es

[0]† Electronic Supplementary Information (ESI) available

concepts", which are commonly used to explain and predict the outcome of chemical processes. These fuzzy principles, among which aromaticity, inductive effects or steric hindrance are included, are often understood as the core of the group of tools known as "chemical intuition", considered by many as the fundamental pillar of modern synthetic chemistry. Despite their success from a pragmatic point of view, most of these concepts are built on quicksand, lacking rigorous mathematical definitions, solid physical ground and, what is even more important, not relying on quantum mechanical observables. Their use may very easily lead to get the right answer for the wrong reason, which thereby limits our potential understanding of the nature of Chemistry.

One of these *chemical unicorns*[1] is steric hindrance (SH), a term that alludes to the repulsive interactions appearing among non-bonded atoms or fragments as their shape gets distorted when they get congested in the physical space. According to the IUPAC, [2] SH is defined as "those steric effects arising from crowding of substituents", while a steric effect is "the effect on a chemical or physical property experienced upon the introduction of substituents having different steric requirements". This circular argument makes obvious that steric repulsion lacks of a rigorous definition, being rather expressed in terms of its effects on a chemical process or reaction. Despite its undefined origin and underlying nature, the concept has nevertheless been widely employed, and a huge number of effects and trends in chemical reactivity are today understood with its help. [3–6]

An early example of the application of SH can be found in the development of *the strain theory* by Adolf von Baeyer back in 1885, [7] a model used to explain the stability of cycloalkanes in terms of the tension associated to their cyclic structures. Since then, steric congestion along with strain effects have been claimed to be the driving force of a wide variety of phenomena ranging from classic textbook examples of reactivity [8–10] to state-of-the-art developments in supra-molecular chemistry. [11–13] Some phenomena where SH has been invoked to play a major role include: the origin of the rotational barriers of alkanes and other derivatives, [14–17] the stability of conformers of cycloalkanes and macrocycles, [18, 19] the ligand ability towards metal centers, [20, 21] the trends in the reactivity of nucleophilic substitution and elimination reactions, [22, 23] the torsional barriers of biphenyls and their optically active derivatives, [24] the reactions between tertiary amines and boron derivatives, [25] the geometrical features of methyl like radicals, [26] the stability of cis-trans isomers, [27] the competition between the basicity and nucleophilicity of nucleophiles and stereo-preference and the selectivity of the active site of

enzymes or organic catalysts, [28] among others.

Sterics as a driving force of chemical phenomena

Many attempts have been made to understand and quantify the effects of steric repulsion through empirical rules and postulates. For instance, the role of SH in organic chemistry is adequately addressed by the *Newman's rule of six* or the Taft equation. [29, 30] They establish, in an analogous way to Hammett's equation, [31] a linear relation between the free energy change in a reaction and different chemical terms that include SH. Due to the success of these and other approaches, SH has been considered to be well understood for many years. In recent times, however, accentuated by the development of theoretical and computational chemistry, an increasing number of debates [32–35] questioning whether SH is the truly driving force behind these empirical observations have appeared. Such a conceptual pitfall would involve huge implications in the way that we, as chemists, understand the working principles of chemistry.

An archetypal example lies in the trends observed in the competition of the uni-molecular, S_N1, and bi-molecular, S_N2 nucleophilic substitution reactions as the reactive electrophilic center is modified. As the number or "size" of the substituents of the electrophilic center increases, the S_N1 reaction mechanism is favored over the S_N2 one. This phenomenon has been classically explained as a result of the increasing SH experienced by the reactants during the nucleophilic attack as the electrophile becomes more sterically crowded. Such a reasoning has been seriously questioned. Indeed, Fernández and coworkers [32] have suggested that electrostatic attraction, and not steric repulsion, determines the trend in the activation barriers found with the increasing size of the aliphatic substituent. This conclusion is in partial disagreement with Bickelhaupt and coworkers, [33] who explained that as atoms approach each other the new orbital overlaps force the appearance of Pauli repulsions that lead to the observed "steric effects".

The explanatory ability of SH has also been invoked to unveil the origin of the rotational and torsional barriers exhibited by different molecules, classically associated to steric repulsion between non-bonded groups. Such a textbook explanation has turned out controversial, resulting in quite a number of alternative models, [6, 34, 36, 37] Since no context-free definition of SH exists, these models often provide contradicting interpretations that depend on how steric repulsion is quantified. Some authors [6, 34, 36] have used natural bond order (NBO) analyses to propose that it is hyperconjugation which is actually responsible for the existence of a rotational barrier, while others [38] suggest that their origin in simple aliphatic systems lies in the

slight rigidity conferred to some rotatable bonds as a result of resonance-like effects. A proper understanding of the deep nature of rotational barriers is not a petty or academic issue, having become of great importance in rational molecular design. For instance, the large torsional rigidity of the biphenyl scaffold has transformed this simple molecule in one of the fundamental building blocks of modern ligands, paving the way to the synthesis of new derivatives with potential catalytic or optical activities. [39, 40] We mention, on passing, that a study of the rotational barrier of ethane which can be immediately restated in terms of the quantities that will be defined in this work[41] already hinted their usefulness as steric energy estimators years ago.

Steric hindrance under the magnifying glass of theoretical chemistry.

Considering the critical role that SH is claimed to play in experimental chemistry, a lot of effort has been put over the years to unravel and elucidate its origin from physically rigorous terms[42–44]. Actually, SH has been examined through almost any possible theoretical perspective: perturbation theory at large distances in its symmetry adapted flavor,[45] (SAPT) Fock space analyses as in the natural steric analysis within the NBO formalism,[46] or via energy decomposition procedures, both in orbital space like in the Energy Decomposition Analysis[47] (EDA) or in real space, like with the Interacting Quantum Atoms method[48] (IQA), to name just a few.

It is widely believed that SH is no more than a manifestation of the antisymmetry requirement that excludes two same-spin fermions from occupying the same spatial position. This leads to identify SH with what is sometimes known as Pauli repulsion, which is clearly but loosely linked to a kinetic energy rise,[49] but this identification does neither provide any insight on how to quantify SH or give any clue on how this effect crystallizes in actual energetic descriptors. In SAPT, for instance, the first order correction to the energy of two interacting fragments has two terms, one describing their mutual electrostatic interaction, E^1_{elst}, and the other (called the exchange term, E^1_{exch}) appearing from antisymmetry. Only the second is repulsive when two neutral closed-shells interact, thus being usually reported as the exchange-repulsion energy. Following this reasoning, in 1997 Badenhoop and coworkers[50] used the NBO analysis to study the origin of steric hindrance, and attributed it to the exchange electronic energy. In this natural steric analysis, energy terms are associated to Pauli exchange antisymmetry, and the steric repulsion is expressed as a sum of energy changes from individual NBOs. This suggests that

the classical picture of atom-atom repulsion is not totally accurate and that it is rather the whole N electron distribution that has to be taken into account to describe the steric exchange repulsion. These ideas have been widely used, e.g. to analyze torsional barriers [6, 34, 36] or the gauche effect in dihalogenated alkanes, [51] among others.

A large number of other theoretically inspired tools have appeared in the literature. These include, to name just a few, the concept of "quantum mechanical size" as proposed by Hollet and coworkers, [52] the steric charge and steric force estimators of steric hindrance based on von Weizsäcker's kinetic energy density in density functional theory, [53, 54] or the redefinition of steric energy on the basis of momentum densities by Alipour and coworkers. [55] As regards energy decomposition methods, a particularly interesting example is the Activation Strain Model (ASM) developed by Bickelhaupt and coworkers, [56, 57] which is conceptually equivalent to the Distortion-Interaction model originally proposed by Houk. [58, 59] The ASM/DI models are extremely simple conceptually, and have been extensively used in chemical reactivity. [60–62] They partition any molecular energy change into strain (E_{str}) and interaction contributions (E_{int}), the former accounting for the energy penalty due to the geometrical deformation suffered by the interacting chemical moieties, and the latter quantifying their mutual interaction energy.

The abundance of SH theoretical models talks about the far from trivial nature of the steric repulsion concept and calls for deeper conceptual analyses. We vividly recommend taking into account the always thoughtful comments of Eugen Schwarz. [49] As he has shown, a recurrent issue that is prone to logical traps, conceptual pitfalls and severe misunderstandings regards finding the *driving force* behind an observed phenomenon from the different additive terms in EDAs. Using the overall change suffered by a state function when we go from an initial to a final state without an explicit account of the path connecting them is particularly dangerous, since the response of the system to the perturbation easily overshoots.

This is the case of the EDA treatment of the rotation barrier of ethane.[34, 63] A plain comparison of the Pauli repulsion term as we go from the geometrically relaxed staggered to the geometrically relaxed eclipsed conformer results in smaller SH in the latter. Recognizing the considerable increase of the C-C bond length accompanying the process, the classical steric view can be recovered if the methyl group is rigidly rotated while maintaining the (short) staggered bond distance. An interpretation compatible with traditional chemical intuition is thus possible: as rotation starts and Pauli repulsion accumulates, the system responds back by increasing the C-C distance, which quickly decreases E_{Pauli}. At the final point, $\Delta E_{Pauli} < 0$ has overshot

and the role of SH cannot be recognized from its consideration. We stress here that this tale is satisfying, but by no means unique. It heavily relies on externally isolating driving forces and their relaxation mechanisms. We notice, nevertheless, that several unbiased procedures to tackle this problem have appeared, as in the relative energy gradient (REG) method,[64] or in the reaction force (RF) analyses.[65]

Steric hindrance has also been studied with real space techniques, which offer orbital invariant descriptors. In the framework of Quantum Chemical Topology (QCT), it was soon shown [35, 66] that many alleged *repulsive interactions* are actually characterized by the presence of bond critical points between the congested atoms. Since in the orthodox QCT view these points are linked to a net energetic stabilization, long-lasting debates have sparkled.[67–69] Provided that a consistent real space account of SH is only possible from a general energy partitioning technique, it is not surprising that the interacting quantum atoms (IQA)[48] technique has been used to find real space SH descriptors.

Actually, Popelier and coworkers have extensively studied [67, 70, 71] steric effects in a variety of chemical scenarios with IQA. In these works, the changes in the IQA energy components of several model systems were analyzed as the molecules were physically compressed. This revealed that it is the intra-atomic (E_{self}) energy term of a congested atom that clearly offers a potential estimator of SH. This is physically appealing, since ΔE_{self} has been shown to measure atomic promotion or atomic deformation.[72]

Moreover, ΔE_{self} was found to be easily modeled through a repulsive Buckingham potential [73] and to be mainly dominated by a kinetic energy rise, all in agreement with what is expected from a Pauli driven process. Though overall successful, this approach faced some difficulties when dealing with H atoms. More specifically, under some circumstances the compression of hydrogens results in a decrease, not an increase, of their self-energy. Such an anomalous behavior was already attributed by Popelier *et al* to charge transfer effects associated to the confinement process, since the lack of core electrons makes E^{H}_{self} particularly susceptible to them. Altogether, these results led the authors to conclude that hydrogen does not produce steric hindrance in a reliable way.

Our approximation

In full agreement with Popelier and coworkers,[67] we truly think that an energetic footprint of SH in real space lies in the IQA group or atomic deformation energies, $E_{def} = \Delta E_{self}$.

However, we expect to convincingly show in this contribution that only after charge transfer effects are properly discounted from E_{def}'s we do have a pure (or purer) steric energy descriptor. Interestingly, charge transfer can be rigorously extracted from E_{self} by appealing to the grand canonical behavior of atomic energies with electron count.[74]

After presenting our partitioning of E_{def} into charge transfer and steric contributions, we organize the work as follows: first, the effect of spatial confinement in the self energy of an atom, as modeled through an external parabolic potential, is compared to the deformations suffered by an actual system. After these insights we validate the reliability and applicability of the steric energy, using for such purpose a set of confined dimers paying special attention to the already mentioned case of H atoms. Finally, the utility of our approach in the field of chemical reactivity is examined through the exhaustive analysis of the classical self-substitution (S_N2) reaction between a halomethane (CH_3X) and a halide anion (X^-) for X = F, Cl, Br.

Steric Hindrance measures in the Real Space

The Interacting Quantum Atoms (IQA) approach is an energy decomposition scheme[48, 72] that writes exactly the molecular energy as a sum of intra- and interatomic terms after a fuzzy or exhaustive atomic partition of the physical space. The partition is invariant under orbital transformations and acquires its full meaning under the Quantum Theory of Atoms in Molecules (QTAIM) [75] umbrella, wherein the problematic domain kinetic energy terms are best defined. IQA needs only from the non-diagonal first order and the diagonal second order density matrices, and is thus available at any theoretical level where those matrices are well defined. DFT approximations have also been presented.[76, 77] Within IQA, the energy is written as

$$E = \sum_A E^A_{self} + \sum_{A>B} E^{AB}_{int}\,, \tag{1}$$

where E^A_{self} and E^{AB}_{int} correspond, respectively, to the intra-atomic energy (also referred to as the net. or self-energy) of atom A and the interaction energy between atoms A and B. E^A_{self} includes the kinetic energy of the electrons residing in A as well as their mutual repulsion (V^{AA}_{ee}) and attraction (V^{AA}_{en}) to its nucleus. Although we will not use them much, the interatomic interaction energy can be partitioned into chemically appealing ionic and a covalent terms. Since any union of QTAIM atom is also a QTAIM region, IQA can be immediately applied to general fragments composed of several atomic domains. The self-energy of a fragment includes

the self-energies of their constituting atoms as well as all their interatomic interactions.

As we will be dealing mainly with self-energies in this contribution, it is important to recognize that E^A_{self} tends to the variational isolated atomic or fragment energy when the fragment is fully detached (dissociated) from a molecule. In this sense, in the absence of other processes (see below), E^A_{self} increases as we allow A to interact with another moiety. ΔE^A_{self} is thus generally positive, and measures the *deformation* suffered by the fragment. As already stated, we call this change the deformation energy of the fragment, E^A_{def}:

$$E^A_{def} = E^A_{self} - E^A_{ref}, \tag{2}$$

where E_{ref} is the intra-atomic energy of the atom or fragment in the reference system (for instance, in vacuum). This is the rationale behind considering E^A_{def} as a proxy for steric hindrance.[70] For instance, if an isolated atom is subjected to physical confinement, its deformation energy will be truly quantifying its steric congestion.

Many different processes are known to contribute to E_{def}.[72] As a fragment gets confined, not only its electron distribution will compact itself. An excited state may well fall below the isolated ground solution. This is believed to lie behind many interesting metal to insulator (or vice versa) phase transitions in atomic solids.[78] The changes may affect the spin multiplicity, the basic electron configuration of the fragment, or both. When a fragment chemically interacts with another moiety, its Hilbert space expands, and its electron count ceases to be well-defined. Sometimes, the average electron number does not change (like when two equal atoms form a diatomic molecule), but the very presence of a fluctuating number of electrons in the region modifies necessarily its self-energy. In other more extreme cases, the interaction may lead to some electrons being almost fully transferred among regions.

Charge transfer has an enormous impact on the atomic or fragment self-energies. If a real space domain loses an electron, even if it is completely decoupled from the rest of the universe, its E_{self} will get destabilized by a quantity equal to its ionization energy, which is generally large. If, on the contrary, the moiety gains electrons, its E_{self} will get stabilized by its electron affinity. On losing electrons, a fragment's deformation energy will decrease steeply, even though the fragment is simultaneously subjected to a considerable steric clash. SH will thus be masked by charge transfer if measured through E_{def}, and charge transfer should be properly subtracted to build a SH descriptor that captures chemical intuition.

Fortunately, grand canonical density functional theory[79] has shown that, at zero temper-

ature, the energy of a system varies with the number of electrons N in a convex an piecewise linear manner between integer N's. This simply means that we do have a physically rooted reference energy $E(N)$ at non-integer N values, from which we can measure true deformations due only to compression or electronic excitation. Since these are the contributions we associate to sterics, we think that this new measure truly captures SH. Let $\lfloor N \rfloor$ be the integer part of a non-integer electron number N, and $\{N\} = N - \lfloor N \rfloor$ its fractional part. Then the energy of an ensemble with N average electrons, where N is a non-integer between$the \lfloor N \rfloor - 1$ and $\lfloor N \rfloor$ integer electron counts is on a straight line between the energies at those two integers, with a slope equal to the ionization energy at $\lfloor N \rfloor$. Thus, it can be calculated through the following expression:

$$E(N) = E(\lfloor N \rfloor - 1) - \{N\} \times \mathrm{IP}(\lfloor N \rfloor + 1), \tag{3}$$

where IP is the ionization potential of the species at integer $\lfloor N \rfloor + 1$ electron count. This procedure allows to extract a charge transfer (CT) term from the deformation energy. If for a fragment A, with in-the-molecule number of electrons N, we use an external reference with electron count N^0, then

$$\begin{aligned} E^A_{def} = E^A_{self}(N) - E^A_{ref}(N^0) &= \\ \left(E^A_{self}(N) - E^A_{ref}(N)\right) + \left(E^A_{ref}(N) - E^A_{ref}(N^0)\right) &= \\ E^A_{ST} + E^A_{CT}. \end{aligned} \tag{4}$$

In the previous expression we have thus defined the steric (ST) and CT components of E_{def}. The CT component is obtained after Eq. 3. Notice that if $N - N^0 > 1$ we need several consecutive fragment IPs (or electron affinities) to apply the grand canonical formalism.

Computational Details

All calculations were performed in the gas phase at different levels of theory, including HF, DFT and CASSCF methodologies in combination with the aug-cc-pVDZ basis set. Geometry optimizations, frequency calculations, energy evaluations and intrinsic reaction coordinate (IRC) paths were computed using Gaussian09. [80] Wavefunctions were generated with Gaussian09 [80] (for HF and DFT) and PySCF [81] (for CASSCF). Finally, IQA data (see the SI, Section 1, for more details) were computed using the PROMOLDEN code. [82]

In dimeric systems, both frozen (rigid) and relaxed scans were performed. In the former, geometrically fixed monomers were separated in 0.10 or 1.00 Å distance steps until their central

atoms reached a separation of 10 Å. In the relaxed scans, only the distance between these atoms was fixed, and the rest of the degrees of freedom optimized while maintaining the point group symmetry. As DFTs are regarded, B3LYP was chosen in most cases and no dispersion correction was applied, since we are mainly interested in short-range effects. The geometry of the independent monomers was optimized in the gas phase at the same level, and their minimum character tested by standard harmonic analysis.

All reported energies and charges are referenced to the infinite separation limit (≈10 Å). Only average energetic values for equivalent (or close to) atoms are provided.

Calculations regarding the S_N2 reactions were done at the M06-2X//cc-pVDZ level,[83] with no relativistic corrections. This level of theory was chosen after a small benchmarking study of the reproducibility of the activation barriers when comparing with already reported data (see the SI, Section 5.1, for more details). Being these thermoneutral reactions, we have only analyzed their forward profile. In order to compare different systems on the same footing, IRCs are many times reported as ratios (in %, see SI for more details). Energies and charge variations are given relative to reactants.

Results

Mimicking spatial confinement through an external potential

As explained, pure confinement must necessarily lead to a positive E_{def} in atoms. To probe the energetic footprints of geometrical constraints, we have examined the behavior of a He atom when its electrons are subjected to a 3D isotropic parabolic potential centered at the nucleus, $V = (1/2)k\sum_i(r_i^2)$, at the CAS(2,9)//cc-pVDZ level (SI, Section 2). This Hamiltonian is easily implemented in the PySCF suite.[81] In order to compare the effects of geometrical confinement with those of a sterically driven process, IQA calculations were also performed at the CAS(4,18)/cc-pVDZ level for the He_2 dimer as the internuclear distance changes.

Relevant results are found in Fig. 1. As the confinement force constant k increases and the electrons compact themselves, E_{def} grows monotonically. Both the kinetic energy (T) and the electron repulsion (V_{ee}) are responsible for this rise, which is not sufficiently compensated by the increased nuclear attractions (V_{en}). Notice how the different energy components are much larger than the total deformation. This cancellation lies behind the usefulness of E_{def} for chemical applications.

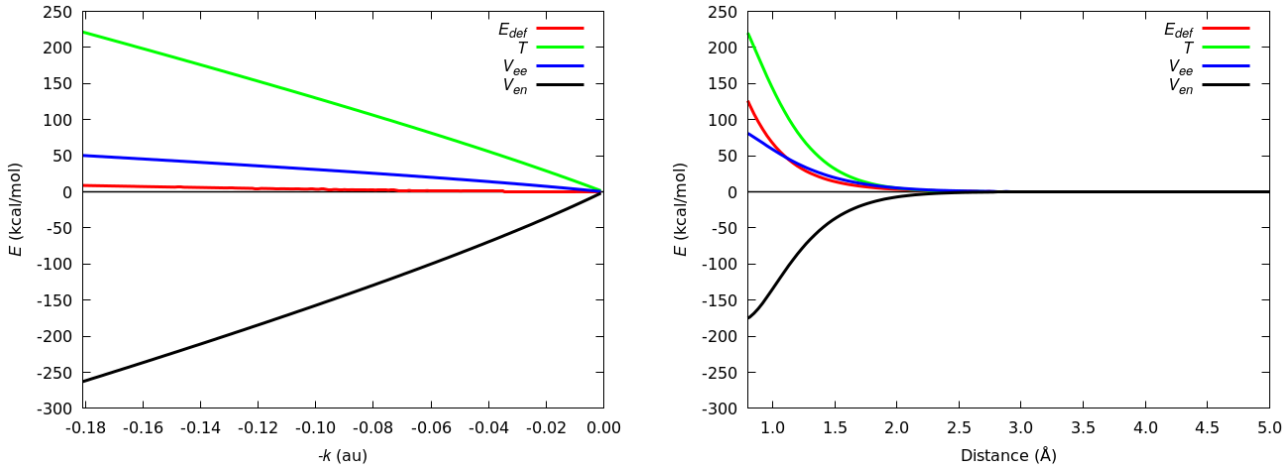

Figure 1: Evolution of the different E_{def} energetic components of a helium atom when it is subjected to a confining parabolic potential and the applied force constant, k, is varied (left), and when it is part of the ground state He_2 dimer and the separation between the He atoms is changed (right). Calculations were performed at the CAS(2,9) and and CAS(4,18) levels, respectively, with the aug-cc-pVDZ basis set. All values relative to the He atom in vacuum.

The behavior of the in-the-molecule He quantum atom in the right panel of Fig. 1 shows how using E_{def} as an SH descriptor in a chemical compression gives rise to the same overall features induced by confinement. It is mostly interesting that V_{en} is now much less able to compensate the rise in T and V_{ee} along compression. This is relatively easy to understand, since the He-in-the-molecule is an open system that acquires a non-negligible probability of having three electrons, which display a large T but considerably less ability to approach the nucleus. In molecules, new phenomena beyond classical Pauli exclusion (which should be well modeled by pure confining potentials) may thus be extremely relevant in the development of SH.

E_{ST} as a faithful estimator of steric hindrance.

As a proof of concept, a well-behaved and simple system was employed to initially assess the reliability of our E_{ST} proposal. In order to do so, the evolution of the self-energies of the methane dimer as two frozen CH_4 monomers approach each other, face to face while preserving C_{3v} symmetry, was evaluated using different methodologies (HF, DFT(B3LYP) and CASSCF (12,8)) in combination with the aug-cc-pVDZ basis set (SI, Section 3). It should be noticed that using a frozen scan is perfectly suitable for validation purposes, which furthermore has been found to provide analogous results to those found for the relaxed approximations within the studied compression regime.

As it can be seen in Fig. 2, moderate values of E_{def}^{C} result again from the cancellation of

larger T, V_{ee}, and V_{en} contributions. Such a behavior (SI, Sec. 3) is rather general, showing that although the rise in T is essential in building SH, it is by no means the only contributor. Our results are in good agreement with previously reported data. [70] Furthermore, the total deformation of both the C atom and the CH_4 molecule decays rapidly with the inter-monomer distance, and is well fitted by a Buckingham potential (see SI Section 3.5).

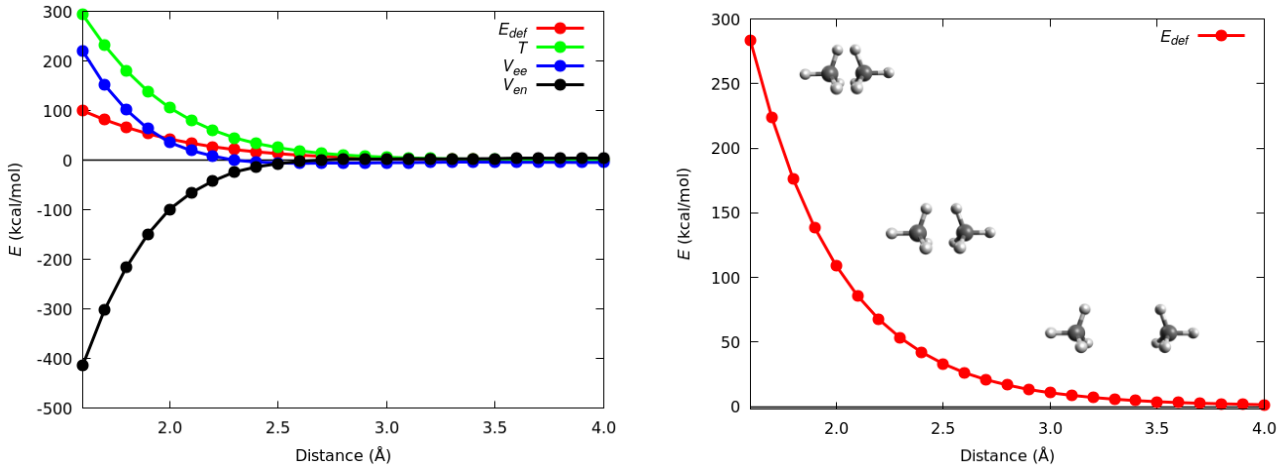

Figure 2: Deformation energy E^{C}_{def} and its constituting components (left), together with the total deformation of the methane monomer (right) computed at the B3LYP/aug-cc-pVDZ level along the frozen compression described in the text. All energies relative to their references, taken at a C-C separation of 10.00 Å.

Since upon compression the electron density redistributes considerably, the (topological) charges of atoms do not remain constant. Fig. 3 shows that as R(C-C) decreases, the C atom loses electrons. Actually (SI, Section 3.4) the clashing inner H atoms also lose electron population, which is accumulated, as expected, at the two terminal H's. This is chemically expected in terms of Pauli exclusion. If we fail to consider the C electron loss by using the plain E^{C}_{def} as an SH descriptor, we will overestimate the C steric contribution. As shown in the figure, E_{CT} decreases E_{ST} between 5 and 10 kcal/mol at the maximum compression. Its contribution gains importance as R decreases and ΔQ grows, as expected. These trends are also observed for the H atoms (SI, Section 3), being the inner ones those exhibiting the largest E_{ST}'s (reaching $\sim$ 20 kcal/mol). The outer H atoms, as expected, get very slightly deformed along the process, with total E_{def} not greater than 2 kcal/mol.

The methodology has an impact on the results, as shown in Fig. 3, although all the levels of theory offer the same general picture for both E_{def} and its constituents. The significantly different ΔQ values offered by the the CASSCF method should not be directly discarded. Notice that the HF values evolve from the CAS to the DFT results as we compress. This may well mean that strong static correlation effects (which can neither be captured by HF or DFT) set in at small distances. In this regard it is particularly satisfying that once CT is singled out, the remaining steric contributions are rather insensitive to the methodology. Moreover, these trends are also found for the remaining atoms (SI, Section 3), and altogether point out that the steric (E_{ST}) contribution under the IQA framework is barely affected by the methodology

employed. Taking this into account, and considering the ability of DFT to provide reasonable results at moderate computational cost, the remaining calculations have been performed at the DFT/aug-cc-pVDZ level of theory.

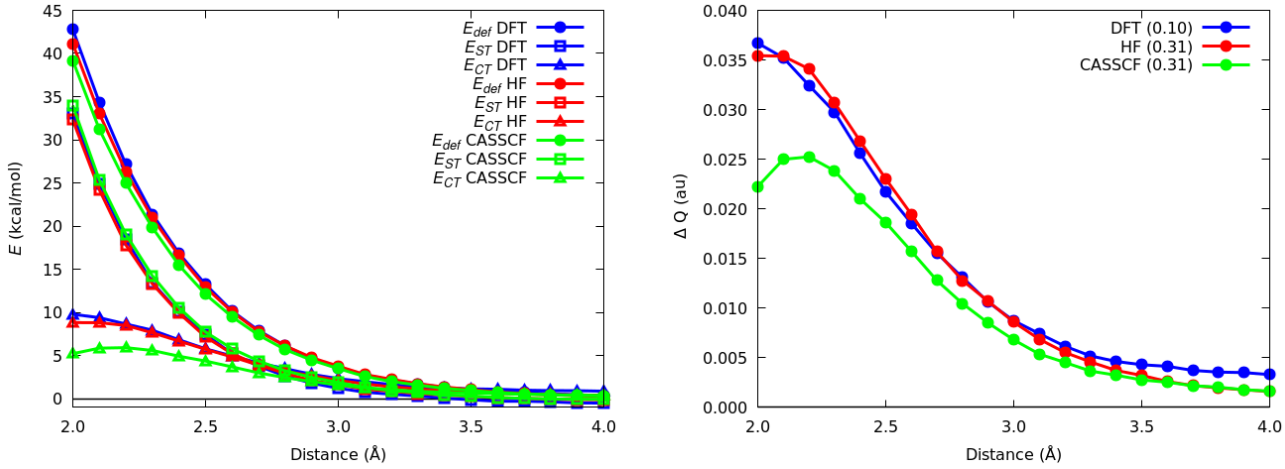

Figure 3: Deformation, E_{def}, and steric, E_{ST}, energies (left) and charge transfer ΔQ (right) for the C atom of the CH_4 molecule along the rigid scan. All the CASSCF, DFT and HF levels are shown. Quantities relative to the quasi-dissociated state at R(C-C) = 10.0 Å. Q^{C} at dissociation is shown in brackets in au.

After this validation, we further analyze how E_{ST} correlates with chemical intuition when H atoms acquire non-negligible atomic charges. This is a case where E_{def} fails to describe properly SH.[70] With that aim, the deformation of the ammonia molecule along the frozen (f) and relaxed (r) compression of the NH_3 dimer was analyzed for a total of four different approximation channels as represented in Fig. 4. The blue lines (at 3.5 Å) appearing in the upcoming figures indicate the average distance at which significant geometrical changes of the NH_3 dimer start to take place along the relaxed approximation. Notice that the self-energy of each NH_3 monomer is built from:

$$E_{self}^{\mathrm{NH_3}} = \sum_{\substack{A\in\{N,H_i\}\\ i=1,2,3}} E_{self}^{A} + \frac{1}{2} \sum_{\substack{\{A,B\}\in\{N,H_i\}\\ i=1,2,3}} E_{int}^{AB} \tag{5}$$

As expected, $E_{def}^{NH_3}$ increases exponentially upon compression, being largest, both for the f and r scans, in H-H approximations. In the most unfavorable eclipsed approach, it scales to 43 and 60 kcal/mol for the r and f scans, respectively. Such results line up with chemical intuition. Also satisfying is that any of the N-N approximation channels yields considerably smaller E_{def}'s $\sim$ 30 kcal/mol, being furthermore nearly identical in the eclipsed and staggered approaches, for both types of scans. We will thus only consider the eclipsed N-N approximation in the following.

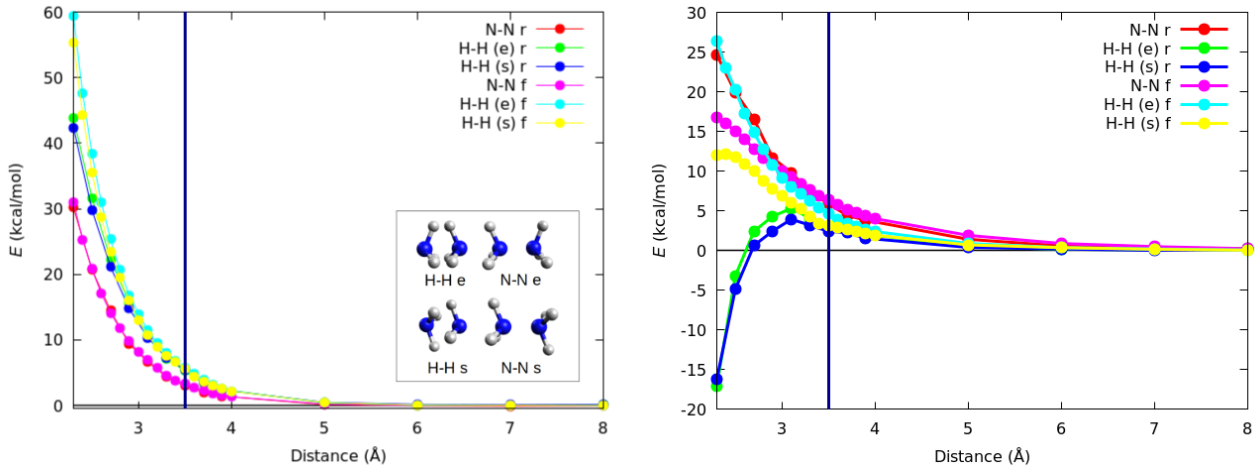

Figure 4: B3LYP/aug-cc-pVDZ total deformation energy of the NH_3 molecule (left) and total ammonia-ammonia interaction energy (right) for the different approximations of the ammonia dimers along the frozen (f) and relaxed (r) scans. The distance is between the N nuclei. Reference values taken at 10.00 Å. Both N-N (e) and N-N (s) channels are indistinguishable and are represented as N-N.

Generally speaking, beyond the 3.5 Å separation limit the f and r approximations provide almost identical total E_{def} results, see Fig. 4, and very similar interaction energies with minor deviations in the H-H (e) case (Fig. 4). This behavior extends to the individual E_{def}^{N} and E_{def}^{H} values, as shown in Figs. 5 and 7. Overall, the results are in consonance with the specially pronounced susceptibility of the NH_3 monomer in the H-H (e) approximation to suffer geometrical deformations even at long range. Below an intermonomer separation of 3.5 Å, geometrical deformations start to play a significant role in the r scan (Sec. 5 of the SI contains more details). In the N-N approximations, the ammonia monomers pyramidalize slightly (the H-N-H umbrella and the intra-molecular H-H distance decrease by 3 degrees and 0.02 Å, respectively, at the shortest separation), while the corresponding N-H distance barely changes. This result can be interpreted sterically: as a response to congestion, the NH_3 lone pair get less expressed, increasing its s character. This is accompanied by a substantial charge transfer from the N to the H atoms that reaches $\Delta Q \approx$ -0.03 au for each H atom.

As expected, the geometrical distortions in the H-H approximations are even larger, opposed to what has just been described, and also in line with steric arguments. The H-N-H bond angle opens by 9.0 and 8.0 degrees in the eclipsed and staggered conformations, respectively. This causes a significant increase in the H-H intra-molecular bond distance of $\sim$ 0.06 Å and $\sim$ 0.05 Å, and a substantial decrease in the intra-molecular N-H bond distance of about 0.02 Å in both cases. Additionally, about 0.02 e are transferred from each of the H basins to the N atoms. As we see, CT is an essential player in the decrease of SH.

Regarding the individual atomic contributions in the long-range regime, all E_{def}, E_{ST}, and ΔQ for the N and H atoms are basically indistinguishable in the f and r paths. Figs. 5 and 7 also show that in this region these descriptors do not tell between the eclipsed and staggered approaches, suggesting that at long distances the N-N separation dominates.

At shorter ranges, the r and f channels start to diverge, this being particularly clear in the H-H approximations, as expected. Fig. 5 shows that the $\mathrm{E}^{\mathrm{N}}_{def}$ along the N-N approach is larger in the f than in the r scan, exhibiting an energy difference as large as 5 kcal/mol. Meanwhile, $\mathrm{E}^{\mathrm{N}}_{ST}$ remains barely distinguishable in both scans, reaching a value of about 35 kcal/mol at the largest compression. This is a satisfying feature of our proposal. The E_{def}-E_{ST} difference is easily rationalized with the help of Fig 6, which shows that the depletion in Q(N) is slightly larger in the r scan, this leading to a larger CT term and lower E_{def}.

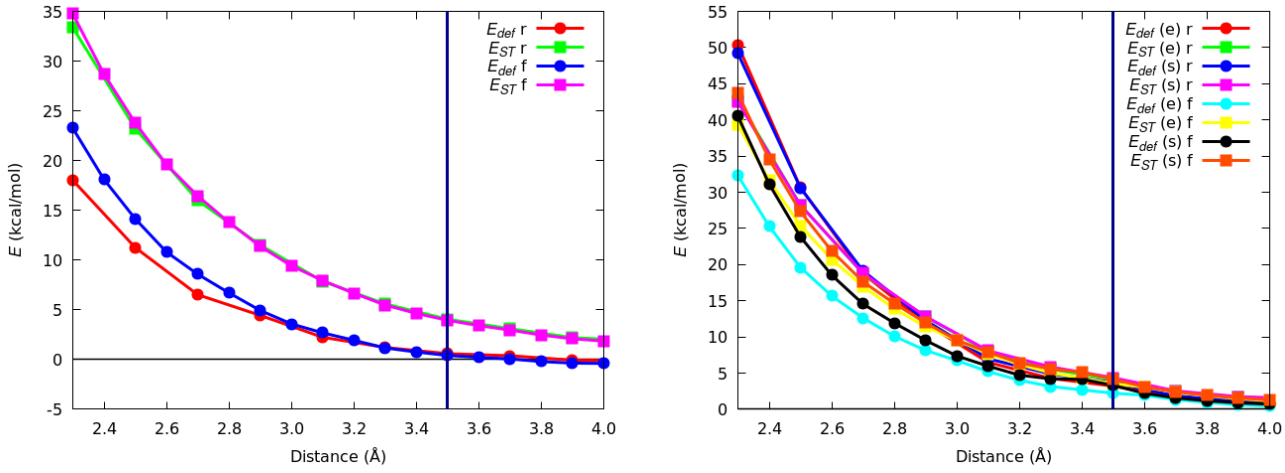

Figure 5: Behavior of E^{N}_{def} and E^{N}_{ST} for the N-N (left) and H-H (right) approaches, at the B3LYP/aug-cc-pVDZ. References taken at 10.00 Å. N-N separation.

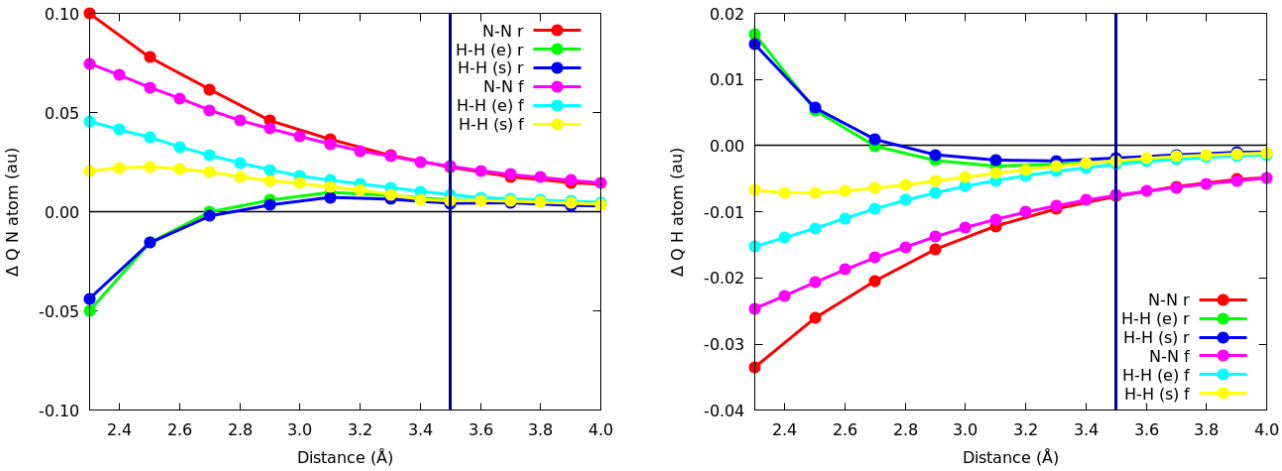

Figure 6: Change in the atomic charges of the N (left) and H (right) atoms of the NH_3 molecule computed at the B3LYP/aug-cc-pVDZ level. References taken at the 10.00 Å N-N distance limit, at which Q(N) and Q(H) are -1.15 and 0.38 au, respectively.

These trends are reversed for H-H approaches (see Fig. 5). Geometrical relaxation, leading to a larger N-N exposure due to umbrella planarization, increases E^{N}_{def} considerably, rising up to 20 kcal/mol with respect to the one in f scans. In the latter, both the deformation energy and its steric component are larger in the staggered case, a difference that vanishes after relaxation.

Fig. 7 examines the H atoms. E^{H}_{def} is clearly negative both in the f and r N-N scans, along which electrons are pumped from the N lone pairs into the H atoms. Correcting for CT, E^{H}_{ST} becomes positive, slightly larger in the r scan. This behavior admits a classical steric reading: E^{H}_{def} is a result of increased H-H congestion caused by larger H electron population. It becomes exacerbated in the r scan as the umbrella angle closes and the H-H distance decreases. Avoidance of the dominant lone pair SH thus leads to an increase in the H-H congestion.

The behavior of the H steric-like descriptors in the H-H approach is different, as shown in Fig. 7. E^{H}_{def} is clearly negative except at the closest distances for both f and r scans. Correcting for CT, E^{H}_{ST} recovers its expected chemical meaning in the frozen approaches, including larger values (about 2 kca/mol) in eclipsed configurations. Unexpectedly, the f approach also pumps out electrons from the N atom into the sterically clashing H's. To understand this, we must recognize that it is still the N atoms which dominate the steric energies in H-H approaches, so that it might be favorable to decrease E^{N}_{ST} by depopulating the N atom even at the expense of increasing the H population. Relaxation adds another source of complexity. Now at the shortest distances the Hs get depopulated. With this, their E_{ST} overshoots, ending up with a slightly smaller value than in the isolated NH_3 molecule. Recall, anyway, that the total $E^{\mathrm{NH_3}}_{ST}$,

that also includes the N atoms and the N-H interactions, is overall positive and decreases upon relaxation.

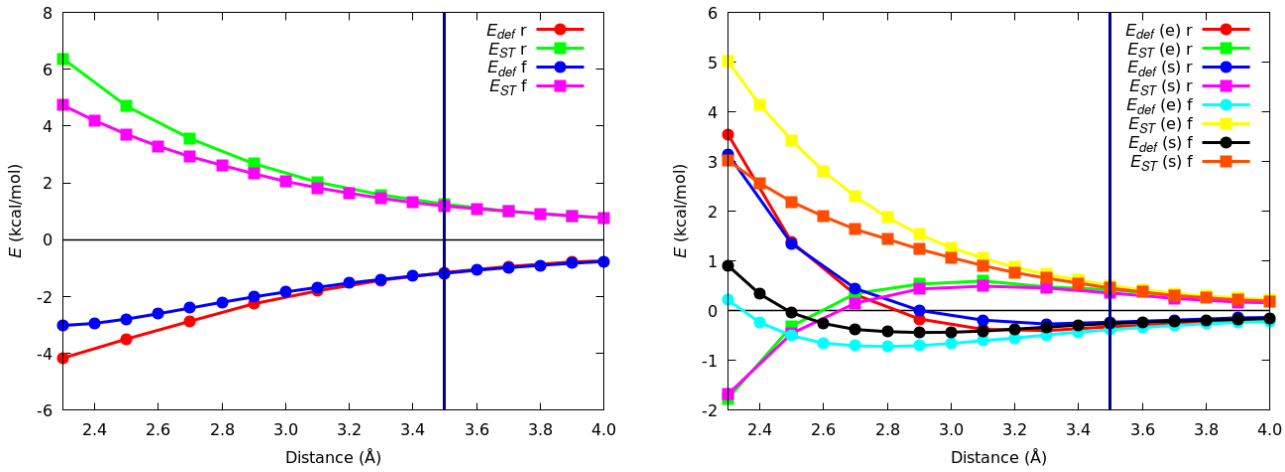

Figure 7: Behavior of E^{H}_{def} and E^{H}_{ST} for the N-N (left) and H-H (right) approaches, at the B3LYP/aug-cc-pVDZ. References taken at 10.00 Å. N-N separation.

It is to be stressed that it is the conspiracy between the energy penalty associated to the intermolecular H-H congestion and the relaxation effect of the intramolecular H-H lengthening that leads to the observed behavior, which is not easily predicted. The fact that E^{H}_{ST} reaches negative values with respect to the chosen reference is in perfect agreement with chemical intuition and does not represent any conceptual pitfall, being rather the result of the slight decrease in the steric energy suffered by the terminal H atoms in the quasi-planar NH_3 moiety relative to the standard NH_3 trigonal pyramid. All these considerations evidence that E_{ST} is a more adequate estimator of SH than E_{def} alone, particularly in the case of H atoms.

The role of E_{ST} in common self-substitution reactions.

In order to further test the applicability and conceptual implications of E_{ST} under a more chemically relevant scenario, the archetypal bimolecular nucleophilic self-substitution S_N2 reactions of a set of simple halomethanes CH_3X, X = F, Cl, Br have been employed as model systems. Fig. 8 collects reaction energy and reaction force[65] diagrams (SI, Section 5.4) for them.

As it can be seen from Fig. 8, and in accordance with classical organic chemistry rules and already reported data by Alkorta *et al*, [84] the computed activation energy of the reactions decreases along the halogen series (14.12, 12.52 and 9.86 kcal/mol for F, Cl and Br, respectively, at the M06-2X/aug-cc-pVDZ level). Such a trend has been classically explained attending to

the change in the leaving group (L) ability and the strength of the C–X bonds for the different halogens (X). A similar behavior is also observed for the nominal charge of the halogen atoms in the activation complex structure (-0.76, -0.70 and -0.67 au for F, Cl and Br respectively, see SI Section 5 for more details) and can be attributed to the change in the electronegativity of the atoms along the series.

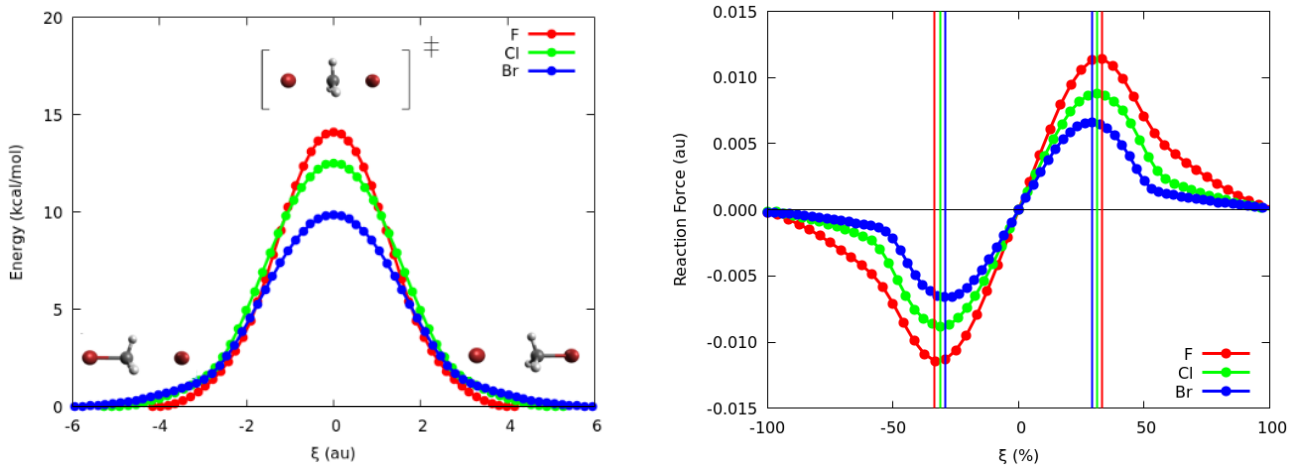

Figure 8: Reaction energy (left) and reaction force (right) diagrams for the self-substitution reaction of CH_3X and X^- evaluated at the M06-2X/aug-cc-pVDZ level of theory in the gas phase. The vertical lines indicate the position of the reaction force minima and maxima (i.e the α and γ points) along the reaction profiles.

It is interesting to analyze the progress of the reaction force (RF) along the reaction. Originally formulated by Toro-Labbé and coworkers, [65] the RF is defined as the negative derivative of the potential energy of the system with respect to the intrinsic reaction coordinate (ξ), and it is able to uncover the different steps involved in a chemical reaction. [85–87] As evidenced in the figure, the reactions proceed in one step.[88] It is customary to highlight the minimum (α) and maximum (ω) points in the RF signaling the geometries at with the retarding forces building the forward and backward barriers peak, respectively. These, together with the transition state (TS, $\xi = 0$) separate the reaction in four regions.

In the first one, going from the reactive complex to α, and also called preparation step, the nucleophile (Nu) approaches the electrophilic center. This is accompanied by a slight deformation of the local geometry of the latter with a minor C–X bond elongation. The second zone, leading to the TS, usually consists of electronic rearrangements like bond breaking or bond formation. The remaining two zones, TS to γ, and γ to the product complex, are symmetric in thermoneutral reactions.

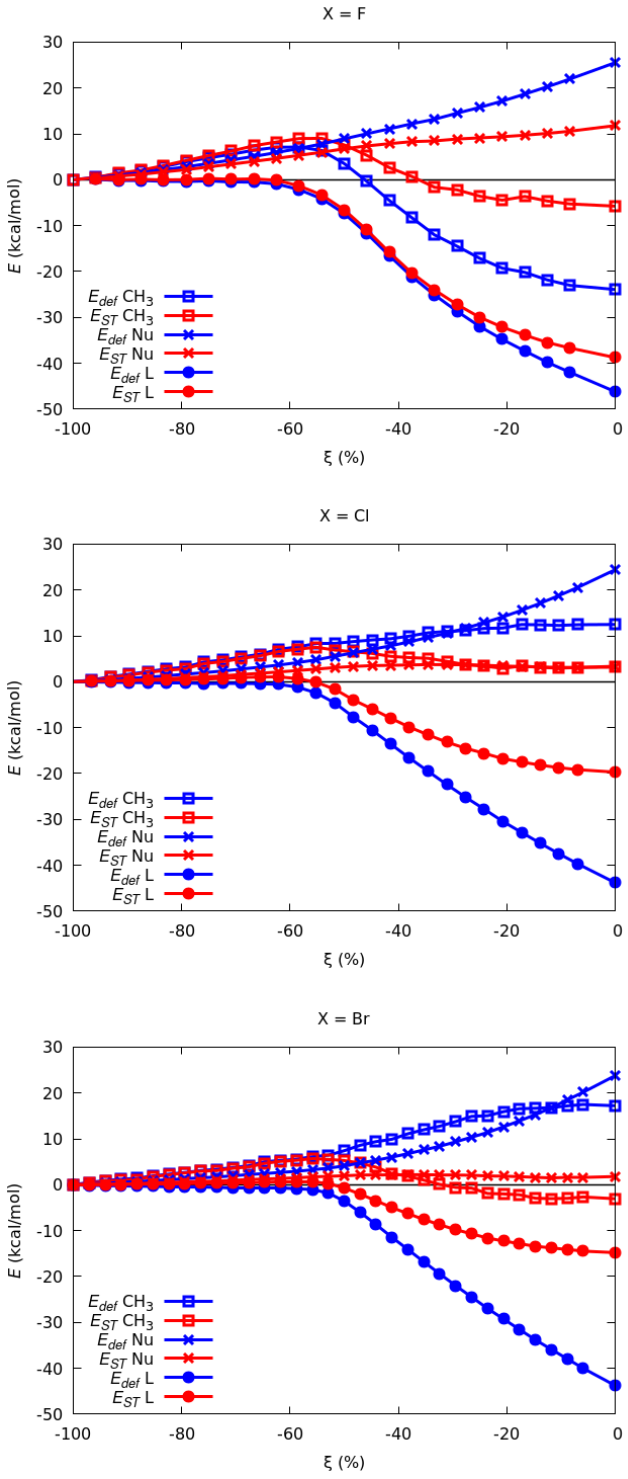

Figure 9: Total deformation and steric energies for the different groups involved along the self-substitution reactions under study when X=F (top), Cl (center), and Br (bottom). All energies referred to the reactive complex.

The evolution of E_{def} and its components for the electrophile (CH_3, El), nucleophile (Nu), and leaving group (L) is plotted in Fig. 9. During the initial stages of the reaction, both E_{def} and E_{ST} of the El and Nu groups increase almost linearly with ξ, while the L group remains basically undeformed. Thus, in the preparation step, SH accumulates in the groups that approach each other. As a result of almost vanishing CT (see Fig. 10), $E_{ST} \approx E_{def}$. Interestingly, the El group reaches its maximum steric penalty in the vicinity of the α point, pointing towards its importance in the building of the barrier.

From this point on, a considerable amount of steric energy is released in L, a result aligned both with a fast change of the El group geometry (that passes from a C_{3v} to a planar D_{3h} structure), and with the elongation of the C–L distance. Chemically speaking, the congested X in CH_3X starts its transition to a free, uncongested X^- anion. $\Delta E^{\mathrm{L}}_{def} \approx -45$ kcal/mol is barely dependent on the nature of the halogen, but the magnitude of $\Delta E^{\mathrm{L}}_{ST}$ decreases along the F to Cl to Br series (-40, -20 and -15 kcal/mol,respectively). In so doing, E_{CT} (SI, Section 5) follows an obviously opposite behavior. At a first glance, the smaller E_{ST} value for the bulkier halogen seems counter-intuitive. Noticing that the ΔQ(L) are -0.1, -0.3, and -0.4 e for F, Cl and Br, see Fig. 10, explains the results. For simple monoatomic groups, softer species are easier to deform and to charge.

A completely equivalent analysis regards the nucleophile, which experiences a moderate increase in its E_{def} along the reaction. Again, the softer the species, the easier to charge, as evidenced by the trends in the charge at the TS of $\Delta Q \sim 0.18$, 0.25, and 0.27 au for F, Cl, and Br, respectively. Since, again, ΔE_{ST} is rather insensitive to the halogen, peaking at about 25 kcal/mol, a consistent reduction in $\Delta E_{ST} \sim 12$, 3 and 2 kcal/mol for F, Cl and Br is found along the series. The approach of the bromide anion to methyl bromide has an almost pure charge transfer cost for the Br^-.

On the contrary, E^{El}_{def} is rather dependent on X. If X=Cl or Br, it increases as the reaction proceeds, being CT controlled. However, for X=F, E^{El}_{def} decreases after the preparation step after showing a maximum. Indeed, as shown in Fig. 10, the trend in ΔQ(El) is very sensitive to X, evolving from negative values in the case of F ($\Delta Q \sim$ - 0.08 a.u) to positive ones for Cl or Br ($\Delta Q \sim +0.04$, +0.09 for Cl and Br). This evidences the unique, hard to charge character of the F atom. If CT is discounted, E^{El}_{ST} evolves similarly in all the halogens.

Altogether, these results point out that E_{ST} is more susceptible than E_{def} to changes in the chemical nature of the species studied, making it a better SH estimator that avoids the masking

effects of charge transfer.

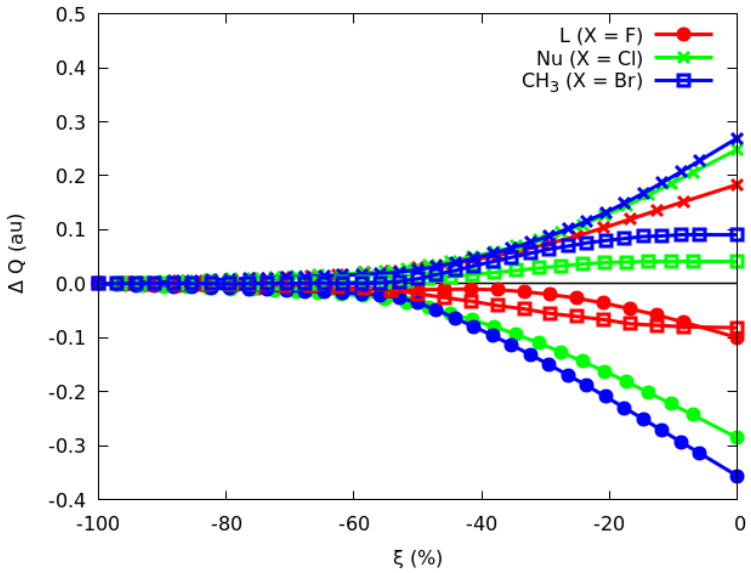

Figure 10: Evolution of ΔQ in the reactions under study starting from the reactive complex. At this point, $Q(\text{Nu}) = -0.96, -0.95, -0.94$, $Q(\text{L}) = -0.68, -0.41, -0.31$ and $Q(\text{El}) = 0.63, 0.36, 0.25$ au for X = F (red), Cl (green), and Br (blue), respectively.

Taking into account the important role of geometrical relaxations in building steric contributions, a scan involving the approximation of a fluoride anion to a geometrically frozen CH_3F molecule was performed (see the SI, Section 5.6 for further details). As it can be seen in Fig. 11, the frozen (f) approximation reproduces quite well the E_{ST} curves of the relaxed (r) reaction in the initial, pertubative-like stages. This regime can thus be attributed, in accordance with our previous hypotheses, to a partial compression of Nu and El yielding a significant steric penalty that does not affect the L group.

After this, the f and r approximations diverge dramatically as a result of the bond breaking and formation processes that induce considerable geometrical distortions. In the f process, E_{ST}^{L} increases slightly ($\sim$ 5 kcal/mol) as a result of the compression of the attacking F atom and the lack of relaxation associated to the C-F rupture, a result differing strongly from the already commented trends in the relaxed approximation. Analogously, the f scan leads to much larger $E_{ST}^{\text{Nu,El}}$ kcal/mol values due to the approach to a rigid halomethane.

Further insight into the f and r behaviors can be obtained from examining the energy change accompanying the pyramidalization of an otherwise planar CH_3^+ species in the gas phase. For such a purpose, a set of intermediate geometries were generated from a linear interpolation between the structures of the CH_3 moiety in the CH_3F system at the end of the preparation

stage and that in the TS complex.

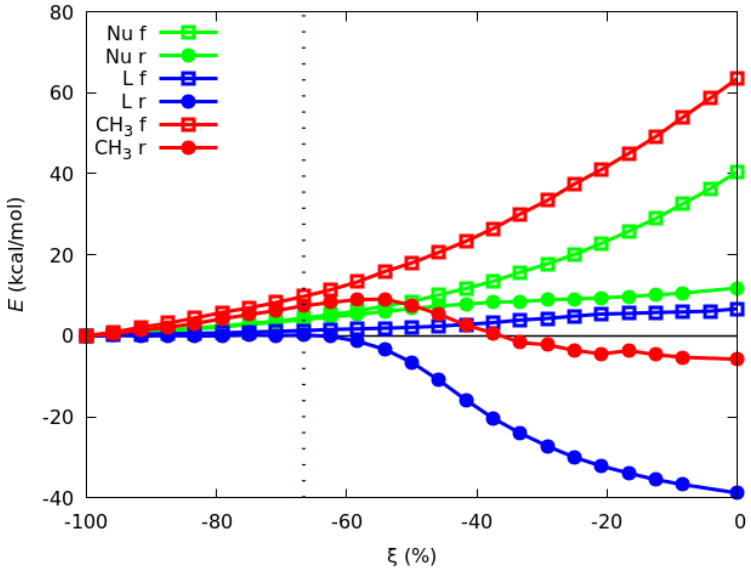

Figure 11: Evolution of E_{ST} along the frozen (f) and relaxed (r) reactions of CH_3F and F^-. The dashed line indicates the point at which the geometry of the CH_3X moiety starts to get distorted.

As it can be seen in Fig. 12, before the halomethane gets significantly distorted, the overall E_{def}^{El} along the reaction (green curve) is mainly determined by the nucleophile-electrophile compression (blue curve). However, once the CH_3 skeleton of the halomethane starts distorting (as indicated by a dashed line in Fig. 12), the steric penalty associated to the compression against the nucleophile is partially counteracted by the favorable planarization of the methyl group (red curve). Such a result suggests that the CH_3 planarization is energetically favorable in terms of E_{def}, an insight in agreement with already reported data.[26]

The global relaxed behavior observed for E_{def}^{El} thus arises from the conspiring interplay between the energy penalty associated to the compression induced by the attacking halide and the relaxation due to the planarization of the methyl scaffold. Rigorously, the reconstruction of E_{def}^{El} cannot be done exclusively from the compression (blue curve) and the planarization (red curve) contributions, since the "decompression" of leaving group should also be taken into account.

Finally, and for the sake of completeness, we have decided to compare also our basic gas phase $F^- + CH_3F$ results with the picture provided by the ASM model. To do that, E_{def} was decomposed as a sum of a geometrical deformation energy $E_{def,g}$, computed as the cost of taking each isolated fragment to the geometry displayed at every ξ, and an electronic deformation term, $E_{def,e}$ that takes everything else into account (see the SI, Section 5.5, for more details). Notice

that in the ASM model, only geometrical deformations are taken into account. The results are collected in Fig. 13.

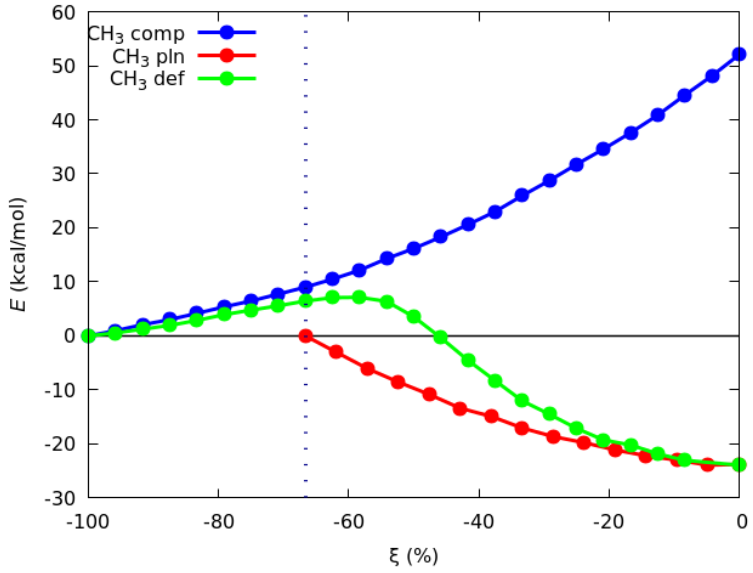

Figure 12: Evolution of the computed E_{def} of the CH_3 moiety (CH_3 def) in the relaxed $F^- + CH_3F$ substitution reaction along with the contributions of the nucleophile compression (CH_3 comp) and planarization (CH_3 pln) processes. The dashed line indicates the point where the geometry of the CH_3X moiety starts to get distorted.

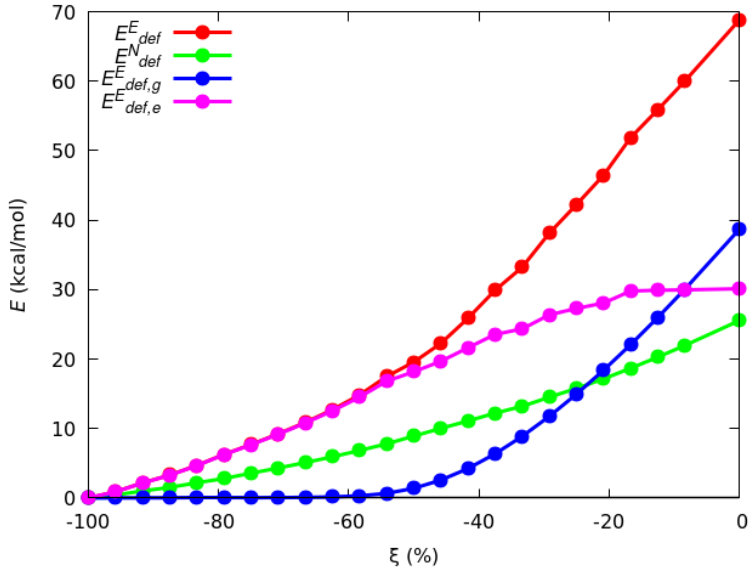

Figure 13: Evolution of E_{def} along with its geometrical ($E_{def,g}$) and electronic ($E_{def,e}$) components for the $F^- + CH_3F$ reaction. Calculations were performed at the M062X/aug-cc-pVDZ level in the gas phase.

During the preparation stage, E_{def} is dominated by its electronic term $E_{def,e}$, since geometric distortions are negligible. Only after the El center starts to planarize does a steep rise in $E_{def,g}$

develops. Although IQA feels a noticeable energetic distortion, ASM skips it.

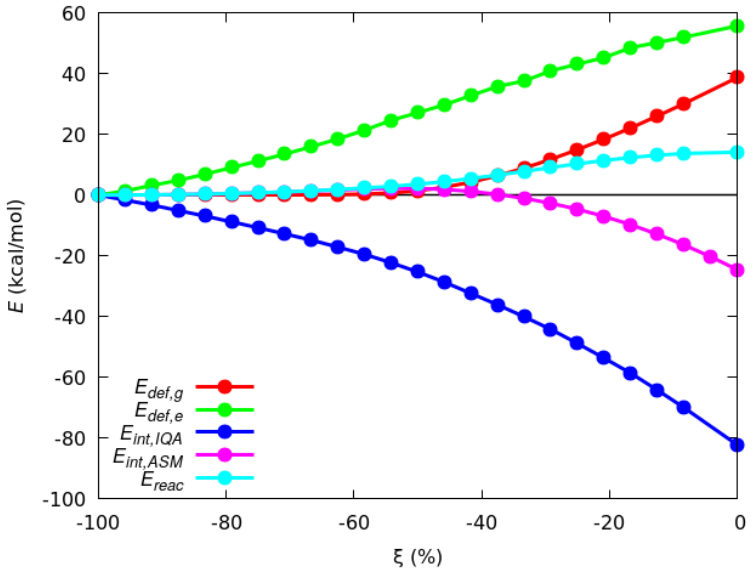

Figure 14: Evolution of the total geometrical, $E_{def,g}$ and electronic $E_{def,e}$, deformation energies along with the electrophile-nucleophile interaction term $E_{int,IQA}$, together with $E_{int,ASM}$ and the total reaction energy E_{reac} along the forward part of the $F^- + CH_3F$ reaction. Calculations performed at the M062X/aug-cc-pVDZ level in the gas phase.

The considerable difference between the IQA and ASM pictures is even clearer after Fig. 14. Initially, the total E_{def}, being almost entirely dominated by its electronic contribution, is partially counteracted by the interaction energy $E_{int,IQA}$ between the two fragments. This results in small total reaction energies (< 5 kcal/mol), proper of a perturbation-like regime. The small reaction energies observed during the initial stages of the reaction arise in IQA form the interplay of a non-negligible electronic deformation and a balancing interaction. Since the ASM model considers the strain energy as a purely geometrically-driven entity, it skips electronic deformations altogether. This provides, in our opinion, a somewhat distorted image of reality.

As the reaction proceeds, the geometrical E_{str} of the ASM model increases as a result of the major geometrical distortion suffered by the reacting species, being only partially balanced by $E_{int,ASM}$. The building of the barrier is thus explained in an equivalent qualitative (not quantitative) way by both the ASM and the IQA formalisms. It should be however noticed that $E_{int,IQA}$ is stabilizing along the whole reaction profile, whereas its $E_{int,ASM}$ analog exhibits a slight destabilizing character during the initial stages of the reaction.

Conclusions

In this paper, the actual relation between steric hindrance and common IQA energetic terms, in particular the deformation energy of an atom or fragment E_{def}, has been exhaustively examined and addressed. Furthermore, an estimator of SH, as represented by E_{ST}, has been developed.

As far as the more common E_{def} is concerned, we have evidenced that such an energy term is not able to provide a description of steric hindrance that mimics chemical intuition, in agreement with the trends recently suggested in the literature. [70] Such a result can be considered to arise from the non-negligible effect that a change in the number of electrons (N) of an species has in its self energy E_{self}. Accounting for such terms in E_{self} allows for its fragmentation in a charge transfer, E_{CT}, and a (more) purely steric, E_{ST}, terms. It is precisely such a decomposition what enables the obtention of a more adequate and faithful estimator of steric effects.

The performance of our approximation has been put to the test with a variety of different chemical scenarios, studying for such a purpose the rigid and relaxed compressions of dimeric systems. We have shown that the steric descriptor, E_{ST}, is able to provide reasonable results in all cases, being furthermore nearly independent on the methodology employed and yielding chemically appealing and coherent trends in consonance with chemical intuition. It is worth to mention that these trends also hold for the more problematic case of H atoms bearing non-negligible charges, where E_{def} behaves against intuition. [70]

Additionally and for the sake of clarity, the application of the model has been extended to a more realistic chemical scenario, and an application to bimolecular nucelophillic self-substitution reactions between CH_3X and X^- for X = F, Cl and Br has also been presented. The results suggest that examining the evolution of E_{ST} and E_{CT} along chemical reactions provides a steric-like scenario which may find useful applications.

Overall, we hope to have proven the importance of removing the masking effects of charge transfer to get an energetic descriptor of steric effects that satisfies chemical expectations. We think that the estimator here presented may be very helpful to uncover the true driving forces that lie behind several chemical phenomena.

Acknowledgments

We thank the Spanish MICINN, grant PGC2018-095953-B-I00, the Spanish MICIU for the predoctoral FPU grant, FPU19/02903, the Principado de Asturias government, grant FC-GRUPIN-IDI/2018/000117, and the European Union FEDER funds for financial support.

References

[1] G. Frenking, A. Krapp, *J. Comput. Chem.* **2007**, *28*, 15–24.

[2] *IUPAC. Compendium of Chemical Terminology, 2nd ed. (The "Gold Book"). Compiled by A. D. McNaught and A. Wilkinson. Blackwell Scientific Publications, Oxford (1997). Online version (2019-) created by S. J. Chalk. ISBN 0-9678550-9-8. https://doi.org/10.1351/goldbook.*

[3] K. B. Wiberg, *Angew. Chem. Int. Ed.* **1986**, *25*, 312–322.

[4] X. Chen, C. K. Regan, S. L. Craig, E. H. Krenske, K. N. Houk, W. L. Jorgensen, J. I. Brauman, *J. Am. Chem. Soc.* **2009**, *131*, 16162–16170, PMID: 19842649.

[5] H. Jacobsen, T. Ziegler, *Comments on Inorganic Chemistry* **1995**, *17*, 301–317.

[6] L. Song, M. Liu, W. Wu, Q. Zhang, Y. Mo, *J. Chem. Theory Comput.* **2005**, *1*, 394–402, PMID: 26641506.

[7] A. von Baeyer, *Ber. Dtsch. Chem. Ges.* **1885**, *18*, 2637.

[8] M. Smith, J. March, *March's Advanced Organic Chemistry: Reactions, Mechanisms, and Structure*, Wiley, Garden City, New York, **2007**.

[9] J. A. Hirsch, *Table of Conformational Energies 1967*, John Wiley & Sons, Ltd, **2007**, pp. 199–222.

[10] C. A. Tolman, *J. Am. Chem. Soc.* **1970**, *92*, 2956–2965.

[11] L. Lunazzi, M. Mancinelli, A. Mazzanti, S. Lepri, R. Ruzziconi, M. Schlosser, *Org. Biomol. Chem.* **2012**, *10*, 1847–1855.

[12] Y. X. Li, H. Zhang, M. N. Yu, S. S. Wang, Y. R. Liu, D. Q. Lin, L. H. Xie, Z. Q. Lin, W. Huang, *Nanoscale* **2019**, *11*, 5158–5162.

[13] J. M. McGrath, M. D. Pluth, *J. Org. Chem.* **2014**, *79*, 711–719, PMID: 24377967.

[14] V. Krishnan, S. Vazquez, K. Maitra, S. Maitra, *Chem. Phys. Lett.* **2017**, *689*, 148 – 151.

[15] J. E. Díaz, A. Mazzanti, L. R. Orelli, M. Mancinelli, *ACS omega* **2019**, *4*, 4712–4720, 31459658[pmid].

[16] M. Parafiniuk, M. P. Mitoraj, *J. Mol. Model.* **2014**, *20*.

[17] S. Liu, N. Govind, *J. Phys. Chem. A* **2008**, *112*, 6690–6699, PMID: 18563887.

[18] V. Dragojlovic, *ChemTexts* **2015**, *1*, 14.

[19] Z. Ye, J. Wang, S. S. K. Kothapalli, Z. Yang, L. Chen, W. Xu, Y. Cai, T. Zhang, X. Xiao, P. Deng, W. Feng, L. Yuan, *Chem. Commun.* **2020**, *56*, 1066–1069.

[20] A. A. Trifonov, T. V. Mahrova, L. Luconi, G. Giambastiani, D. M. Lyubov, A. V. Cherkasov, L. Sorace, E. Louyriac, L. Maron, K. A. Lyssenko, *Dalton Trans.* **2018**, *47*, 1566–1576.

[21] S. Nückel, P. Burger, *Organometallics* **2000**, *19*, 3305–3311.

[22] S. Liu, H. Hu, L. G. Pedersen, *J. Phys. Chem. A* **2010**, *114*, 5913–5918.

[23] H. C. Brown, I. Moritani, Y. Okamoto, *J. Am. Chem. Soc.* **1956**, *78*, 2193–2197.

[24] M. Charton, *J. Org. Chem.* **1977**, *42*, 2528–2529.

[25] J. Légarié Lavergne, A. Jayaraman, L. C. Misal Castro, E. Rochette, F. G. Fontaine, *J. Am. Chem. Soc.* **2017**, *139*, 14714–14723, PMID: 28901757.

[26] F. M. Bickelhaupt, T. Ziegler, P. v. R. Schleyer, *Organometallics* **1996**, *15*, 1477–1487.

[27] D. N. Reddy, E. N. Prabhakaran, *Biopolymers* **2014**, *101*, 66–77.

[28] R. J. Hooley, S. R. Shenoy, J. Rebek, *Org. Lett.* **2008**, *10*, 5397–5400, PMID: 18989966.

[29] R. W. Taft, *J. Am. Chem. Soc.* **1952**, *74*, 2729–2732.

[30] R. W. Taft, *J. Am. Chem. Soc.* **1953**, *75*, 4538–4539.

[31] L. P. Hammett, *J. Am. Chem. Soc.* **1937**, *59*, 96–103.

[32] I. Fernández, G. Frenking, E. Uggerud, *Chem. Eur. J.* **2009**, *15*, 2166–2175.

[33] W. J. van Zeist, F. Bickelhaupt, *Chem. Eur. J.* **2010**, *16*, 5538–5541.

[34] V. Pophristic, L. Goodman, *Nature* **2001**, *411*, 565–568.

[35] R. F. W. Bader, *Chem. Eur. J.* **2006**, *12*, 2896–2901.

[36] J. K. Badenhoop, F. Weinhold, *Int. J. Quantum Chem.* **1999**, *72*, 269–280.

[37] F. M. Bickelhaupt, E. J. Baerends, *Angew. Chem. Int. Ed.* **2003**, *42*, 4183–4188.

[38] F. Weinhold, *Nature* **2001**, *411*, 539–541.

[39] S. Jeulin, S. D. de Paule, V. Ratovelomanana-Vidal, J.-P. Genêt, N. Champion, P. Dellis, *PNAS* **2004**, *101*, 5799–5804.

[40] L. Qiu, J. Wu, S. Chan, T. T.-L. Au-Yeung, J.-X. Ji, R. Guo, C.-C. Pai, Z. Zhou, X. Li, Q.-H. Fan, A. S. C. Chan, *PNAS* **2004**, *101*, 5815–5820.

[41] A. Martín Pendás, M. A. Blanco, E. Francisco, *Journal of Computational Chemistry* **2009**, *30*, 98–109.

[42] S. Liu, L. Liu, D. Yu, C. Rong, T. Lu, *Phys. Chem. Chem. Phys.* **2018**, *20*, 1408–1420.

[43] S. Liu, *J. Chem. Phys.* **2007**, *126*, 244103.

[44] A. Nagy, *Chem. Phys. Lett.* **2007**, *449*, 212–215.

[45] B. Jeziorski, R. Moszynski, K. Szalewicz, *Chem. Rev.* **1994**, *94*, 1887–1930.

[46] F. Weinhold, C. R. Landis, *Valency and Bonding: A Natural Bond Orbital Donor-Acceptor Perspective*, Cambridge University Press, **2005**.

[47] M. v. Hopffgarten, G. Frenking, *WIREs Comput. Mol. Sci.* **2012**, *2*, 43–62.

[48] M. Blanco, A. Martín Pendás, E. Francisco, *J. Chem. Theory Comput.* **2005**, *1*, 1096–1109.

[49] W. H. E. Schwarz, H. Schmidbaur, *Chem. Eur. J.* **2012**, *18*, 4470–4479.

[50] J. K. Badenhoop, F. Weinhold, *J. Chem. Phys.* **1997**, *107*, 5406–5421.

[51] L. Goodman, H. Gu, V. Pophristic, *J. Phys. Chem. A* **2005**, *109*, 1223–1229, PMID: 16833433.

[52] J. W. Hollett, A. Kelly, R. A. Poirier, *J. Phys. Chem. A* **2006**, *110*, 13884–13888, PMID: 17181348.

[53] S. Liu, L. Liu, D. Yu, C. Rong, T. Lu, *Phys. Chem. Chem. Phys.* **2018**, *20*, 1408–1420.

[54] S. Liu, C. Rong, T. Lu, *Phys. Chem. Chem. Phys.* **2017**, *19*, 1496–1503.

[55] M. Alipour, A. Mohajeri, *Mol. Phys.* **2012**, *110*, 2895–2899.

[56] I. Fernández, F. M. Bickelhaupt, *Chem. Soc. Rev.* **2014**, *43*, 4953–4967.

[57] W. J. van Zeist, F. M. Bickelhaupt, *Org. Biomol. Chem.* **2010**, *8*, 3118–3127.

[58] F. M. Bickelhaupt, K. N. Houk, *Angew. Chem. Int. Ed.* **2017**, *56*, 10070–10086.

[59] D. H. Ess, K. N. Houk, *J. Am. Chem. Soc.* **2007**, *129*, 10646–10647.

[60] F. M. Bickelhaupt, K. N. Houk, *Angew. Chem. Int. Ed.* **2017**, *56*, 10070–10086.

[61] J. Kubelka, F. M. Bickelhaupt, *J. Phys. Chem. A* **2017**, *121*, 885–891, PMID: 28045531.

[62] L. P. Wolters, F. M. Bickelhaupt, *WIREs Comput. Mol. Sci.* **2015**, *5*, 324–343.

[63] F. Weinhold, *Angew. Chem. Int. Ed.* **2003**, *42*, 4188–4194.

[64] J. C. R. Thacker, P. L. A. Popelier, *Theor. Chem. Acc.* **2017**, *136*.

[65] P. Politzer, A. Toro-Labbé, S. Gutiérrez-Oliva, B. Herrera, P. Jaque, M. C. Concha, J. S. Murray, *J. Chem. Sci* **2005**, *117*, 467–472.

[66] R. F. W. Bader, Y. Tal, S. G. Anderson, T. T. Nguyen-Dang, *Isr. J. Chem.* **1980**, *19*, 8–29.

[67] P. Popelier, P. Maxwell, I. Thacker, J.C.R. Alkorta, *Theor. Chem. Acc.* **2019**, *138*, 12.

[68] J. Hernández-Trujillo, C. F. Matta, *Struct. Chem.* **2007**, *18*, 849–857.

[69] J. Poater, M. Solà, F. M. Bickelhaupt, *Chem. Eur. J.* **2006**, *12*, 2889–2895.

[70] B. C. B. Symons, D. J. Williamson, C. M. Brooks, A. L. Wilson, P. L. A. Popelier, *ChemistryOpen* **2019**, *8*, 560–570.

[71] P. I. Maxwell, P. L. A. Popelier, *J. Comput. Chem.* **2017**, *38*, 2459–2474.

[72] A. Martín Pendás, M. A. Blanco, E. Francisco, *J. Comput. Chemr.* **2007**, *28*, 161–184.

[73] R. A. Buckingham, J. E. Lennard-Jones, *P. Roy. Soc. A Math. Phy.* **1938**, *168*, 264–283.

[74] R. Parr, *Density-functional theory of atoms and molecules*, Oxford University Press Clarendon Press, New York, **1989**.

[75] R. Bader, *Atoms in Molecules: A Quantum Theory*, of *International series of monographs on chemistry*, Clarendon Press, Oxford, **1990**.

[76] P. Maxwell, A. Martín Pendás, P. L. A. Popelier, *Phys. Chem. Chem. Phys.* **2016**, *18*, 20986–21000.

[77] E. Francisco, J. L. Casals-Sainz, T. Rocha-Rinza, A. Martín Pendás, *Theor. Chem. Acc.* **2016**, *135:170*, 1–8.

[78] M. Marqués, M. Santoro, C. L. Guillaume, F. A. Gorelli, J. Contreras-García, R. T. Howie, A. F. Goncharov, E. Gregoryanz, *Phys. Rev. B* **2011**, *83*, 184106.

[79] J. P. Perdew, R. G. Parr, M. Levy, J. L. Balduz, *Phys. Rev. Lett.* **1982**, *49*, 1691–1694.

[80] M. J. Frisch, G. W. Trucks, H. B. Schlegel, G. E. Scuseria, M. A. Robb, J. R. Cheeseman, G. Scalmani, V. Barone, B. Mennucci, G. A. Petersson, H. Nakatsuji, M. Caricato, X. Li, H. P. Hratchian, A. F. Izmaylov, J. Bloino, G. Zheng, J. L. Sonnenberg, M. Hada, M. Ehara, K. Toyota, R. Fukuda, J. Hasegawa, M. Ishida, T. Nakajima, Y. Honda, O. Kitao, H. Nakai, T. Vreven, J. A. Montgomery, Jr., J. E. Peralta, F. Ogliaro, M. Bearpark, J. J. Heyd, E. Brothers, K. N. Kudin, V. N. Staroverov, R. Kobayashi, J. Normand, K. Raghavachari, A. Rendell, J. C. Burant, S. S. Iyengar, J. Tomasi, M. Cossi, N. Rega, J. M. Millam, M. Klene, J. E. Knox, J. B. Cross, V. Bakken, C. Adamo, J. Jaramillo, R. Gomperts, R. E. Stratmann, O. Yazyev, A. J. Austin, R. Cammi, C. Pomelli, J. W. Ochterski, R. L. Martin, K. Morokuma, V. G. Zakrzewski, G. A. Voth, P. Salvador, J. J. Dannenberg, S. Dapprich, A. D. Daniels, O. Farkas, J. B. Foresman, J. V. Ortiz, J. Cioslowski, D. J. Fox, *Gaussian 09 Revision E.01*, Gaussian Inc. Wallingford CT 2009.

[81] Q. Sun, T. C. Berkelbach, N. S. Blunt, G. H. Booth, S. Guo, Z. Li, J. Liu, J. D. McClain, E. R. Sayfutyarova, S. Sharma, S. Wouters, G. K. Chan, *PySCF: the Python based simulations of chemistry framework*, **2017**.

[82] A. Martín Pendás, E. Francisco, *Promolden. A QTAIM/IQA code (Avaliable from the authors upon request).*

[83] Y. Zhao, D. G. Truhlar, *Theor. Chem. Acc.* **2008**, *120*, 215–241.

[84] I. Alkorta, J. C. R. Thacker, P. L. A. Popelier, *J. Comput. Chem.* **2018**, *39*, 546–556.

[85] P. Politzer, J. R. Reimers, J. S. Murray, A. Toro-Labbé, *J. Phys. Chem. Let.* **2010**, *1*, 2858–2862.

[86] J. Martínez, A. Toro-Labbé, *J. Math. Chem.* **2009**, *45*, 911–927.

[87] S. Giri, E. Echegaray, P. W. Ayers, A. S. Nuñez, F. Lund, A. Toro-Labbé, *J. Phys. Chem. A* **2012**, *116*, 10015–10026, PMID: 22974407.

[88] P. Politzer, J. V. Burda, M. C. Concha, P. Lane, J. S. Murray, *J. Phys. Chem. A* **2006**, *110*, 756–761, PMID: 16405350.

Supporting Information

Energetic descriptors of steric hindrance in real space: an improved IQA picture †

Miguel Gallegos González, Aurora Costales, Ángel Martín Pendás.

Contents

1 Further computational details

1.1 IQA calculations

The IQA analysis and energy terms along the different studies were obtained using the in-house code PROMOLDEN [1] without employing explicit symmetry options. β-spheres were used throughout. Out-β integrations used used 451 points Gauss-Legendre radial quadratures with maximum $L = 12$ and 5810 angular Lebedev quadratures. In-β integrations were performed using 451 points Gauss-Chebychev radial quadratures and L was decreased to 10. The Lebedev grid was not changed.

2 Artificial compression of the He atom

2.1 Rigid scan of the He_2 dimer

The evolution of the intra-atomic energy of the He atom, in addition to its constituting IQA components, was evaluated along the rigid compression of two He atoms in the He_2 dimer. For such a purpose a frozen scan was performed with separations between the atoms ranging from 0.50 Å to 2.50 Å in steps of 0.10 Å as shown in the following figure.

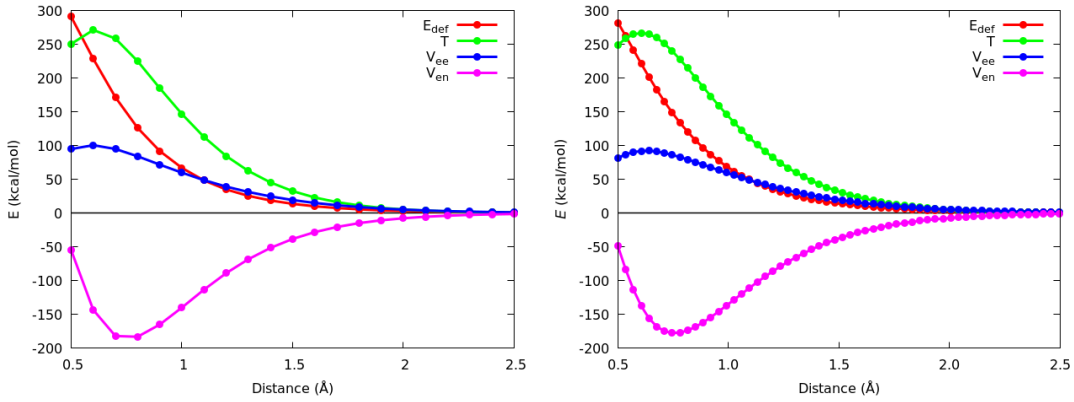

Figure 1: Evolution of the E_{def}, T, V_{ee} and V_{en} energetic components of the He atom along the frozen compression of the He_2 dimer. Calculations performed in the gas phase at the HF/aug-cc-pVDZ (left) and CASSCF(4,18)/aug-cc-pVDZ (right) levels of theory. The energies reported as relative magnitudes with respect to the values corresponding to the He atom in vacuum.

Notice that the results obtained for any of the employed methodologies are, as expected, nearly identical.
In Fig. 2.1 it is also clear that the limited active space is able to show a dispersion minimum in roughly at roughly the appropriate internuclear distance in agreement with previously reported data [2]

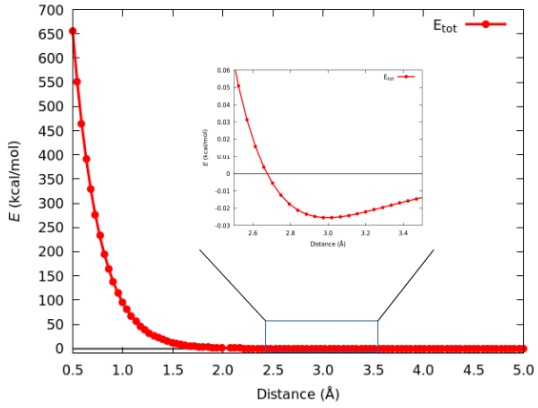

Figure 2: Evolution of the total energy of the He_2 dimer along the frozen scan evaluated in the gas phase and at the CASSCF(4,18)/aug-cc-pVDZ level of theory.

2.2 Confinement through an external parabolic potential

An artificial confinement of the He atom was enforced through the application of a uniform isotropic parabolic potential centered at the nucleus.

$$\hat{H} = \hat{H}_0 + \frac{1}{2}k\hat{r}^2.$$

All calculations were performed in the gas phase at the CASSCF/aug-cc-pVDZ level of theory using the PySCF [3] quantum chemistry package. Figure 2.2 shows a k-E_{def} equivalence by mapping the deformation energy of the helium atom in the He_2 diatomic to that found at a given k driven confinement. Stronger confinements correspond, as expected, to larger harmonic constants.

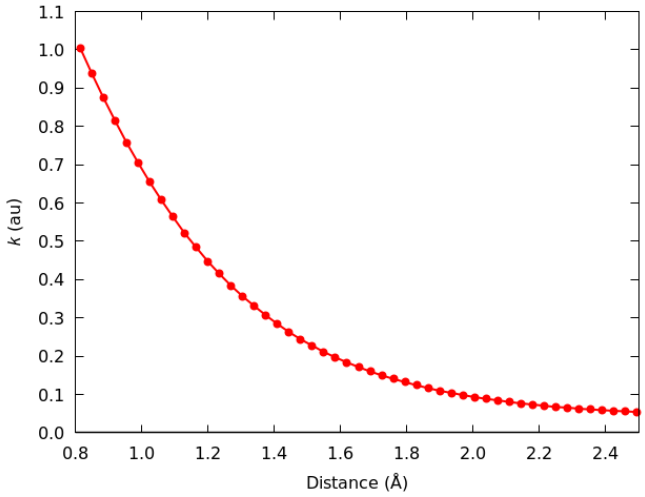

Figure 3: Relation between the parabolic potential equivalent force constant k and the interatomic distance along the compression of the He_2 dimer.

3 Methane dimer (CH_4-CH_4) frozen compression

The current section collects the IQA analysis of the methane dimer. The reported calculations were performed at the DFT (B3LYP), HF and CASSCF (12,8) methods in combinations with the aug-cc-pVDZ basis set in the gas phase. The inner H atoms are those which are directly facing the opposite monomer, thus directly engaged in congestion, whereas the outer H atoms are the ones pointing outwards. The abscissas reported in the graphs corresponds to the distance between the C atoms of both monomers.

3.1 Intra-atomic components

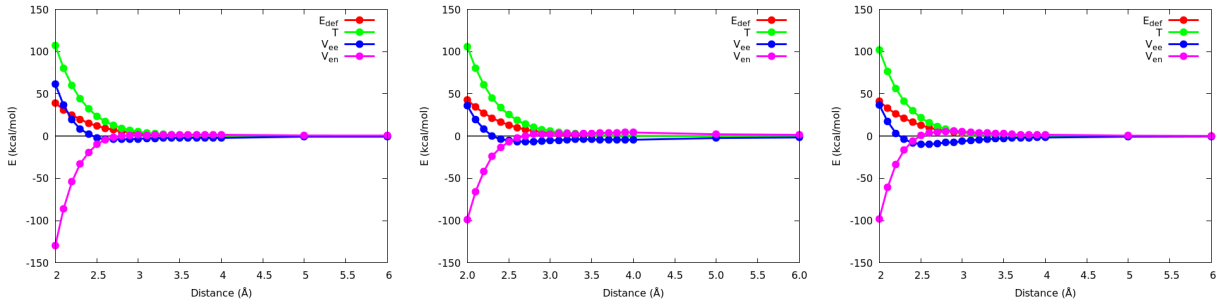

Figure 4: Deformation energy E_{def}, kinetic energy T, electron-electron repulsion V_{ee} and electron-nucleus attraction V_{en} at the CASSCF, DFT and HF levels of theory for the C atom.

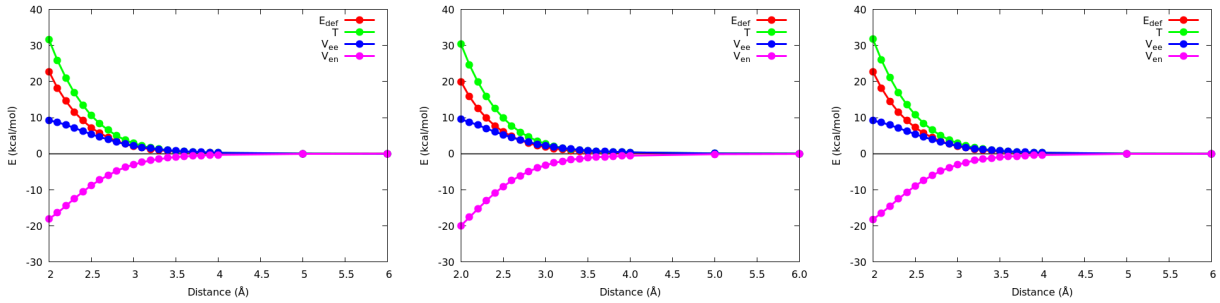

Figure 5: Deformation energy E_{def}, kinetic energy T, electron-electron repulsion V_{ee} and electron-nucleus attraction V_{en} at the CASSCF, DFT and HF levels of theory for the inner H atoms.

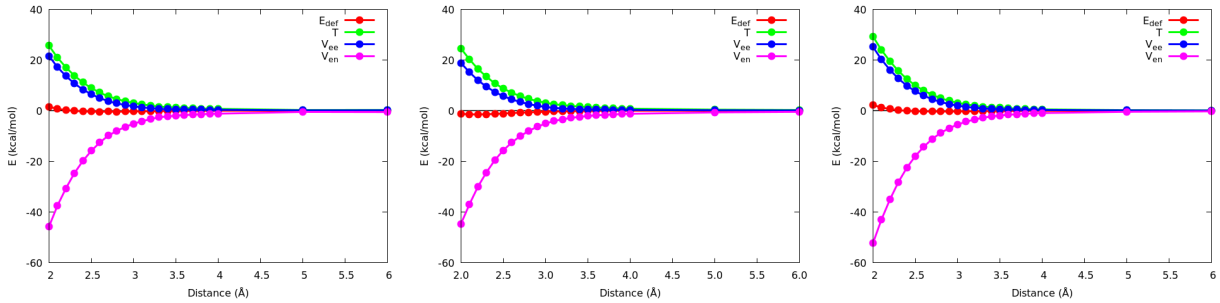

Figure 6: Deformation energy E_{def}, kinetic energy T, electron-electron repulsion V_{ee} and electron-nucleus attraction V_{en} at the CASSCF, DFT and HF levels of theory for the outer H atoms.

3.2 Deformation energies

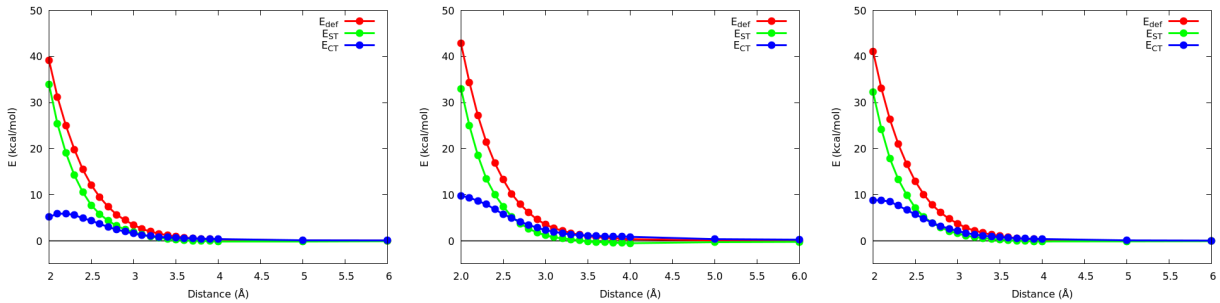

Figure 7: Deformation energy E_{def}, charge transfer term E_{CT} and steric energy E_{ST} at the CASSCF, DFT and HF levels of theory for the C atom.

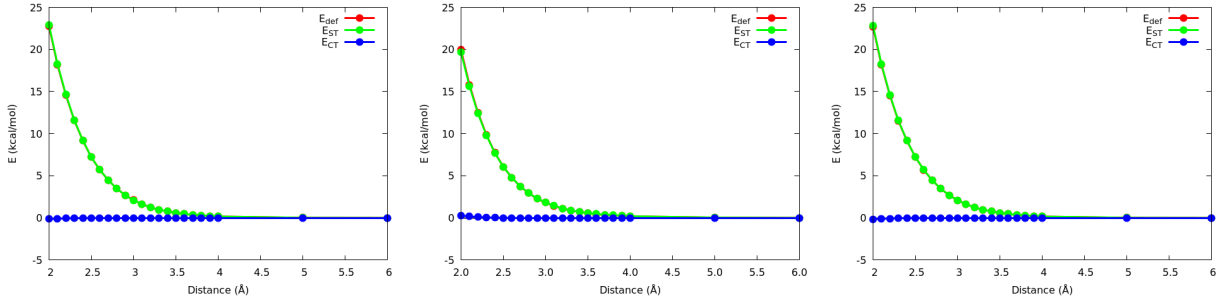

Figure 8: Deformation energy E_{def}, charge transfer term E_{CT} and steric energy E_{ST} at the CASSCF, DFT and HF levels of theory for the inner H atoms.

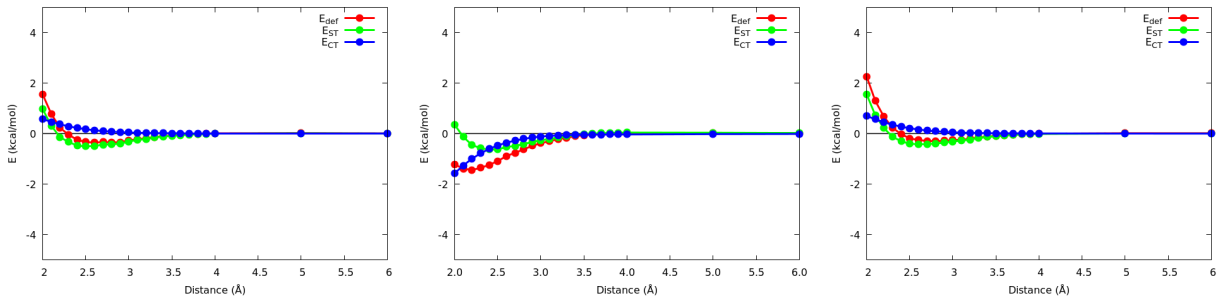

Figure 9: Deformation energy E_{def}, charge transfer term E_{CT} and steric energy E_{ST} at the CASSCF, DFT and HF levels of theory for the outer H atoms.

As it can be seen in the previous figures, charge transfer effects represent only a small contribution to the total deformation energies, a contribution which increases as the separation between the monomers is reduced due to the increasing values of ΔQ. Moreover, as a general trend, the steric energy behaves analogously to the deformation energy with the inter-atomic distance between the approaching monomers, fitting in both cases to the well-known Buckingham potential (see section 3.5). It should be noticed that in the case of the outer H atoms, both the deformation and steric energies get slightly negative values at any of the employed levels of theory. This result is, however, not very significant since the outer H atoms get very slightly deformed along the scan and hence such values can be considered to be within the typical margin of error of this kind of calculations. Moreover it is worth mentioning that, as it can be seen from the previous figures, the E_{CT} term evaluated at the CASSCF and HF methodologies may differ from the one obtained under DFT, something which can be explained considering the difference in the atomic charges when estimated at these different levels of theory.

3.3 Total deformation energy of the methane monomer

As shown in Fig. 10, the total deformation energy of the CH_4 molecule decays exponentially with the inter-atomic distances, in agreement with the already mentioned Buckingham potential (see section 3.5). On the other hand, any of the employed methodologies yielded nearly identical results.

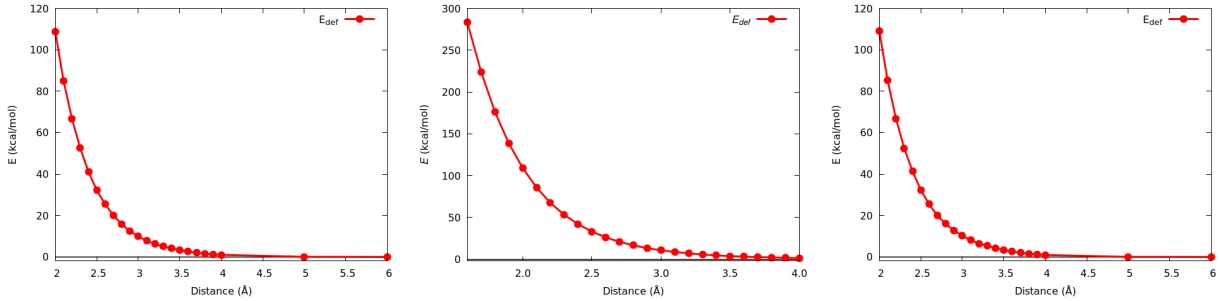

Figure 10: Total deformation energy E_{def} at the CASSCF, DFT and HF levels of theory for the CH_4 molecule.

3.4 Change in the atomic charges, ΔQ

The following tables show the evolution of the atomic charges of the constituting atoms of the methane monomer along the frozen scan.

Level of theory	Q(C) (au)	$Q(\mathrm{H})_{in}$ (au)	$Q(\mathrm{H})_{out}$ (au)
CASSCF(12,8)/aug-cc-pVDZ	0.31	-0.08	-0.06
B3LYP/aug-cc-pVDZ	0.10	-0.03	-0.02
HF/aug-cc-pVDZ	0.31	-0.08	-0.08

Table 1: Table collecting the atomic charges at the reference point (10 Å of separation between the monomers) computed at different levels of theory.

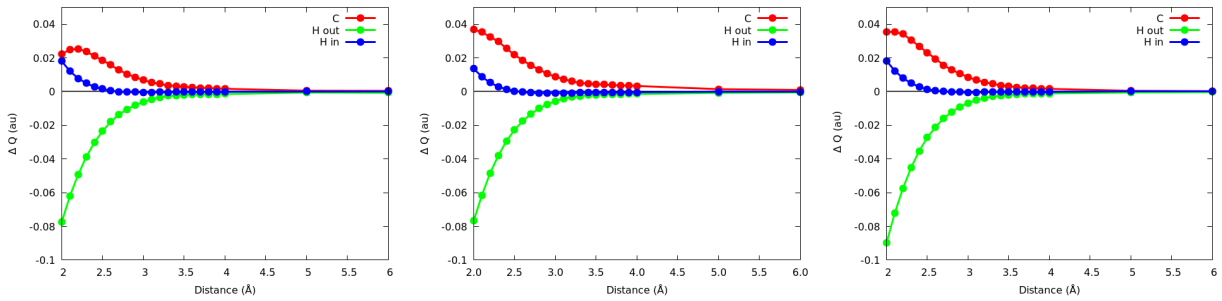

Figure 11: Change in the atomic charge at the CASSCF, DFT and HF levels of theory for the CH_4 molecule.

As shown, the atomic charges computed at the HF and CASSCF levels of theory are very similar to one another, being at the same time considerably different from the nominal values computed with DFT. However, as expected, the ΔQ values exhibit an analogous behavior with the distance for any of the methodologies.

3.5 Buckingham potential fittings

We collect here results from fitting certain energetic components, particularly the E_{def} and E_{ST} energies to Buckingham potentials,

$$V(r) = A \cdot exp(-B \cdot r), \tag{1}$$

being r the separation between the approaching monomers.
Considering the low dependency of E_{def}'s with the level of theory, only B3LYP/aug-cc-pVDZ results are shown.

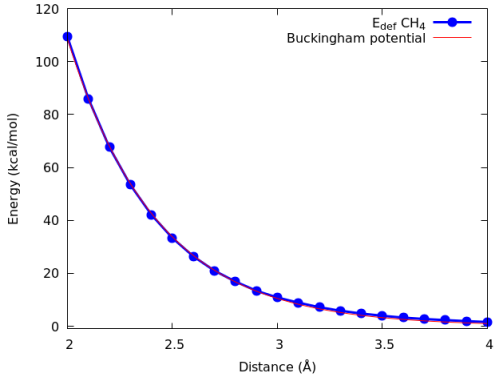

Figure 12: Total deformation energy of the CH_4 monomer along the compression process evaluated at the B3LYP/aug-cc-pVDZ level of theory in the gas phase along with the optimized fitting. A = 11610.20 kcal/mol, B = 2.33 $Å^{-1}$, RMS of residuals = 0.57 kcal/mol.

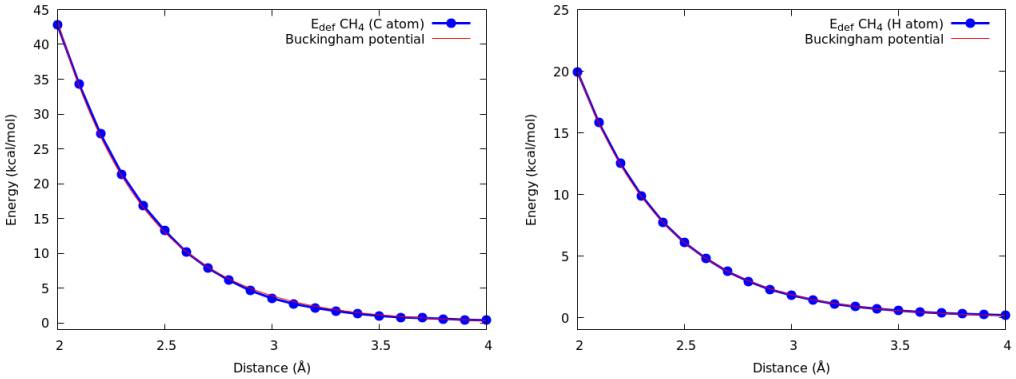

Figure 13: Total deformation energy of the C atom (left) and inner H atom (right) of the CH_4 monomer along the compression process evaluated at the B3LYP/aug-cc-pVDZ level of theory in the gas phase along with the optimized fitting. A = 5328.82 and 2347.78 kcal/mol, B = 2.41 and 2.38 $Å^{-1}$, RMS of residuals = 0.26 and 0.04 kcal/mol respectively.

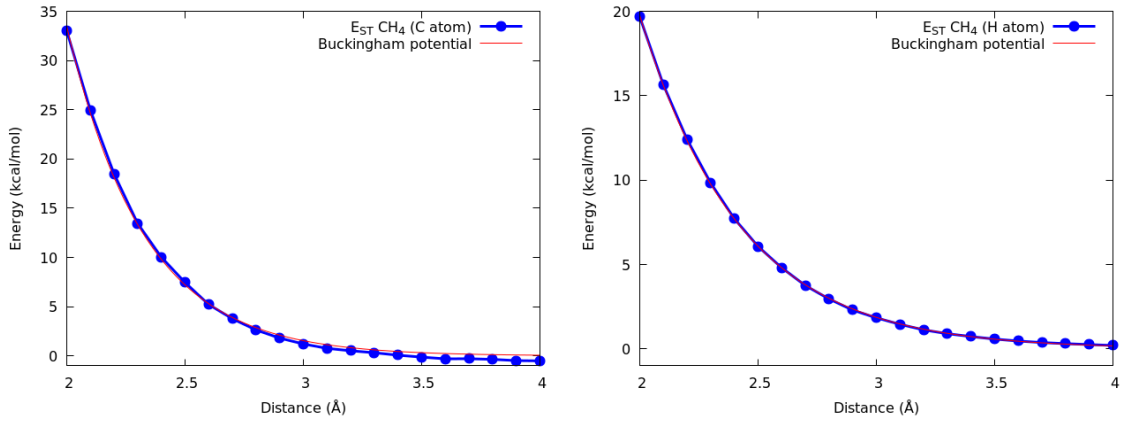

Figure 14: Steric energy of the C atom (left) and inner H atom (right) of the CH_4 monomer along the compression evaluated at the B3LYP/aug-cc-pVDZ level of theory in the gas phase along with the optimized fitting. A = 15579.60 and 2202.03 kcal/mol, B = 3.07 and 2.36 $Å^{-1}$, RMS of residuals = 0.39 and 0.04 kcal/mol respectively.

4 Ammonia dimer (NH_3-NH_3) compression

The current section collects the IQA analyses of the ammonia molecule along the frozen and relaxed scans corresponding to a total of 4 different types of approximations. The reported calculations were performed at the B3LYP/aug-cc-pVDZ and HF/aug-cc-pVDZ levels of theory in the gas phase. Graph abscissas correspond to the distance between the two N atoms.

4.1 Frozen compression

4.1.1 Intra-atomic components

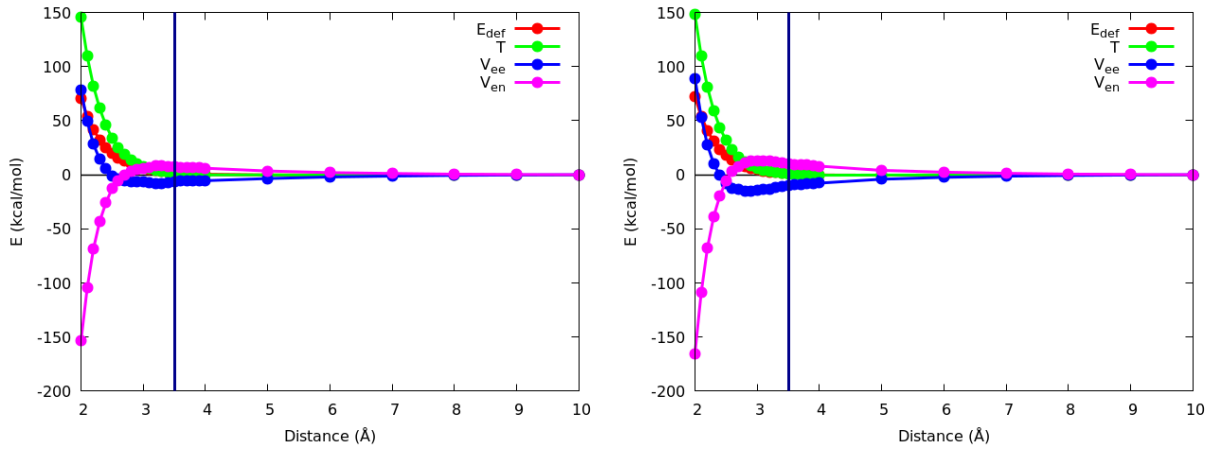

Figure 15: Deformation energy E_{def}, kinetic energy T, electron-electron repulsion V_{ee} and electron-nucleus attraction V_{en} at the DFT and HF levels of theory for the N atom in the H-H eclipsed conformation.

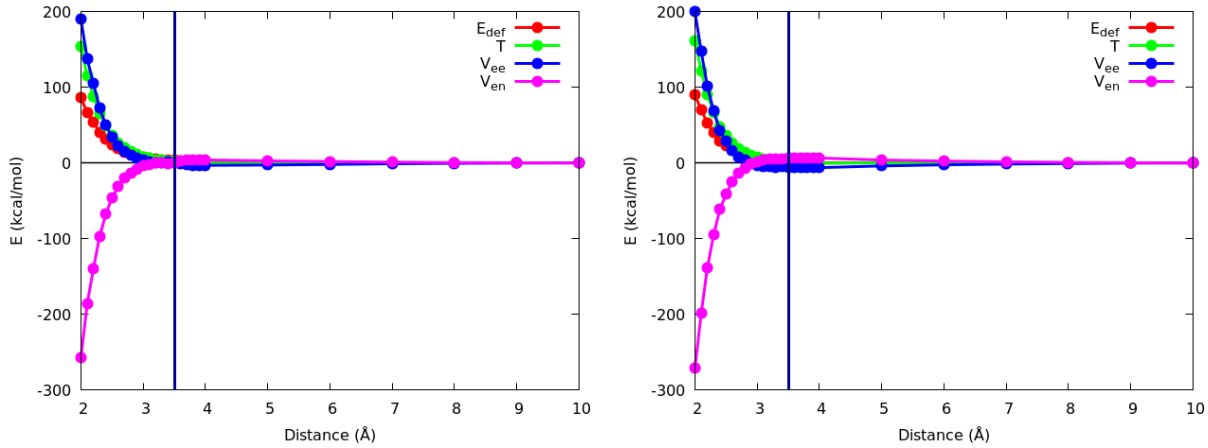

Figure 16: Deformation energy E_{def}, kinetic energy T, electron-electron repulsion V_{ee} and electron-nucleus attraction V_{en} at the DFT and HF levels of theory for the N atom in the H-H staggered conformation.

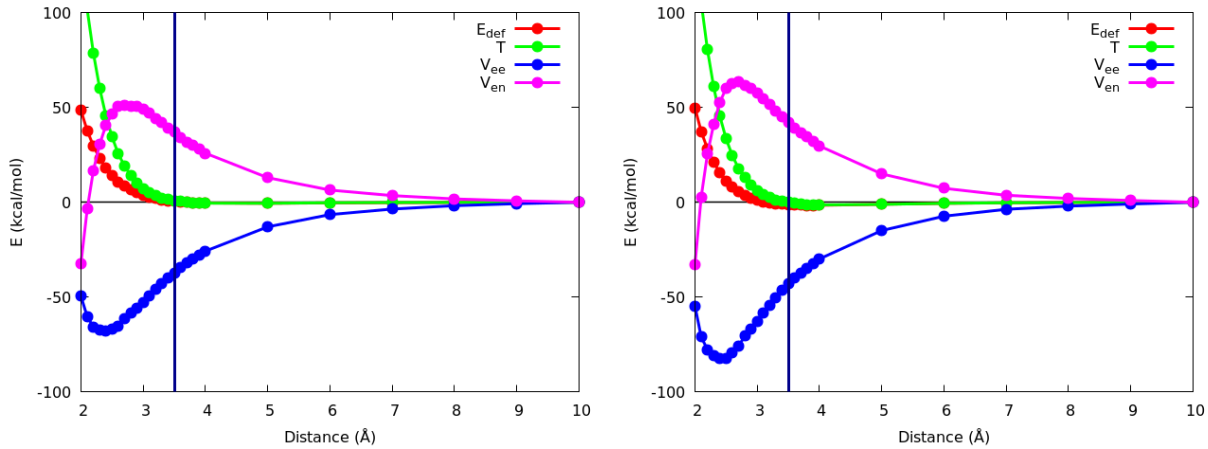

Figure 17: Deformation energy E_{def}, kinetic energy T, electron-electron repulsion V_{ee} and electron-nucleus attraction V_{en} at the DFT and HF levels of theory for the N atom in the N-N eclipsed conformation.

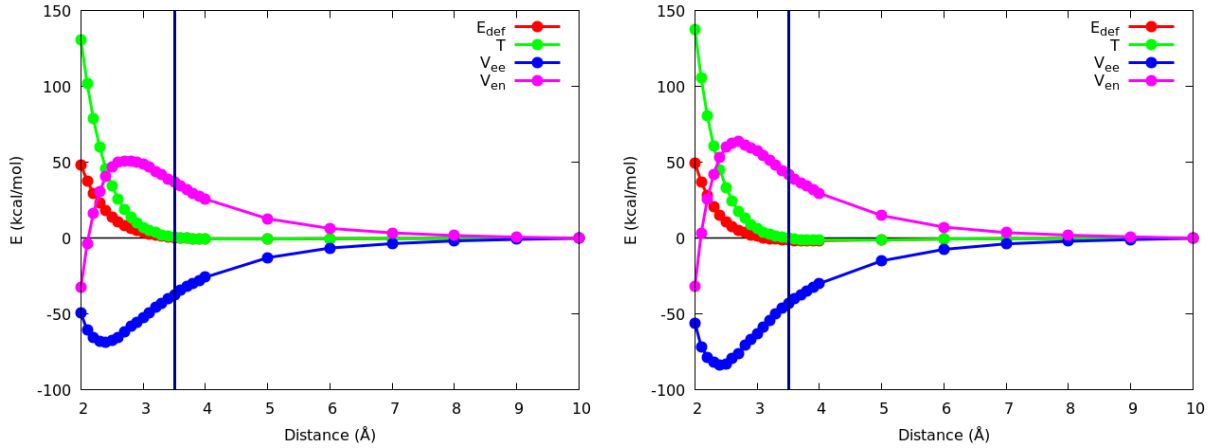

Figure 18: Deformation energy E_{def}, kinetic energy T, electron-electron repulsion V_{ee} and electron-nucleus attraction V_{en} at the DFT and HF levels of theory for the N atom in the N-N staggered conformation.

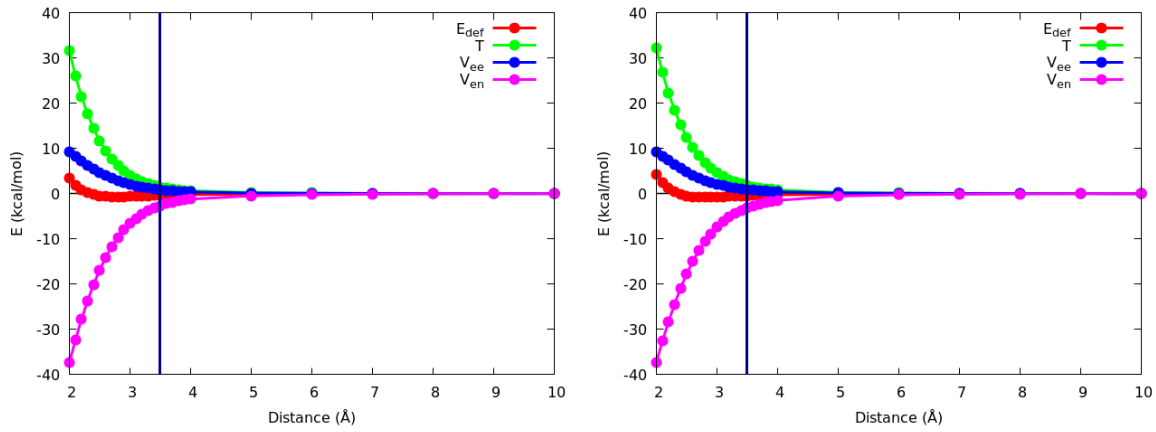

Figure 19: Deformation energy E_{def}, kinetic energy T, electron-electron repulsion V_{ee} and electron-nucleus attraction V_{en} at the DFT and HF levels of theory for the H atom in the H-H eclipsed conformation.

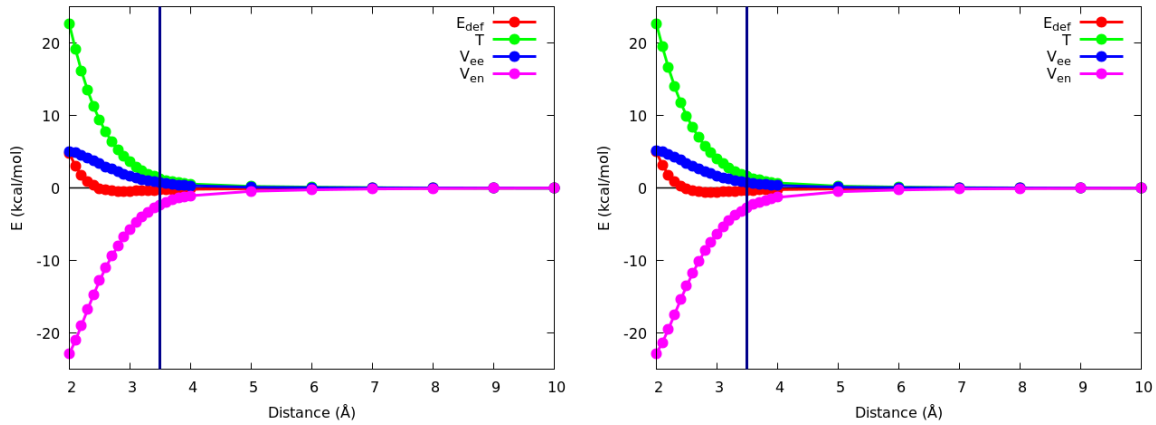

Figure 20: Deformation energy E_{def}, kinetic energy T, electron-electron repulsion V_{ee} and electron-nucleus attraction V_{en} at the DFT and HF levels of theory for the H atom in the H-H staggered conformation.

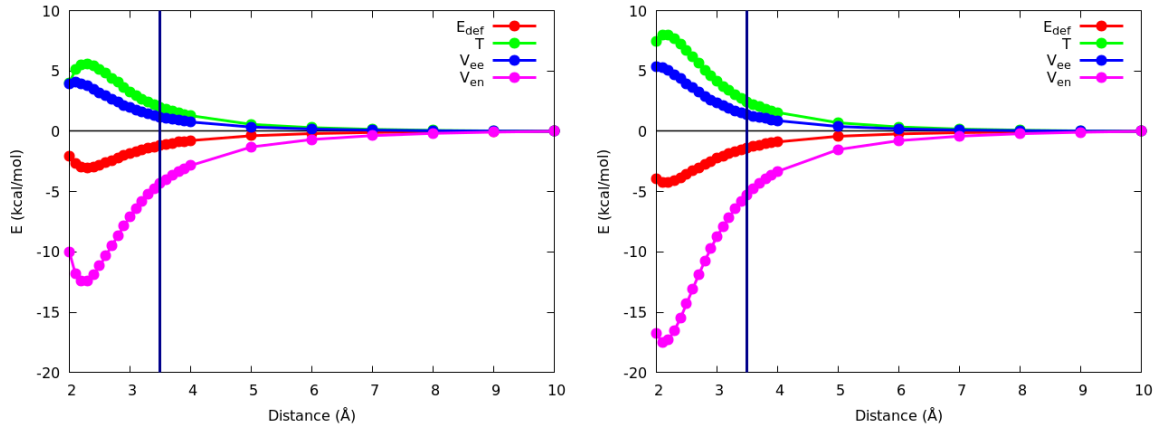

Figure 21: Deformation energy E_{def}, kinetic energy T, electron-electron repulsion V_{ee} and electron-nucleus attraction V_{en} at the DFT and HF levels of theory for the H atom in the N-N eclipsed conformation.

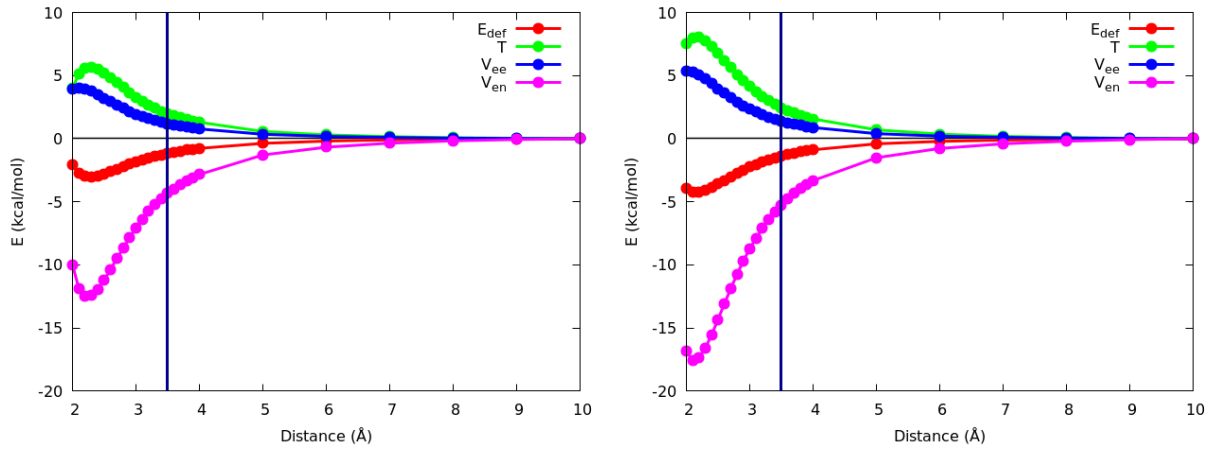

Figure 22: Deformation energy E_{def}, kinetic energy T, electron-electron repulsion V_{ee} and electron-nucleus attraction V_{en} at the DFT and HF levels of theory for the H atom in the N-N staggered conformation.

4.1.2 Deformation energies

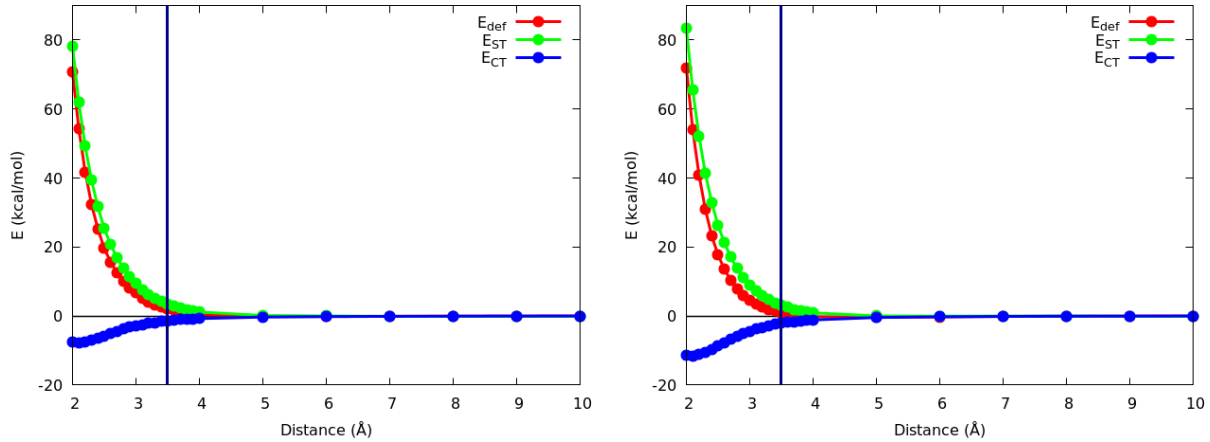

Figure 23: Deformation energy E_{def}, charge transfer term E_{CT} and steric energy E_{ST} at the DFT and HF levels of theory for the N atom in the H-H eclipsed NH_3 dimer.

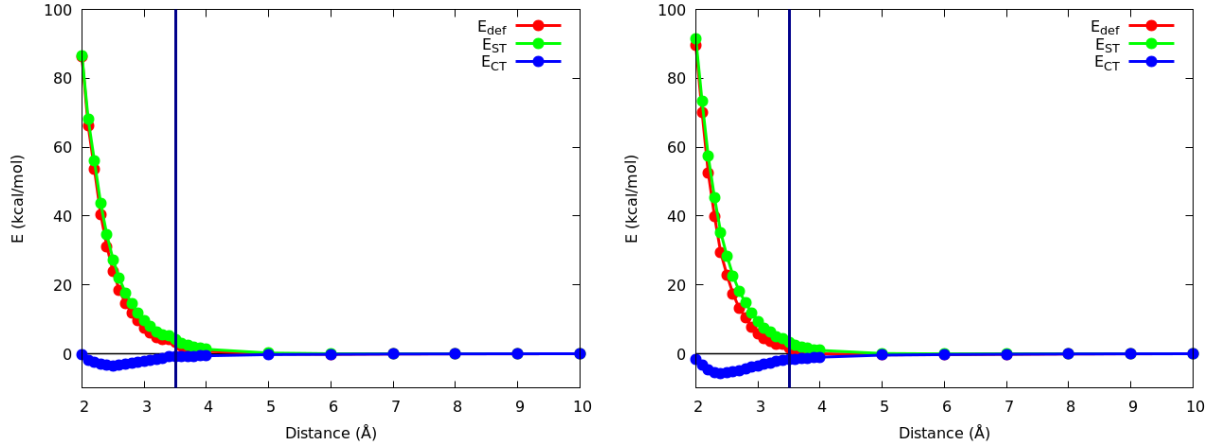

Figure 24: Deformation energy E_{def}, charge transfer term E_{CT} and steric energy E_{ST} at the DFT and HF levels of theory for the N atom in the H-H staggered NH_3 dimer.

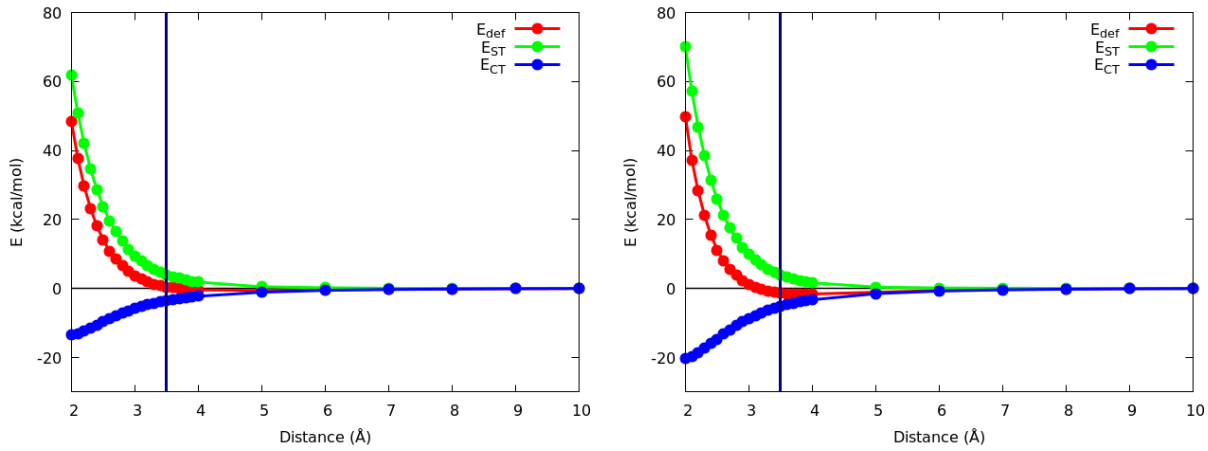

Figure 25: Deformation energy E_{def}, charge transfer term E_{CT} and steric energy E_{ST} at the DFT and HF levels of theory for the N atom in the N-N eclipsed NH_3 dimer.

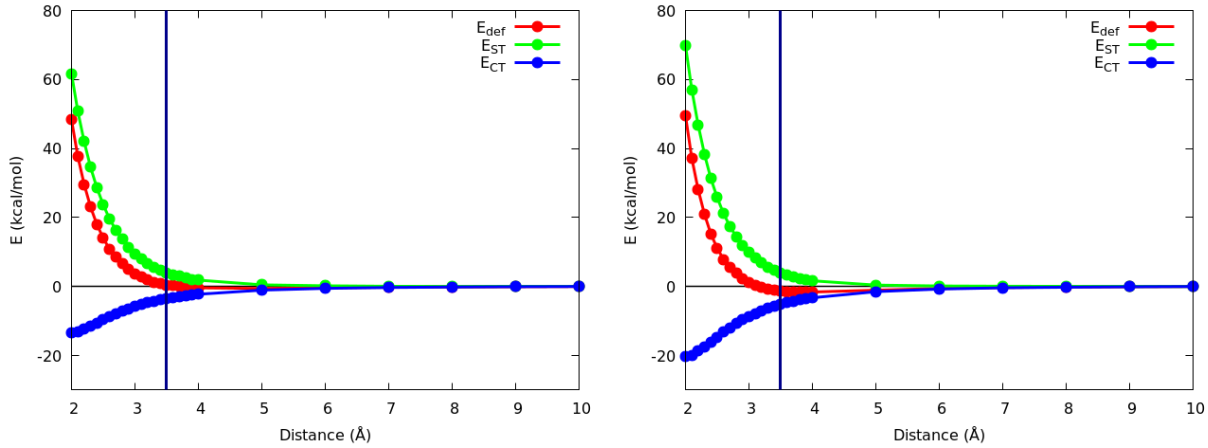

Figure 26: Deformation energy E_{def}, charge transfer term E_{CT} and steric energy E_{ST} at the DFT and HF levels of theory for the N atoms in the N-N staggered NH_3 dimer.

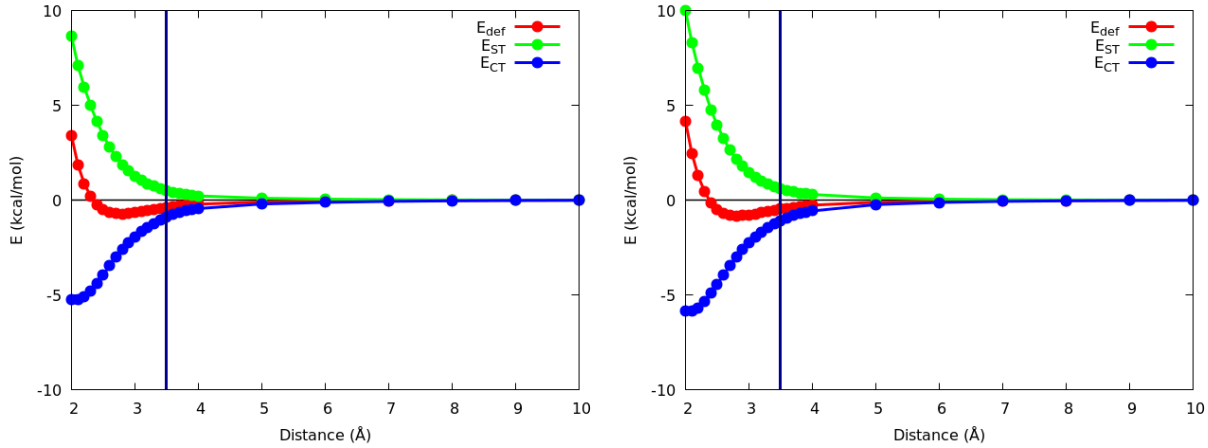

Figure 27: Deformation energy E_{def}, charge transfer term E_{CT} and steric energy E_{ST} at the DFT and HF levels of theory for the H atom in the H-H eclipsed NH_3 dimer.

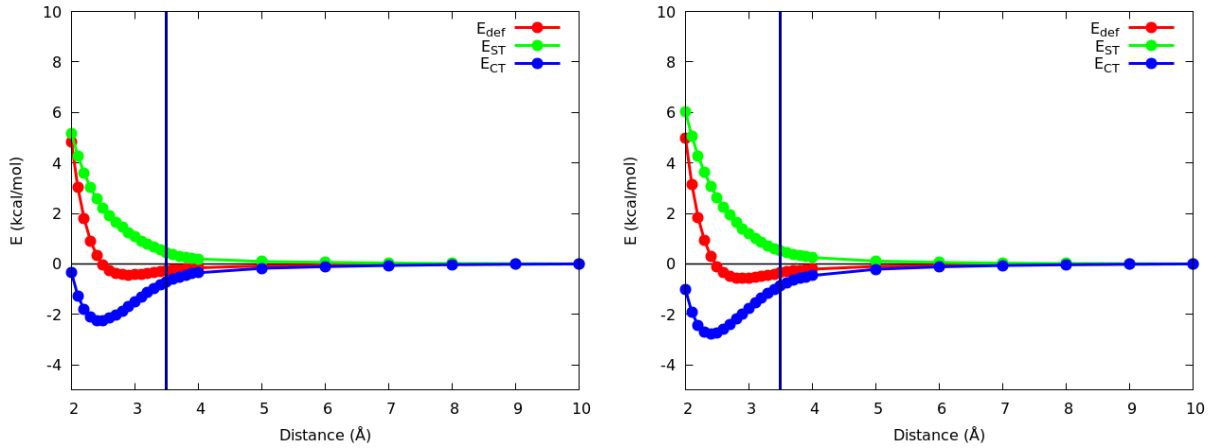

Figure 28: Deformation energy E_{def}, charge transfer term E_{CT} and steric energy E_{ST} at the DFT and HF levels of theory for the H atom in the H-H staggered NH_3 dimer.

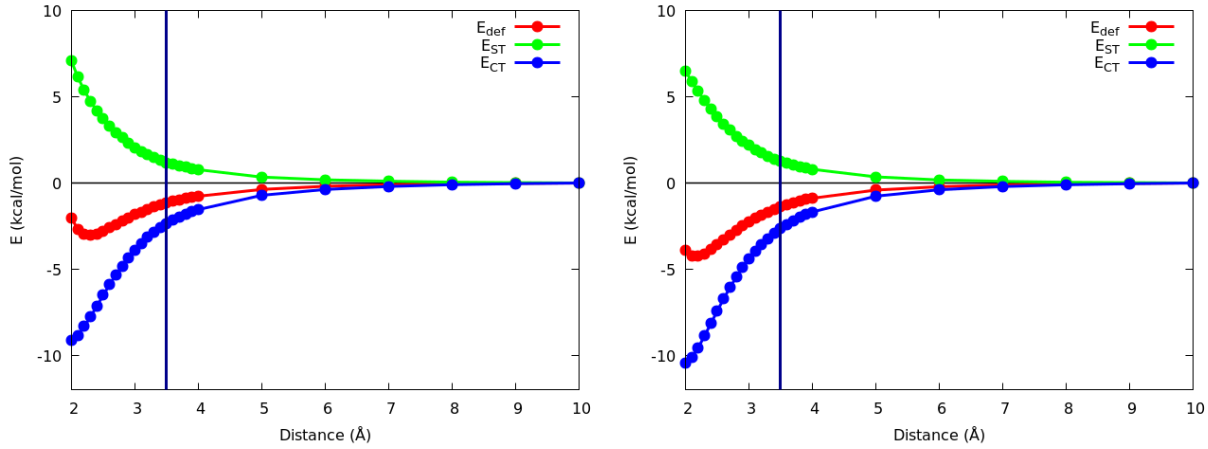

Figure 29: Deformation energy E_{def}, charge transfer term E_{CT} and steric energy E_{ST} at the DFT and HF levels of theory for the H atom in the N-N eclipsed NH_3 dimer.

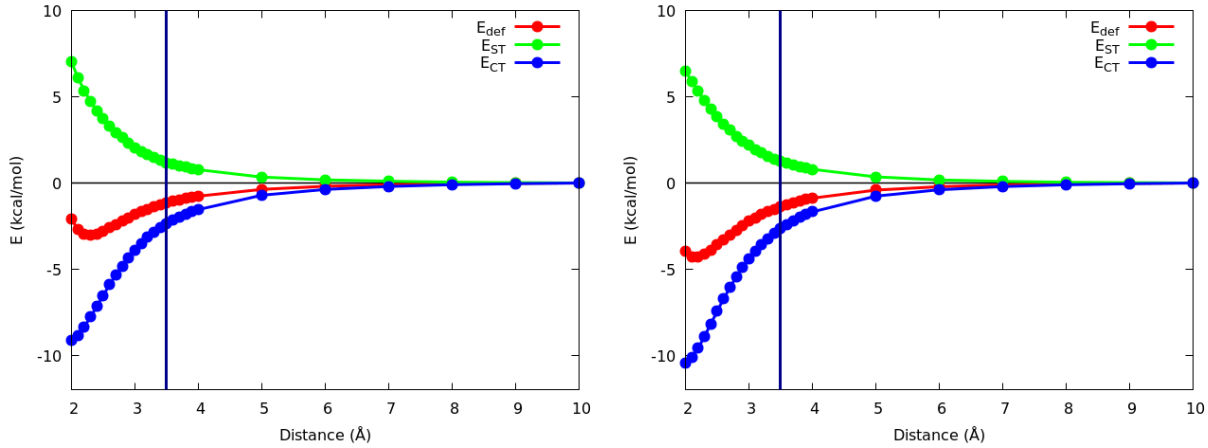

Figure 30: Deformation energy E_{def}, charge transfer term E_{CT} and steric energy E_{ST} at the DFT and HF levels of theory for the H atoms in the N-N staggered NH_3 dimer.

4.1.3 Total deformation energy of the ammonia monomer

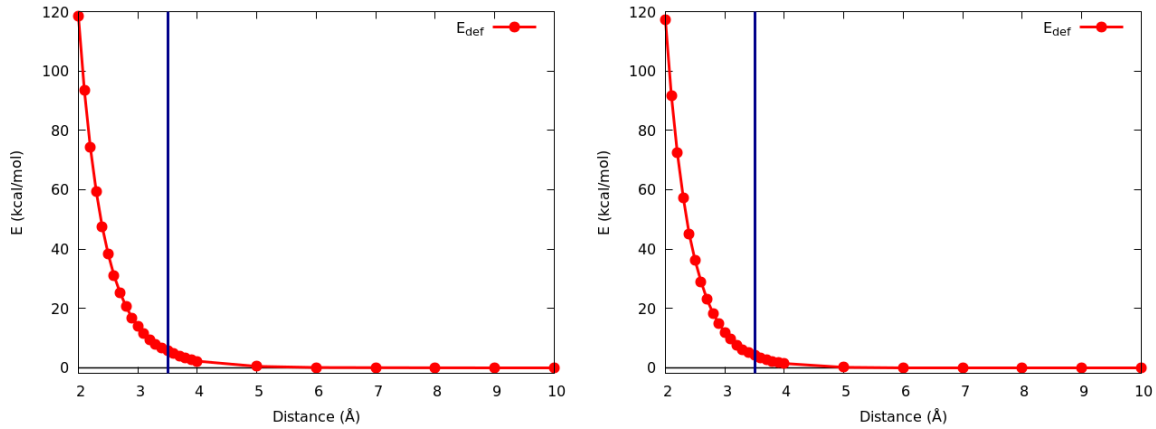

Figure 31: Total deformation energy E_{def} at the DFT and HF levels of theory for the NH_3 molecule in the H-H eclipsed approach.

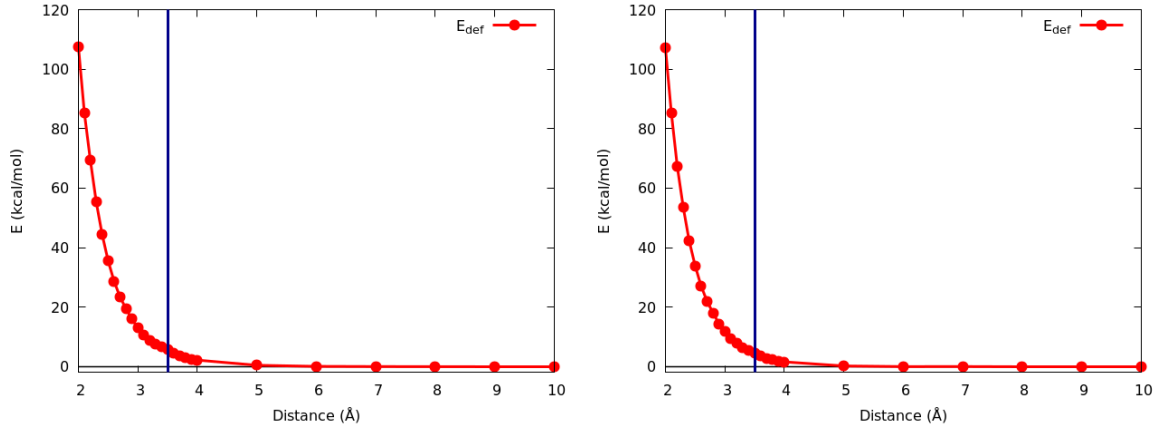

Figure 32: Total deformation energy E_{def} at the DFT and HF levels of theory for the NH_3 molecule in the H-H staggered approach.

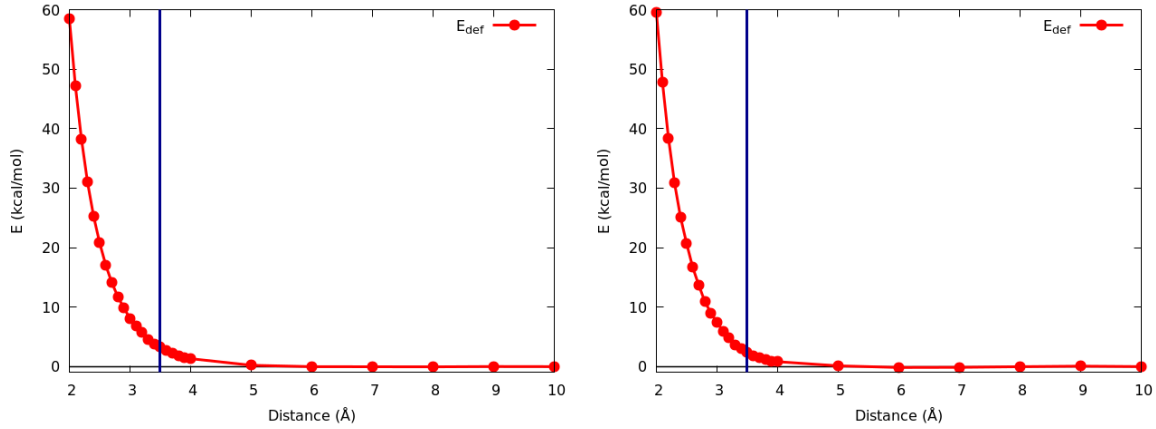

Figure 33: Total deformation energy E_{def} at the DFT and HF levels of theory for the NH_3 molecule in the N-N eclipsed approach.

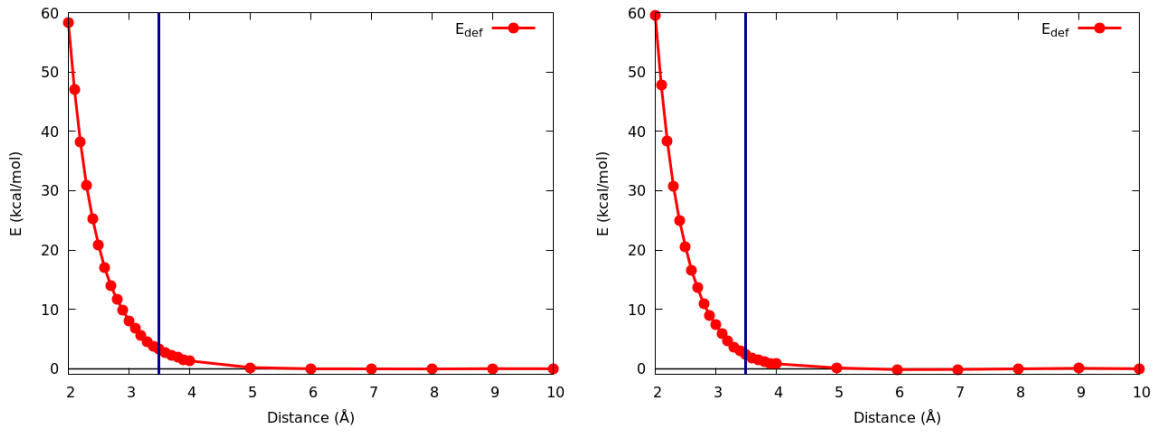

Figure 34: Total deformation energy E_{def} at the DFT and HF levels of theory for the NH_3 molecule in the N-N staggered approach.

4.1.4 Atomic charges, ΔQ

The following figures and tables show the evolution of the atomic charges of the constituting atoms of the ammonia monomer along the frozen scan.

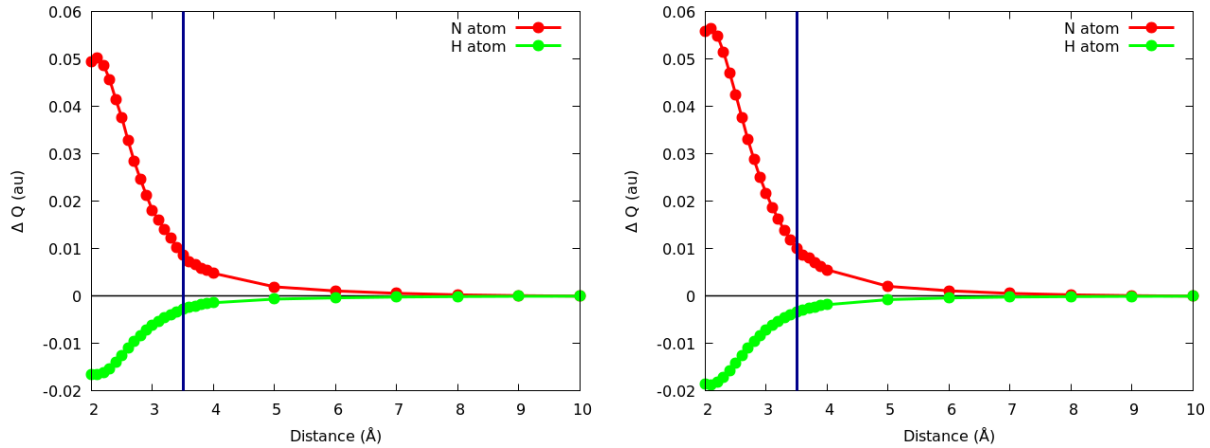

Figure 35: Change in the atomic charge at the DFT and HF levels of theory for the H-H eclipsed approximation.

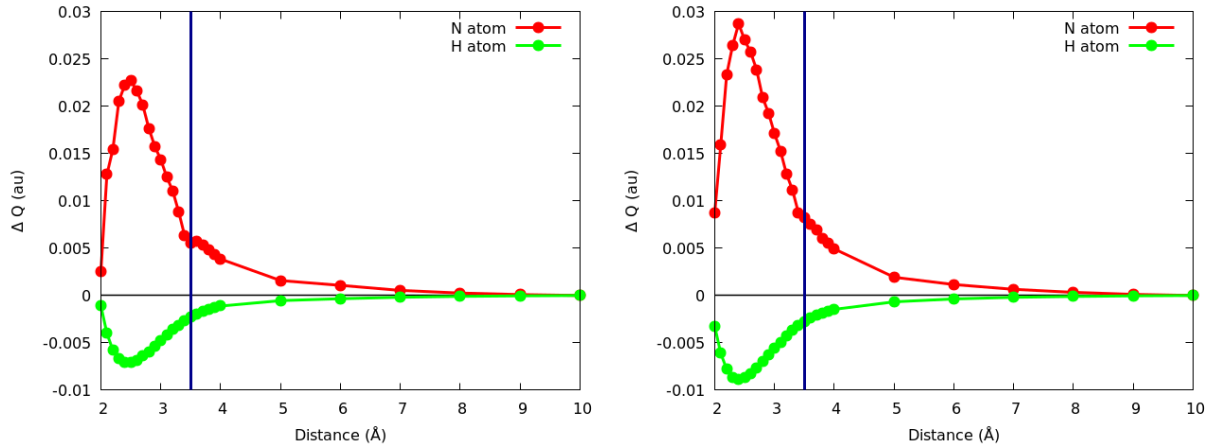

Figure 36: Change in the atomic charge at the DFT and HF levels of theory for the H-H staggered approximation.

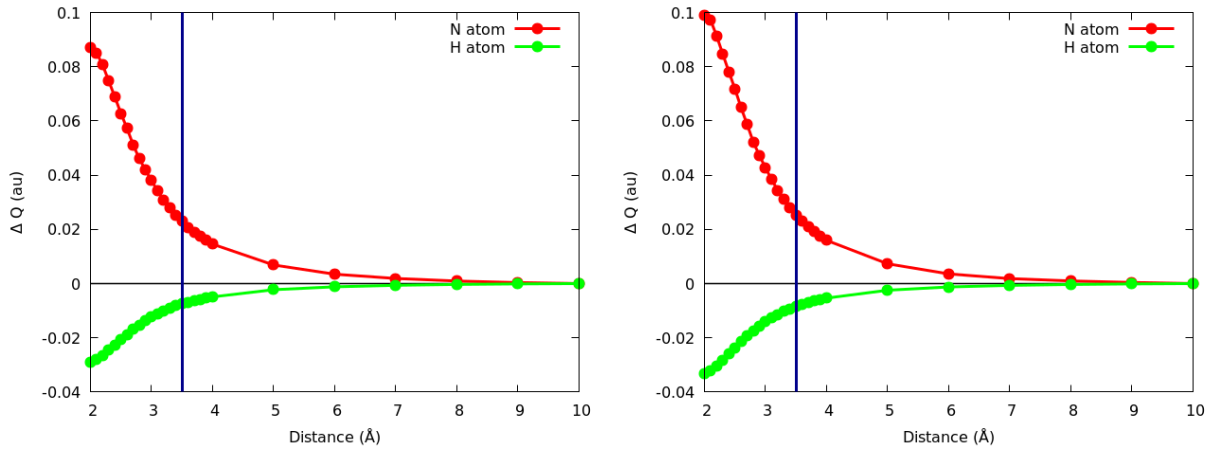

Figure 37: Change in the atomic charge at the DFT and HF levels of theory for the N-N eclipsed approximation.

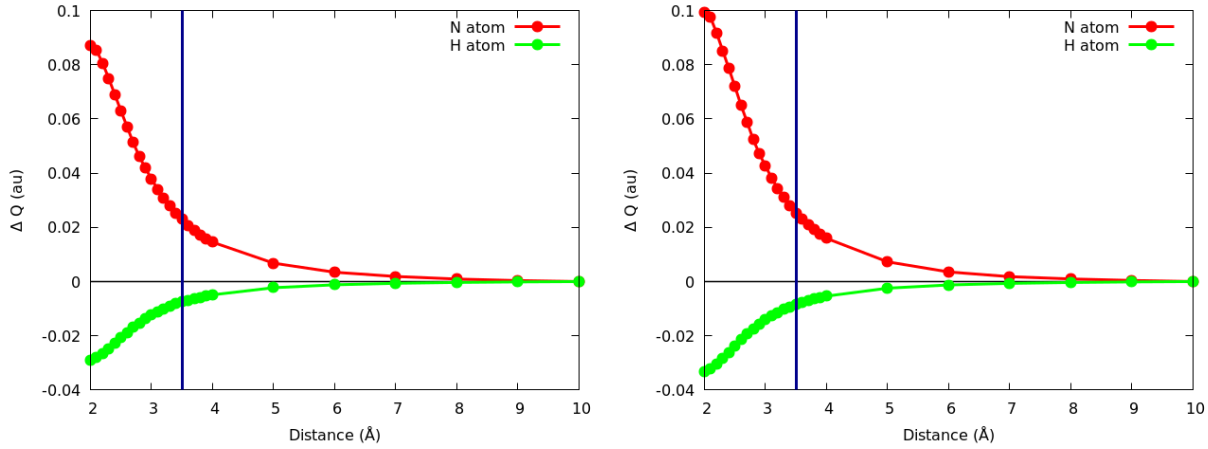

Figure 38: Change in the atomic charge at the DFT and HF levels of theory for the N-N staggered approximation.

Conformation	Level of theory	Q(N) (au)	Q(H) (au)
H-H (e)	B3LYP/aug-cc-pVDZ	-1.15	0.38
H-H (e)	HF/aug-cc-pVDZ	-1.22	0.41
H-H (s)	B3LYP/aug-cc-pVDZ	-1.15	0.38
H-H (s)	HF/aug-cc-pVDZ	-1.22	0.41
N-N (e)	B3LYP/aug-cc-pVDZ	-1.15	0.38
N-N (e)	HF/aug-cc-pVDZ	-1.22	0.41
N-N (s)	B3LYP/aug-cc-pVDZ	-1.15	0.38
N-N (s)	HF/aug-cc-pVDZ	-1.22	0.41

Table 2: Table collecting the atomic charges at the reference point (10 Å of separation between the monomers) computed at different levels of theory.

4.2 Relaxed compression

4.2.1 Intra-atomic components

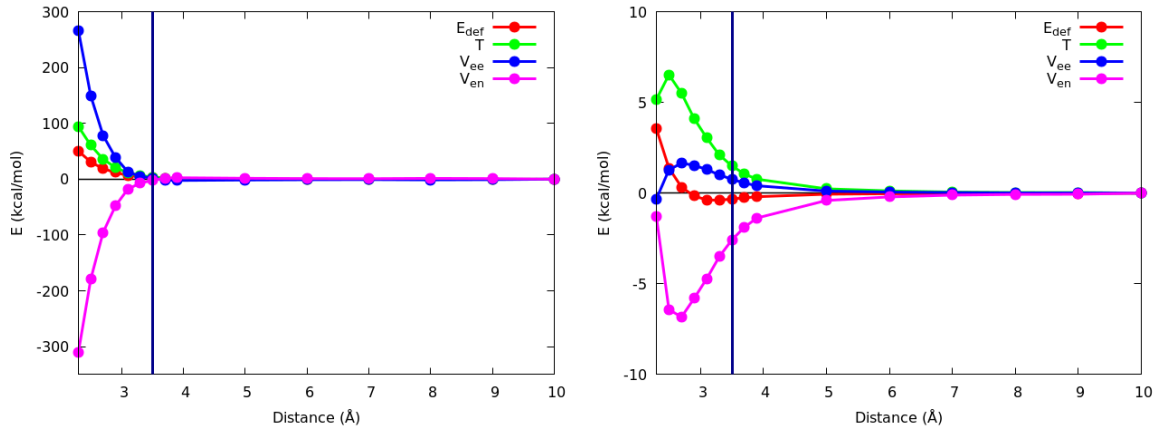

Figure 39: Deformation energy E_{def}, kinetic energy T, electron-electron repulsion V_{ee} and electron-nucleus attraction V_{en} at the DFT level of theory for the N atom (left) and H atom (right) in the H-H eclipsed conformations.

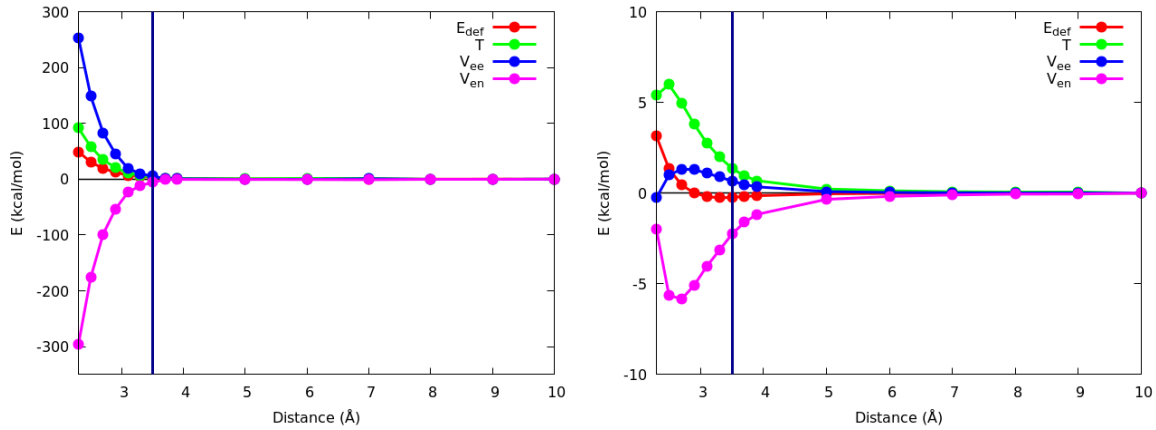

Figure 40: Deformation energy E_{def}, kinetic energy T, electron-electron repulsion V_{ee} and electron-nucleus attraction V_{en} at the DFT level of theory for the N atom (left) and H atom (right) in the H-H staggered conformations.

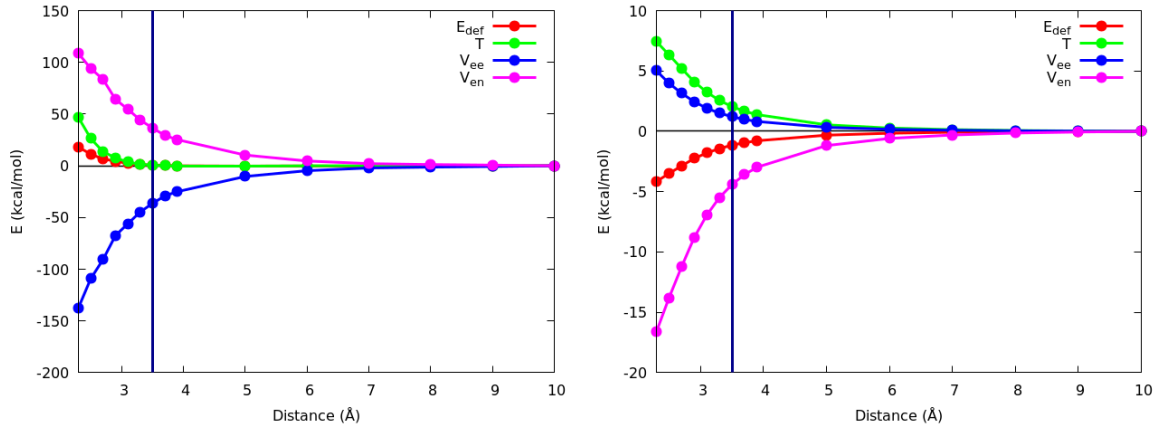

Figure 41: Deformation energy E_{def}, kinetic energy T, electron-electron repulsion V_{ee} and electron-nucleus attraction V_{en} at the DFT level of theory for the N atom (left) and H atom (right) in the N-N eclipsed conformations.

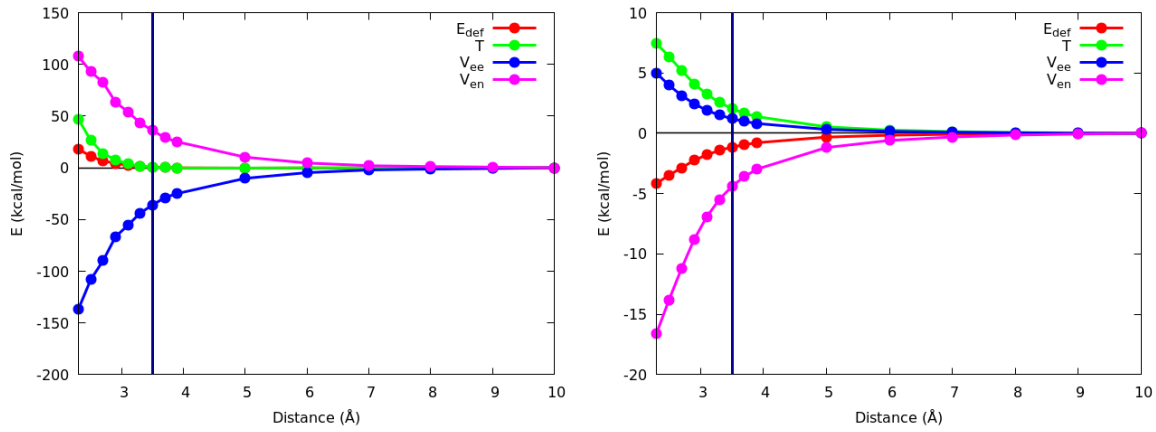

Figure 42: Deformation energy E_{def}, kinetic energy T, electron-electron repulsion V_{ee} and electron-nucleus attraction V_{en} at the DFT level of theory for the N atom (left) and H atom (right) in the N-N staggered conformations.

4.2.2 Deformation energies

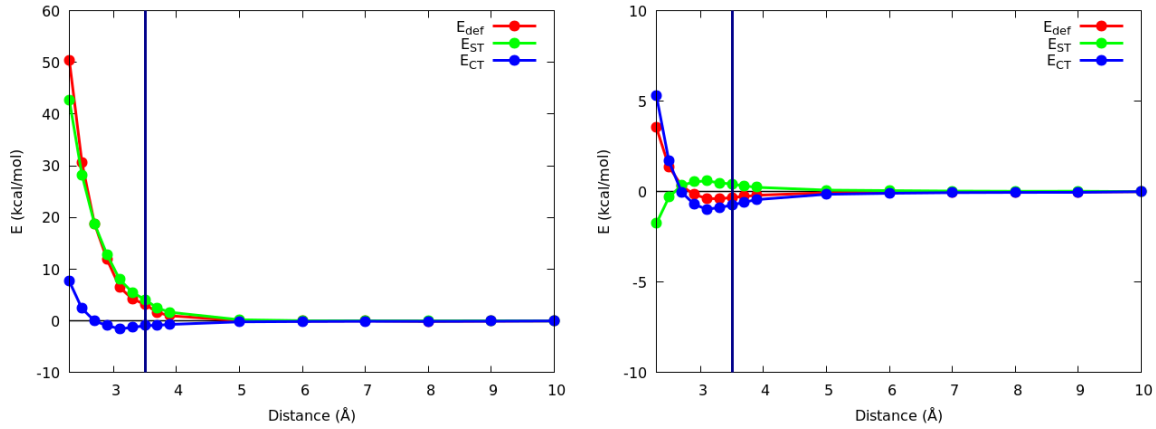

Figure 43: Deformation energy E_{def}, charge transfer term E_{CT} and steric energy E_{ST} at the DFT and HF levels of theory for the N atom (left) and H atom (right) in the H-H eclipsed NH_3 dimer.

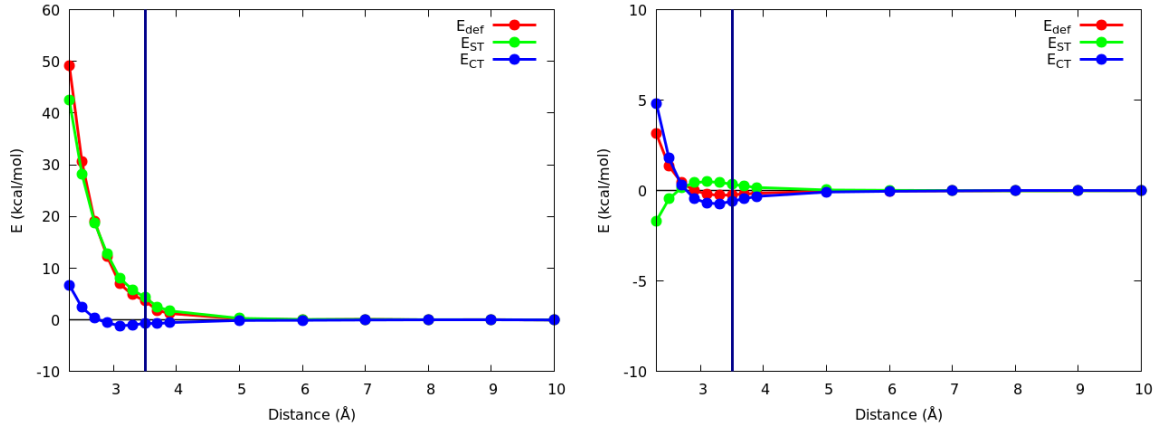

Figure 44: Deformation energy E_{def}, charge transfer term E_{CT} and steric energy E_{ST} at the DFT and HF levels of theory for the N atom (left) and H atom (right) in the H-H staggered NH_3 dimer.

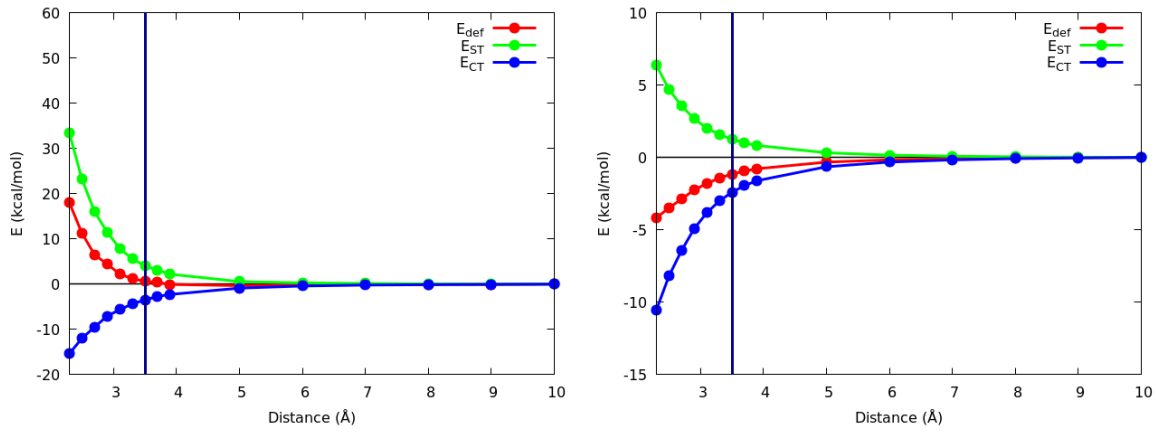

Figure 45: Deformation energy E_{def}, charge transfer term E_{CT} and steric energy E_{ST} at the DFT and HF levels of theory for the N atom (left) and H atom (right) in the N-N eclipsed NH_3 dimer.

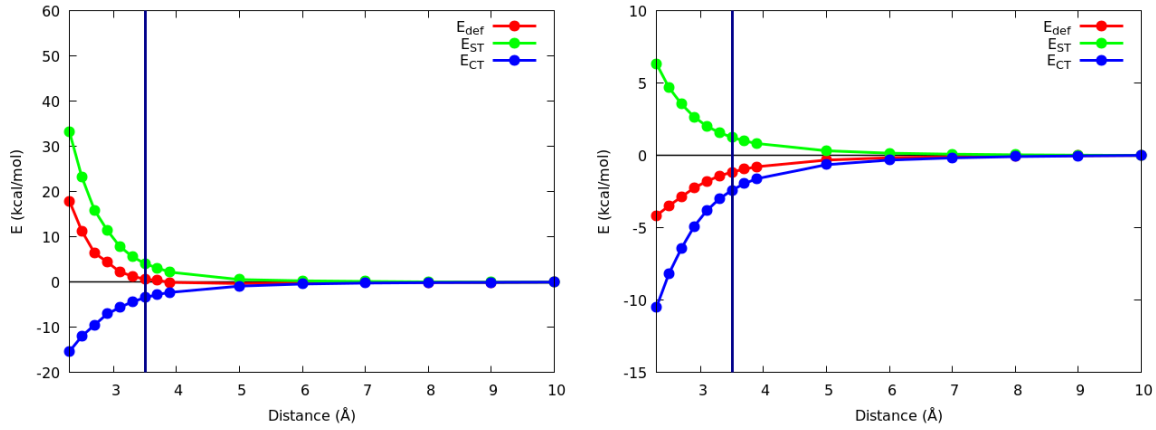

Figure 46: Deformation energy E_{def}, charge transfer term E_{CT} and steric energy E_{ST} at the DFT and HF levels of theory for the N atom (left) and H atom (right) in the N-N staggered NH_3 dimer.

4.2.3 Total deformation energy of the ammonia monomer

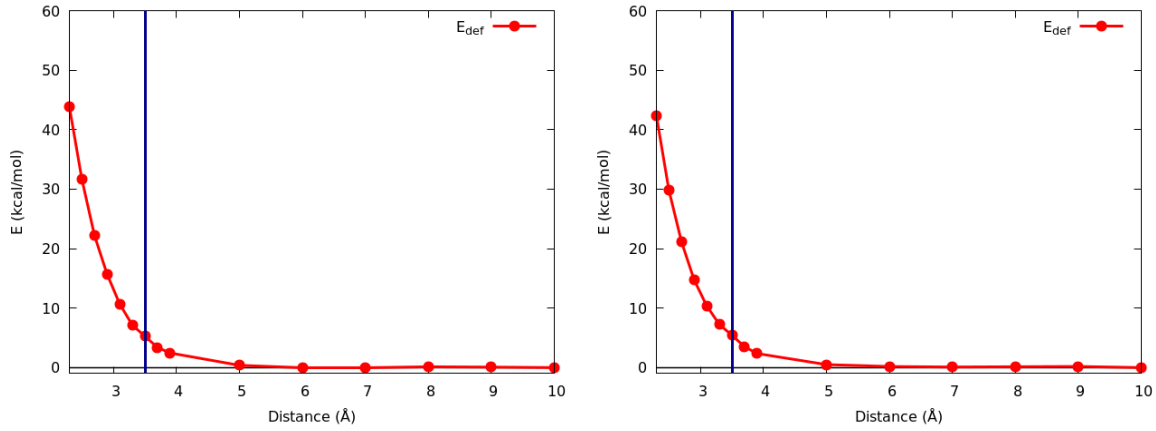

Figure 47: Total deformation energy E_{def} at the DFT and HF levels of theory for the NH_3 molecule in the H-H eclipsed (left) and H-H staggered (right) approaches.

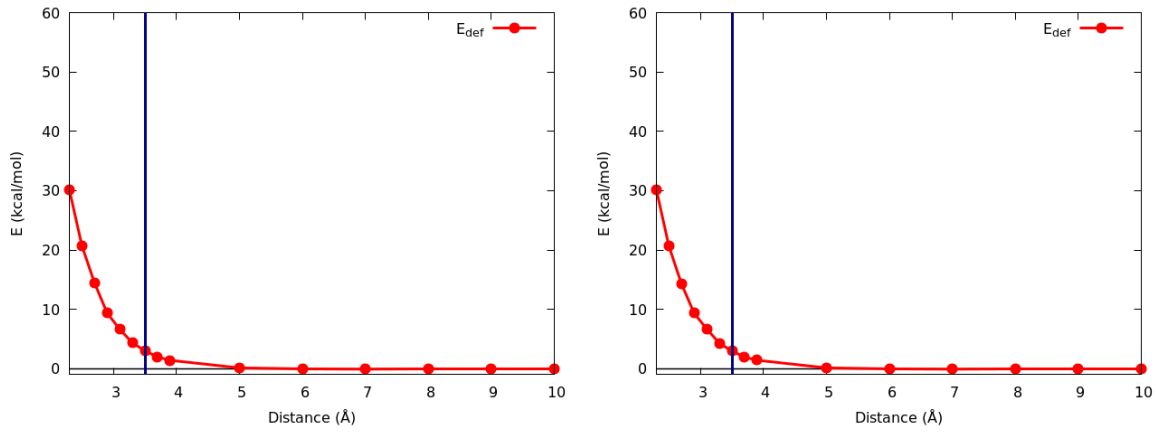

Figure 48: Total deformation energy E_{def} at the DFT and HF levels of theory for the NH_3 molecule in the N-N eclipsed (left) and N-N staggered (right) approaches.

4.2.4 Change in the atomic charges, ΔQ

The following figures and tables show the evolution of the atomic charges of the constituting atoms of the ammonia monomer along the relaxed scan.

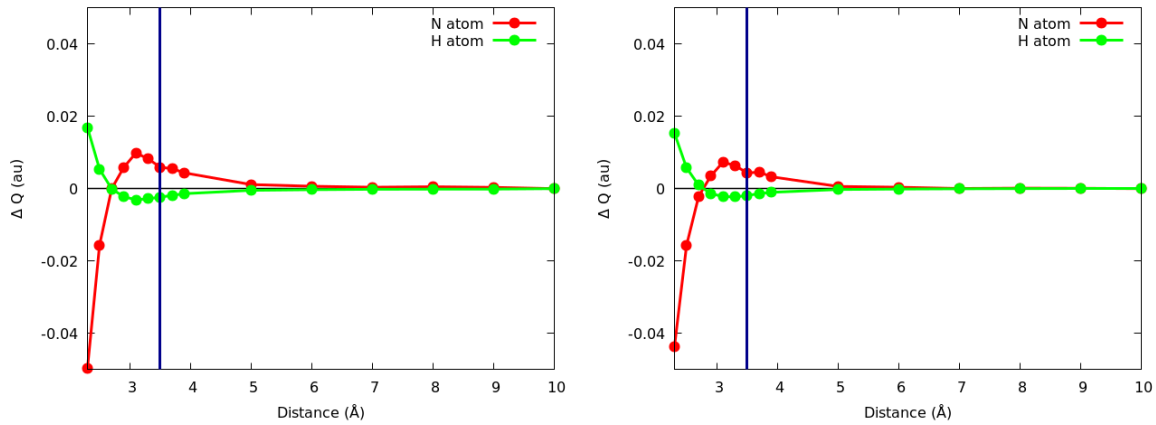

Figure 49: Change in the atomic charge at the DFT level of theory for the H-H eclipsed (left) and H-H staggered (right) relaxed approximations.

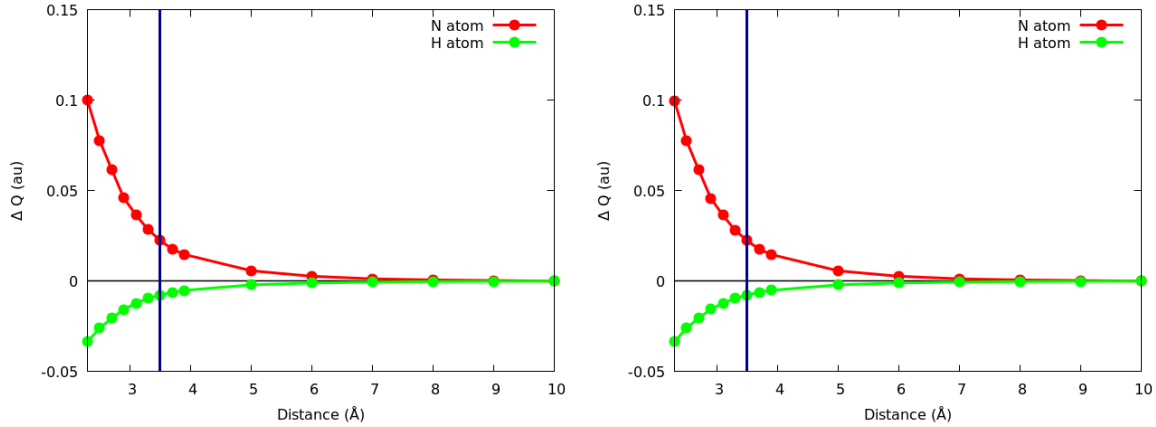

Figure 50: Change in the atomic charge at the DFT levels of theory for the N-N eclipsed (right) and N-N staggered (left) relaxed approximations.

4.2.5 Geometrical changes

The current section collects the evolution of the most relevant geometrical features of the ammonia dimer along the relaxed scan.

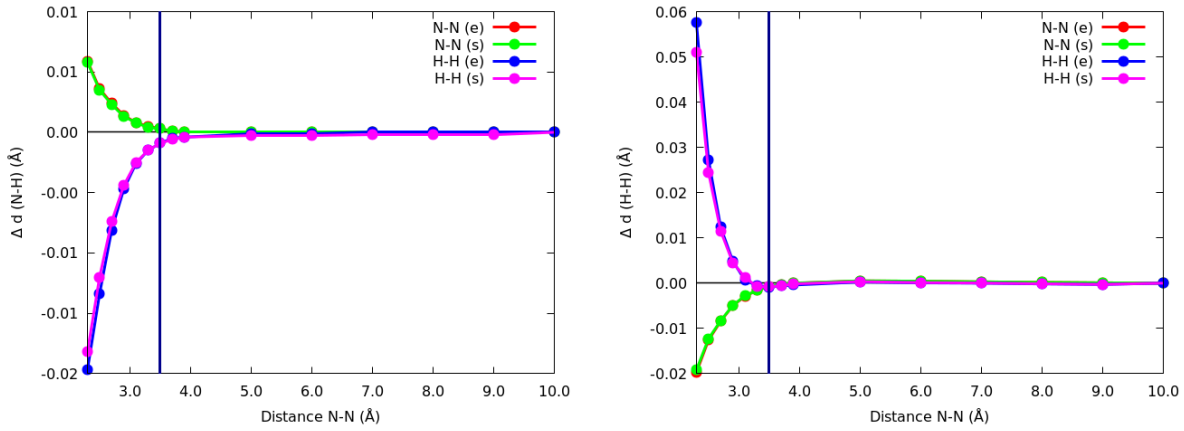

Figure 51: Evolution of the N-H (left) and H-H (right) intra-molecular distances along the relaxed scan.

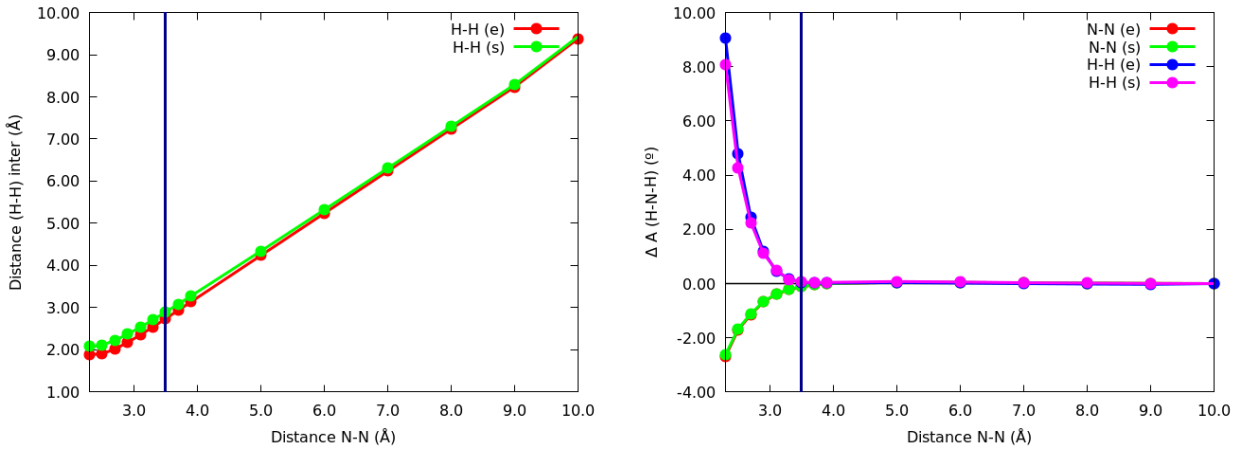

Figure 52: Evolution of the H-H inter-molecular distances (left) and H-N-H intra-molecular angle (right) along the relaxed scan. The inter-molecular distance is reported as the separation between the closest H neighbors in the two different monomers.

5 Self-substitution reactions of halomethanes (CH_3X)

We report the results obtained in the self-substitution reactions (S_N2) of a halomethane (CH_3X) and the corresponding halide anion (X^-). All calculations were performed in the gas phase at different levels of theory (DFT and HF) in combination with the correlation consistent aug-cc-pVDZ basis set. The graphs and representations are reported as relative values with respect to the reactive complex structure. The TS is located at $\xi = 0$. As the nucleophile and the leaving group are the same species, only the forward counterpart profile is shown

5.1 Benchmarking table

Methodology	Basis set	H_{reac} (au)	H_{TS} (au)	$\Delta E^{\ddagger}$ (kcal/mol)	Error (kcal/mol)
B2PLYP	cc-pVDZ	-239.320347	-239.306543	8.66	-4.74
B2PLYP	cc-pvtz	-239.488149	-239.473900	8.94	-4.46
B2PLYP	aug-cc-pVDZ	-239.421234	-239.407282	8.76	-4.64
B2PLYP	6-31G	-239.206956	-239.198788	5.13	-8.27
B2PLYP	6-311G	-239.324397	-239.316473	4.97	-8.43
B2PLYP	6-311G(d)	-239.400452	-239.386092	9.01	-4.39
B2PLYP	6-311++G(d)	-239.456622	-239.440849	9.90	-3.50
B3LYP	cc-pVDZ	-239.520193	-239.508073	7.61	-5.79
B3LYP	cc-pvtz	-239.643100	-239.630495	7.91	-5.49
B3LYP	aug-cc-pVDZ	-239.608109	-239.594937	8.27	-5.13
B3LYP	6-31G	-239.468273	-239.461094	4.50	-8.90
B3LYP	6-311G	-239.580855	-239.574144	4.21	-9.19
B3LYP	6-311G(d)	-239.599867	-239.587878	7.52	-5.88
B3LYP	6-311++G(d)	-239.653369	-239.640023	8.37	-5.03
HF	cc-pVDZ	-238.399355	-238.374193	15.79	2.39
HF	cc-pvtz	-238.498939	-238.470335	17.95	4.55
HF	aug-cc-pVDZ	-238.457975	-238.430781	17.06	3.66
HF	6-31G	-238.336129	-238.318722	10.92	-2.48
HF	6-311G	-238.428256	-238.410783	10.96	-2.44
HF	6-311G(d)	-238.459404	-238.432756	16.72	3.32
HF	6-311++G(d)	-238.496102	-238.466853	18.35	4.95
M062X	cc-pVDZ	-239.426905	-239.409288	11.05	-2.35
M062X	cc-pvtz	-239.548089	-239.528480	12.30	-1.10
M062X	aug-cc-pVDZ	-239.500741	-239.479726	13.19	-0.21
M062X	6-31G	-239.369150	-239.356136	8.17	-5.23
M062X	6-311G	-239.480692	-239.467223	8.45	-4.95
M062X	6-311G(d)	-239.502137	-239.483509	11.69	-1.71
M062X	6-311++G(d)	-239.546110	-239.523883	13.95	0.55
PBE1PBE	cc-pVDZ	-239.276773	-239.263638	8.24	-5.16
PBE1PBE	cc-pvtz	-239.387574	-239.372805	9.27	-4.13
PBE1PBE	aug-cc-pVDZ	-239.355162	-239.340115	9.44	-3.96
PBE1PBE	6-31G	-239.222498	-239.214485	5.03	-8.37
PBE1PBE	6-311G	-239.325888	-239.317850	5.04	-8.36
PBE1PBE	6-311G(d)	-239.346376	-239.332741	8.56	-4.84
PBE1PBE	6-311++G(d)	-239.395180	-239.379434	9.88	-3.52
PBEPBE	cc-pVDZ	-239.266712	-239.257574	5.73	-7.67
PBEPBE	cc-pvtz	-239.386482	-239.377862	5.41	-7.99
PBEPBE	aug-cc-pVDZ	-239.357591	-239.349012	5.38	-8.02
PBEPBE	6-31G	-239.215921	-239.210822	3.20	-10.20
PBEPBE	6-311G	-239.327732	-239.323295	2.78	-10.62
PBEPBE	6-311G(d)	-239.343739	-239.335211	5.35	-8.05
PBEPBE	6-311++G(d)	-239.399939	-239.391246	5.45	-7.95

Table 3: Benchmarking table collecting the activation energies for the reaction with CH_3 in terms of the standard enthalpies computed at the 298.15 K. Errors are reported with respect to the experimentally determined values[4].

With the aim to select the optimum level of theory to be used for the computation of the self-substitution reactions under study, the activation energy of the reaction of our model system (CH_3F and F^-) was evaluated with different methodologies as collected in Table 3. As shown, the lowest errors in the evaluation of the activation energy of the model reaction were obtained for the M06-2X/aug-cc-pVDZ level of theory and hence this will be consider the methodology of choice to be used in our studies. It is interesting to notice that the errors at the HF level of theory are moderate, showing an offset with respect to the experimentally reported values of only a few kcal/mol.

5.2 Effect of the methodology in the SN2 calculations

After having selected the best functional and basis set to be used in the evaluation of the self-substitution reactions of simple haloalkanes, a test-bed study of the role of the theoretical level in the IQA analysis of the intra-atomic components of the energy along the reaction was performed. For such a purpose, a set of IQA calculations were run along the forward part of the S_N2 reaction of the model system ($CH_3F + F^-$). Since the results obtained with the methane dimer suggested that any of the methodologies, and particularly CASSCF and HF, offer nearly identical results, the benchmarking study was performed at the HF and DFT methods in combination with the aug-cc-pVDZ basis set. Furthermore, regarding the density functional choice, both the Minnesota (M06-2X) and the hybrid (B3LYP) functionals were tested, since the are commonly used when dealing with common main-element compounds.

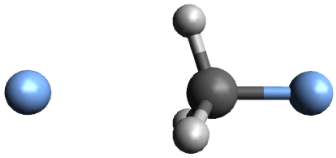

Figure 53: The halomethane plus halide substitution reaction.

5.2.1 Calculations at the B3LYP/aug-cc-pVDZ level of theory

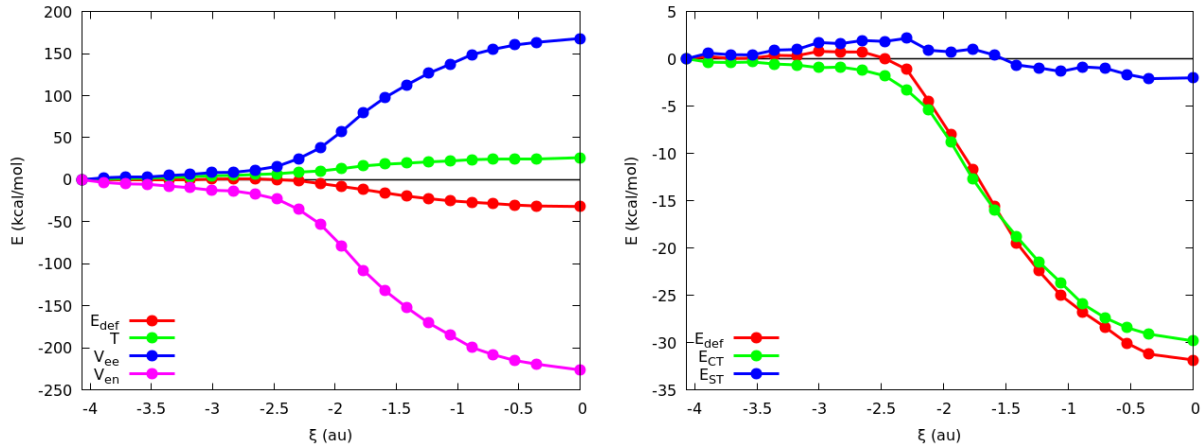

Figure 54: Deformation energy, E_{def}, kinetic energy, T, electron-electron repulsion, V_{ee}, and electron-nucleus attraction, V_{en}, of the C atom along the forward part of the reaction path.

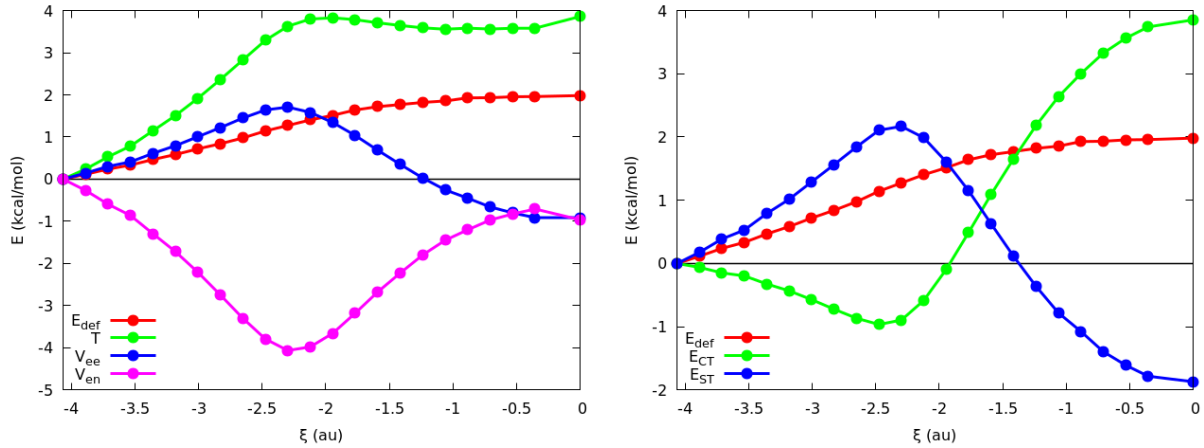

Figure 55: Deformation energy, E_{def}, kinetic energy, T, electron-electron repulsion, V_{ee}, and electron-nucleus attraction, V_{en}, of the H atom along the forward part of the reaction path.

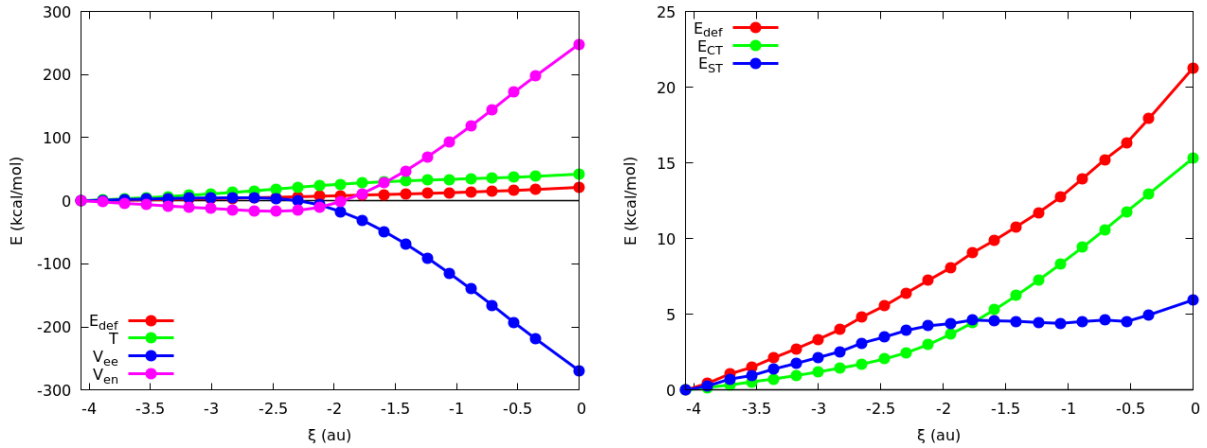

Figure 56: Deformation energy, E_{def}, kinetic energy, T, electron-electron repulsion, V_{ee}, and electron-nucleus attraction, V_{en}, of the nucleophile along the forward part of the reaction path.

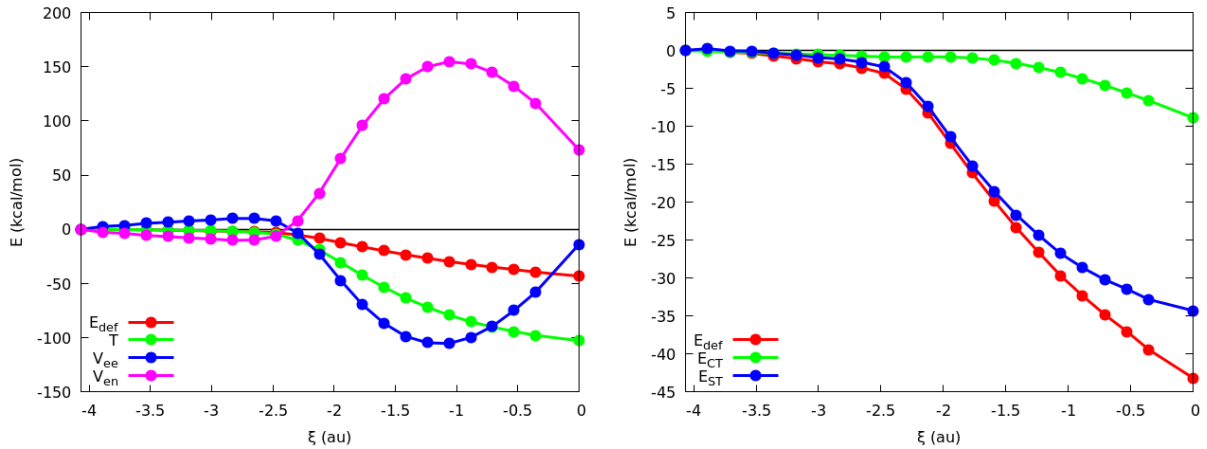

Figure 57: Deformation energy, E_{def}, kinetic energy, T, electron-electron repulsion, V_{ee}, and electron-nucleus attraction, V_{en}, of the leaving group along the forward part of the reaction path.

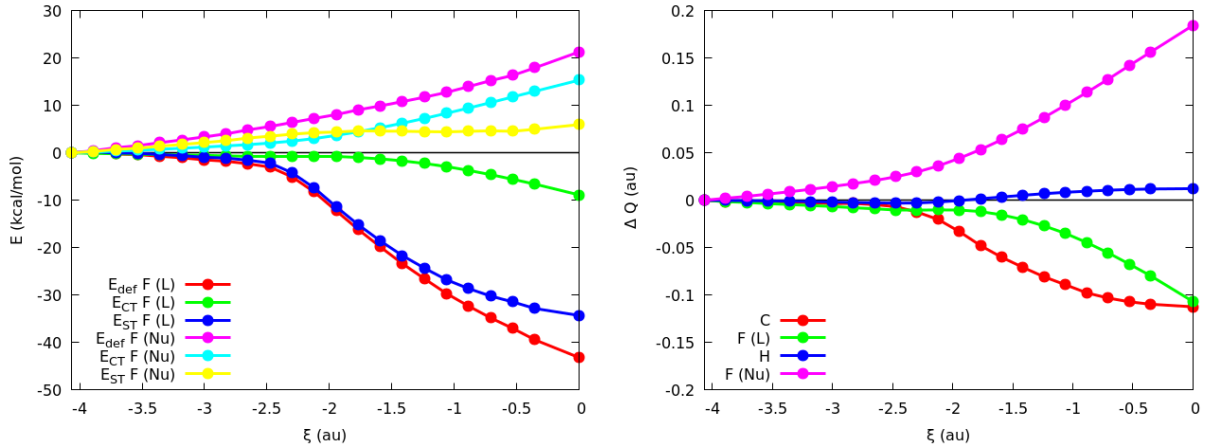

Figure 58: Energetic components for the nucleophile and leaving group participating in the reaction and change in the atomic charges, ΔQ, along the forward part of the reaction path.

5.2.2 Calculations at the M06-2X/aug-cc-pVDZ level of theory

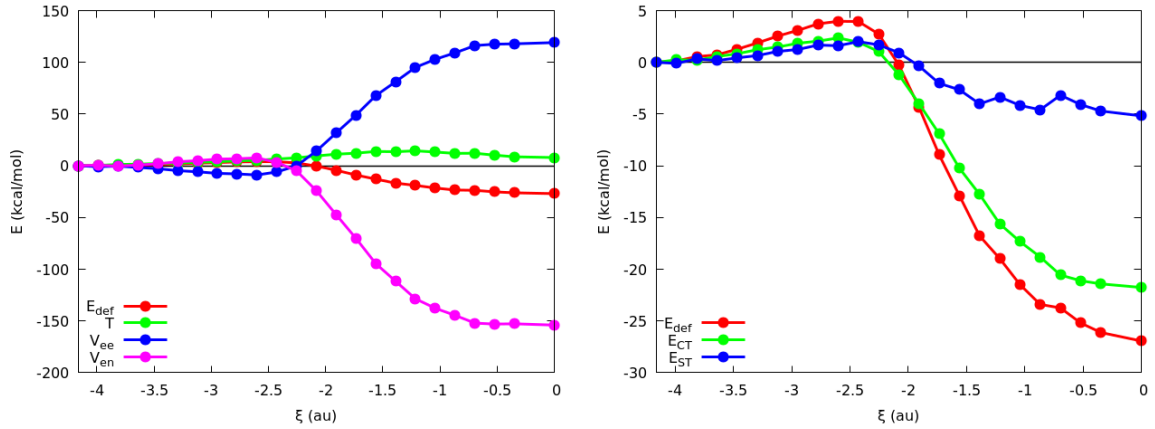

Figure 59: Deformation energy, E_{def}, kinetic energy, T, electron-electron repulsion, V_{ee}, and electron-nucleus attraction, V_{en}, of the C atom along the forward part of the reaction path.

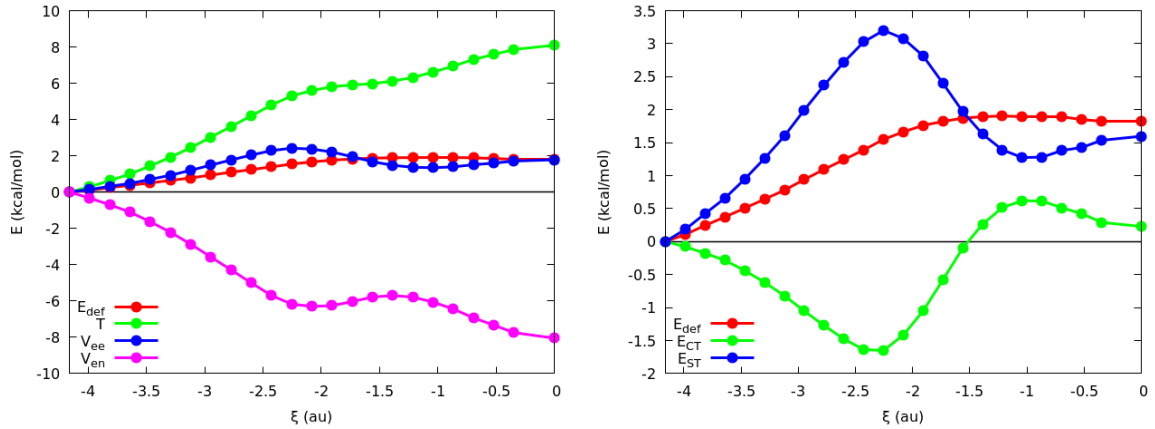

Figure 60: Deformation energy, E_{def}, kinetic energy, T, electron-electron repulsion, V_{ee}, and electron-nucleus attraction, V_{en}, of the H atom along the forward part of the reaction path.

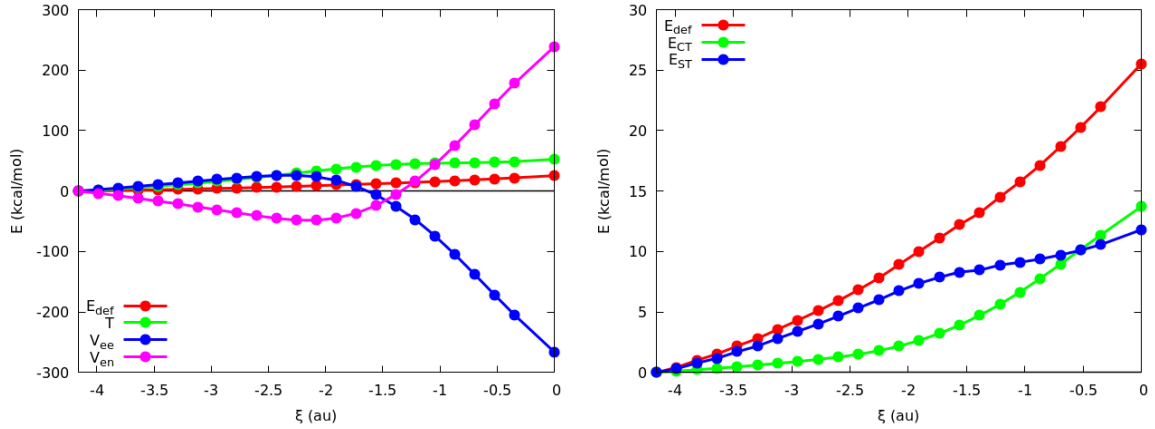

Figure 61: Deformation energy, E_{def}, kinetic energy, T, electron-electron repulsion, V_{ee}, and electron-nucleus attraction, V_{en}, of the nucleophile along the forward part of the reaction path.

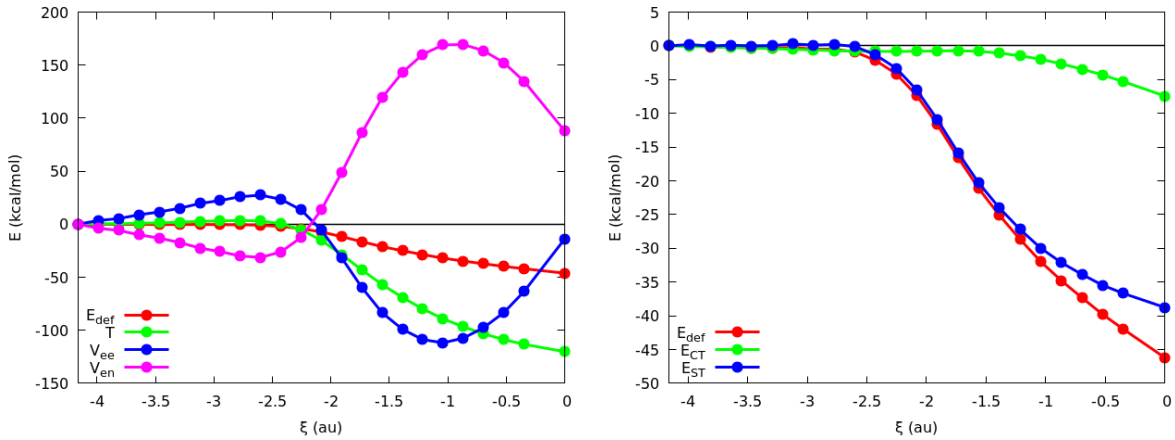

Figure 62: Deformation energy, E_{def}, kinetic energy, T, electron-electron repulsion, V_{ee}, and electron-nucleus attraction, V_{en}, of the leaving group along the forward part of the reaction path.

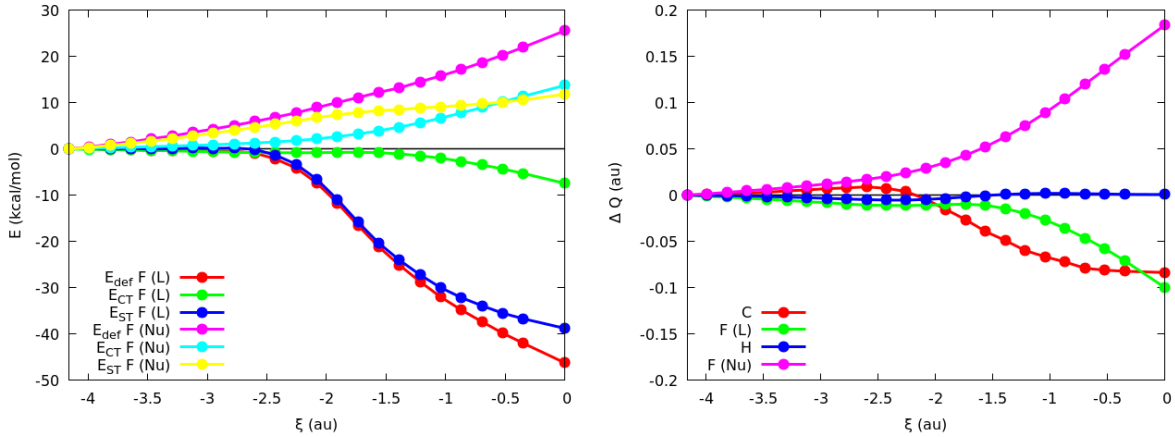

Figure 63: Energetic components for the nucleophile and leaving group participating in the reaction and change in the atomic charges, ΔQ, along the forward part of the reaction path.

5.2.3 Calculations at the HF/aug-cc-pVDZ level of theory

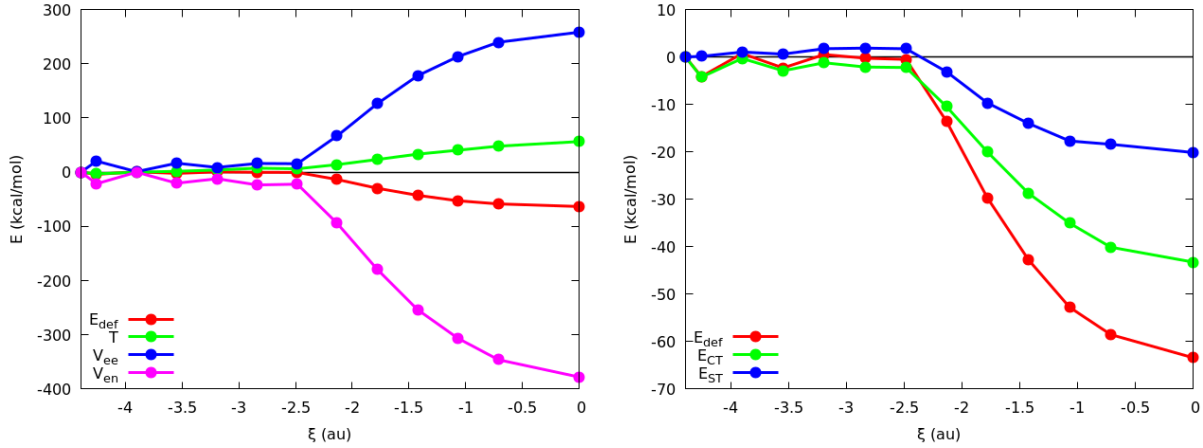

Figure 64: Deformation energy, E_{def}, kinetic energy, T, electron-electron repulsion, V_{ee}, and electron-nucleus attraction, V_{en}, of the C atom along the forward part of the reaction path.

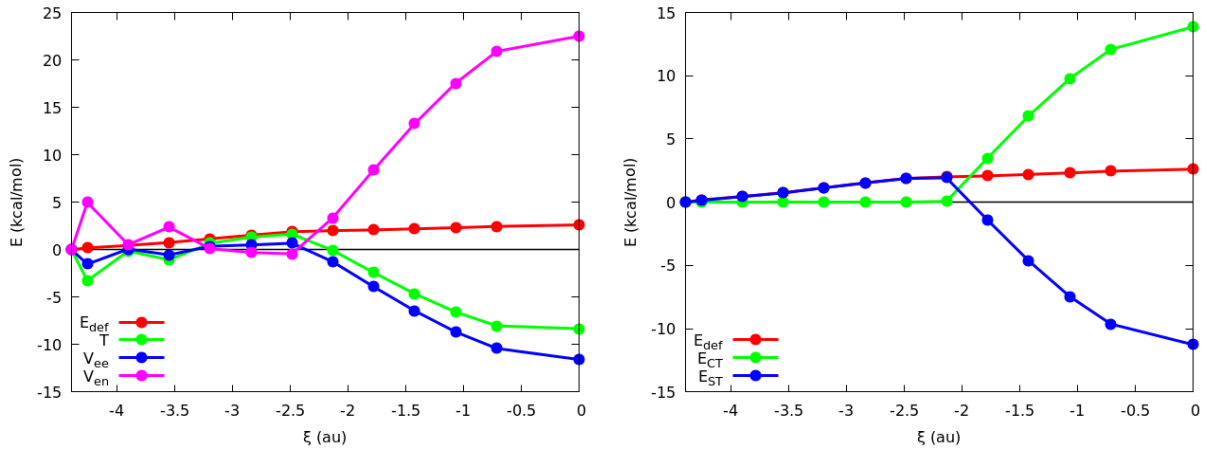

Figure 65: Deformation energy, E_{def}, kinetic energy, T, electron-electron repulsion, V_{ee}, and electron-nucleus attraction, V_{en}, of the H atom along the forward part of the reaction path.

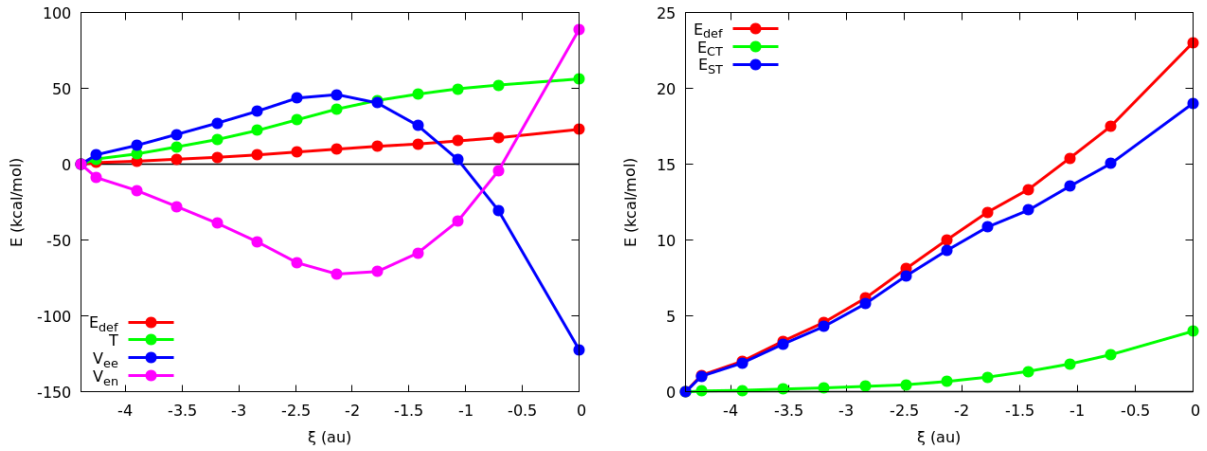

Figure 66: Deformation energy, E_{def}, kinetic energy, T, electron-electron repulsion, V_{ee}, and electron-nucleus attraction, V_{en}, of the nucleophile along the forward part of the reaction path.

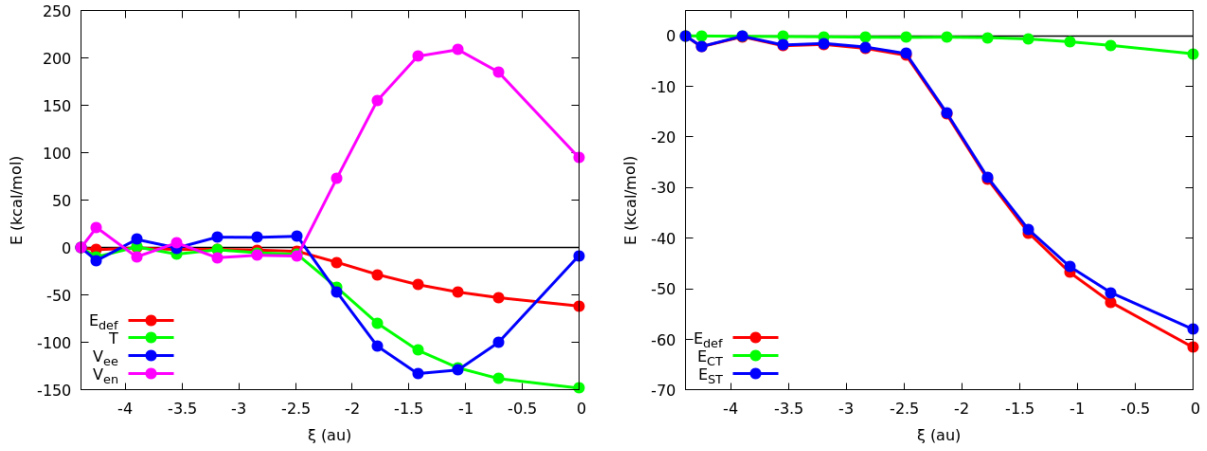

Figure 67: Deformation energy, E_{def}, kinetic energy, T, electron-electron repulsion, V_{ee}, and electron-nucleus attraction, V_{en}, of the leaving group along the forward part of the reaction path.

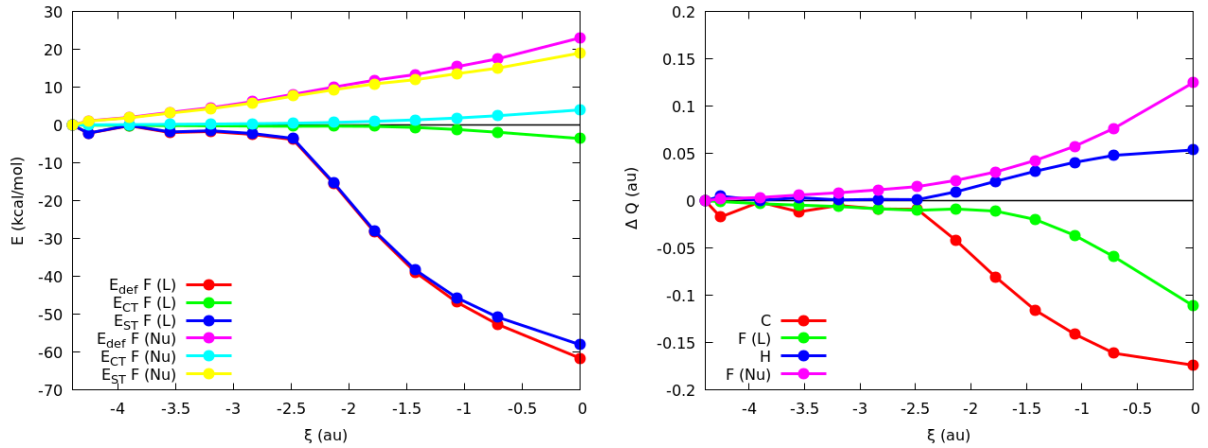

Figure 68: Energetic components for the nucleophile and leaving group participating in the reaction (left) and change in the atomic charges, ΔQ, (right) along the forward part of the reaction path.

The results obtained for any of the DFT functionals employed are quite similar to one another on a general basis, showing nearly identical trends for the different contributions to the total deformation energy of the involved atoms. It is worth to mention, however, that the steric, E_{ST}, and charge transfer, E_{CT}, contributions for the C atom as well as for the H atoms of the methyl group exhibit slightly different trends for these two functionals. More specifically, the E_{ST} term of the central C atom remains barely constant along the reaction when computed at the B3LYP level of theory whereas in the case of the Minnesota functional there is a small decrease of such contribution to the total deformation, E_{def}, along the reaction. Furthermore, calculations at the HF level of theory yielded qualitatively similar results to the previously obtained ones for all the atoms expect for the H atoms of the CH_3 moiety, for which drastically different trends were obtained. Such a deviation can be mainly attributed to the large discrepancies observed in the atomic charges computed at the DFT and HF levels of theory, which becomes even more evident for the H atoms. The following figures collect the deformation, E_{def}, and steric, E_{ST}, energies along with the evolution of the ΔQ for the different atoms involved in the reaction under study. For the sake of simplicity, the x axis of the upcoming figures is defined as the ratio of a given step along the reaction coordinate and its maximum value.

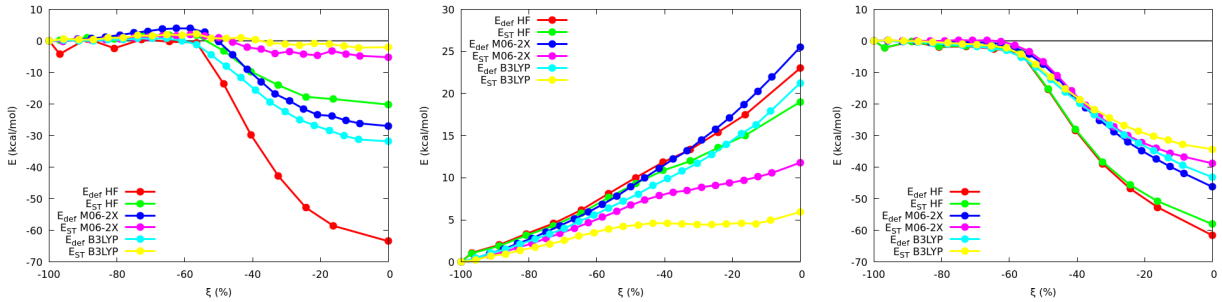

Figure 69: Energetic components of the central C atom (left), nucleophile (center) and leaving group (right) along the forward part of the reaction path computed at different levels of theory.

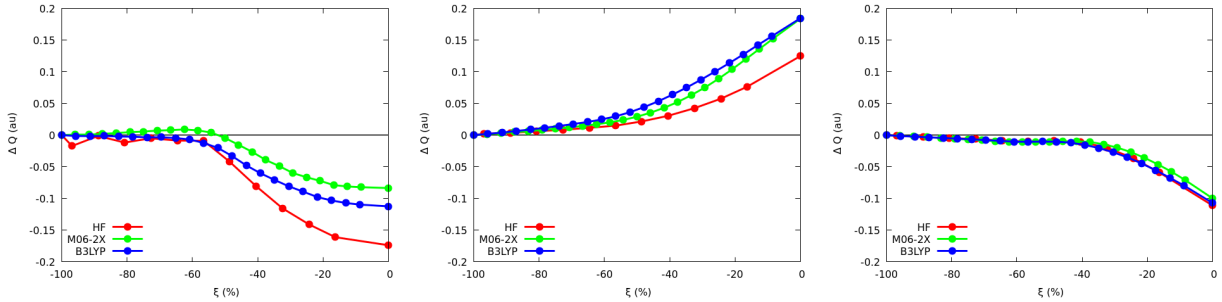

Figure 70: ΔQ of the central C atom (left), nucleophile (center) and leaving group (right) along the forward part of the reaction path computed at different levels of theory.

As shown in the previous figures, the qualitative behaviors exhibited by the deformation and steric energies of the main atoms participating in the substitution reactions are equivalent for any of the methodologies under consideration. However, HF results in considerably larger total deformation and steric contributions when compared to any of the DFT functionals employed, which furthermore yielded quite close results to one another regardless on the functional employed. Moreover, HF generally overestimate the total contribution of the steric energy to the total deformation when compared with the results obtained at the DFT levels of theory.

Level of theory	Q(C) (au)	Q(H) (au)	$Q(\mathrm{F})_{Nu}$ (au)	$Q(\mathrm{F})_{L}$ (au)
HF/aug-cc-pVDZ	0.75	-0.01	-0.98	-0.74
B3LYP/aug-cc-pVDZ	0.49	0.04	-0.95	-0.65
M06-2X/aug-cc-pVDZ	0.55	0.03	-0.96	-0.68

Table 4: Atomic charges of the atoms involved in the model reaction computed at different levels of theory. The values correspond to the atomic charges of the reactive complex species.

As in previous case, any of the methodologies employed yielded analogous trends in the total change of the atomic charges of the main atoms participating in the reaction under study. It is worth to mention, however, that the total change in the atomic charges is considerably different when computed at the HF level of theory, a result which is specially pronounced for the C and nucleophilic F atoms. Whereas on the other hand, the trends in the ΔQ of the leaving group are barely affected by the methodology employed in the calculation.

5.3 Effect of the halogen in the S_N2 reaction

Now we turn to the effect of the halogen in the self-substitution reactions. All calculations were performed at the M06-2X/aug-cc-pVDZ level of theory using Gaussian09[5] without accounting for any relativistic effect.

5.3.1 X=Cl

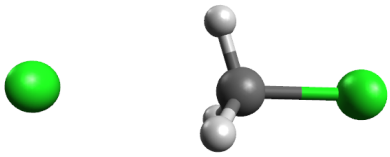

Figure 71: Reaction between CH_3Cl and Cl^-.

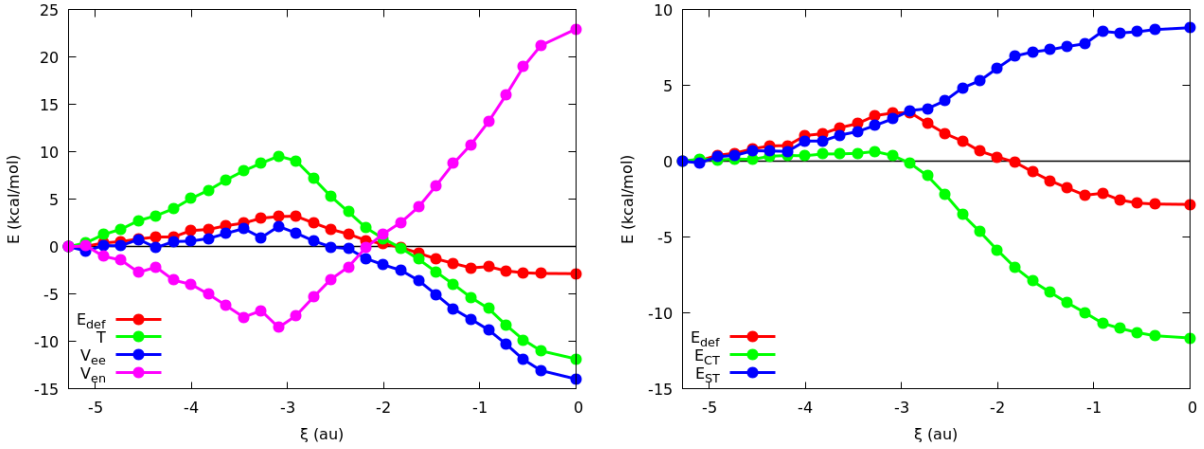

Figure 72: Deformation energy, E_{def}, kinetic energy, T, electron-electron repulsion, V_{ee}, and electron-nucleus attraction, V_{en}, of the C atom along the forward part of the reaction path.

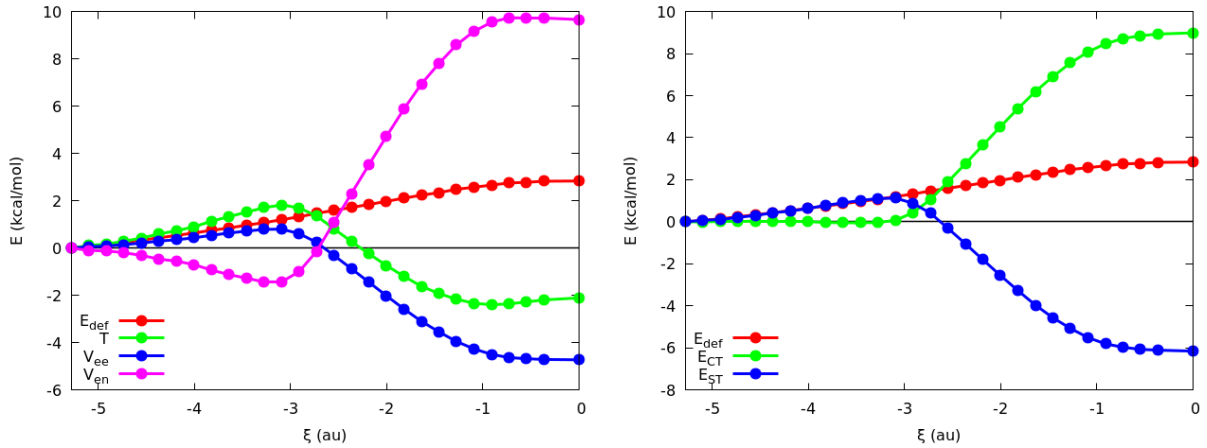

Figure 73: Deformation energy, E_{def}, kinetic energy, T, electron-electron repulsion, V_{ee}, and electron-nucleus attraction, V_{en}, of the H atom along the forward part of the reaction path.

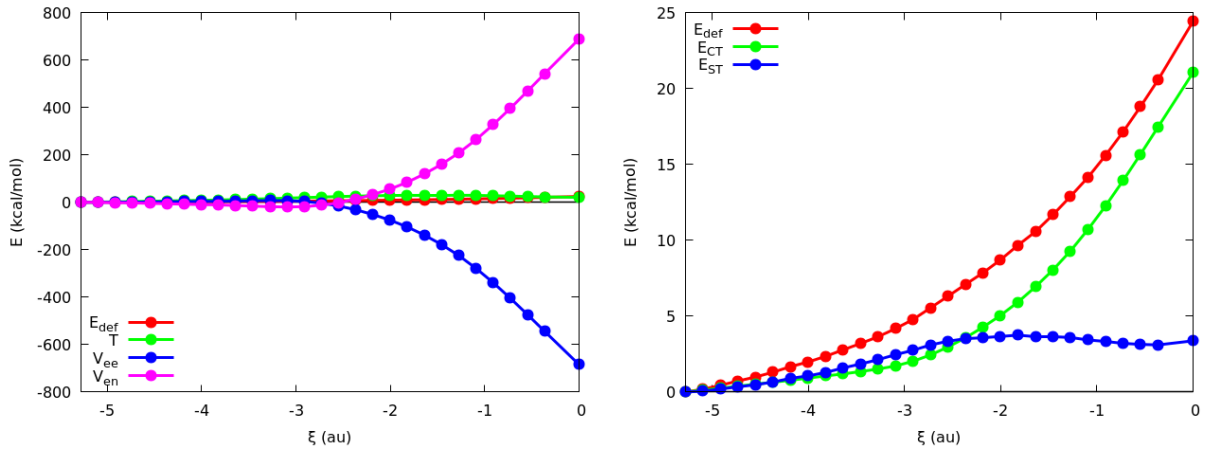

Figure 74: Deformation energy, E_{def}, kinetic energy, T, electron-electron repulsion, V_{ee}, and electron-nucleus attraction, V_{en}, of the nucleophile along the forward part of the reaction path.

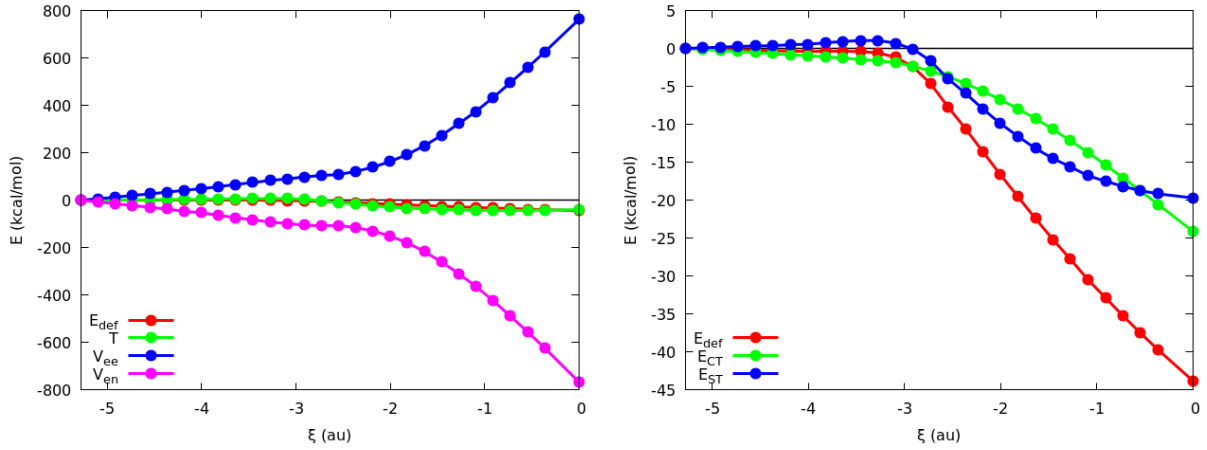

Figure 75: Deformation energy, E_{def}, kinetic energy, T, electron-electron repulsion, V_{ee}, and electron-nucleus attraction, V_{en}, of the leaving group along the forward part of the reaction path.

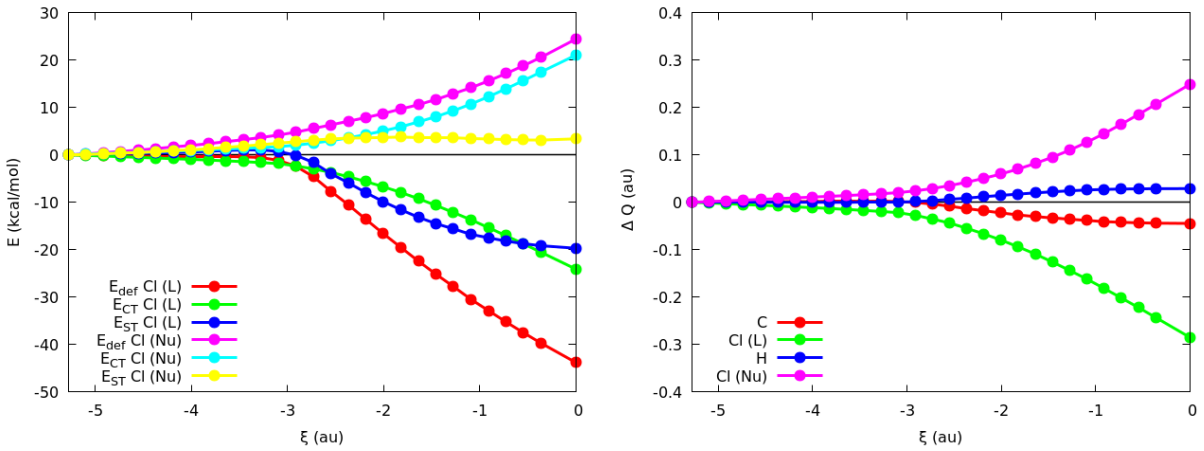

Figure 76: Energetic components for the nucleophile and leaving group participating in the reaction (left) and change in the atomic charges, ΔQ, (right) along the forward part of the reaction path.

5.3.2 X=Br

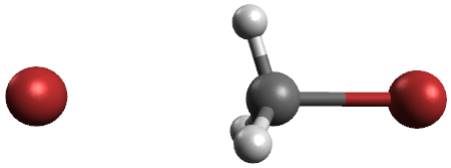

Figure 77: Reaction between CH_3Br and Br^-.

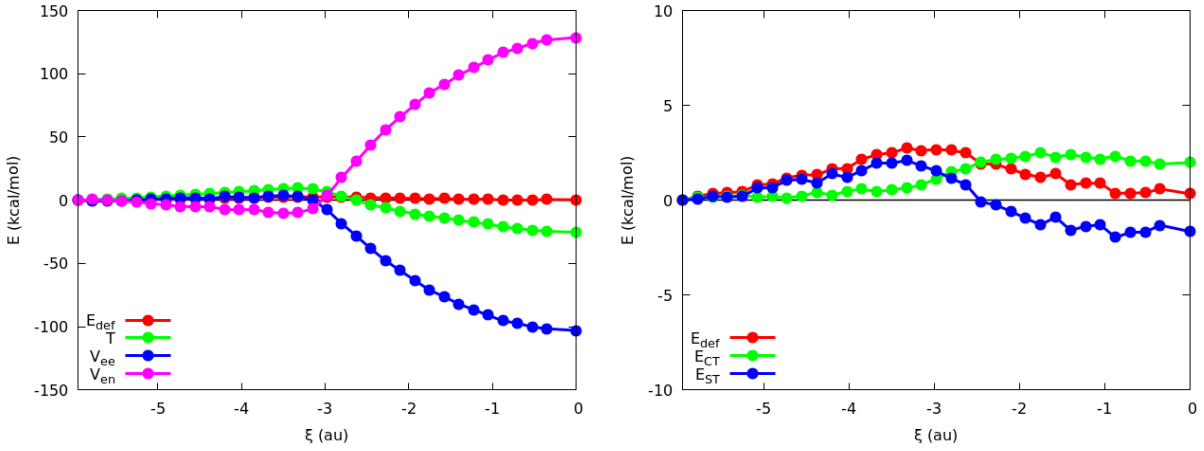

Figure 78: Deformation energy, E_{def}, kinetic energy, T, electron-electron repulsion, V_{ee}, and electron-nucleus attraction, V_{en}, of the C atom along the forward part of the reaction path.

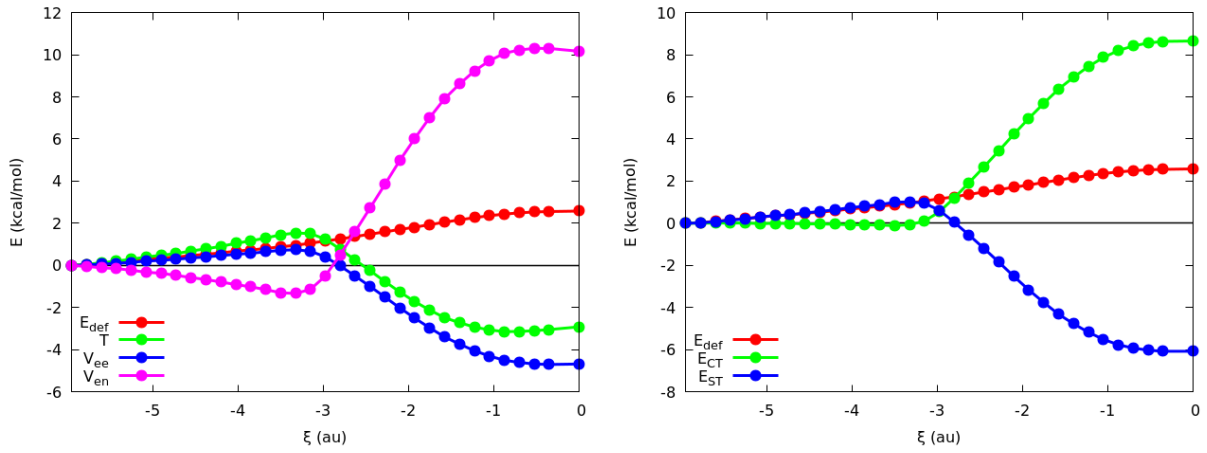

Figure 79: Deformation energy, E_{def}, kinetic energy, T, electron-electron repulsion, V_{ee}, and electron-nucleus attraction, V_{en}, of the H atom along the forward part of the reaction path.

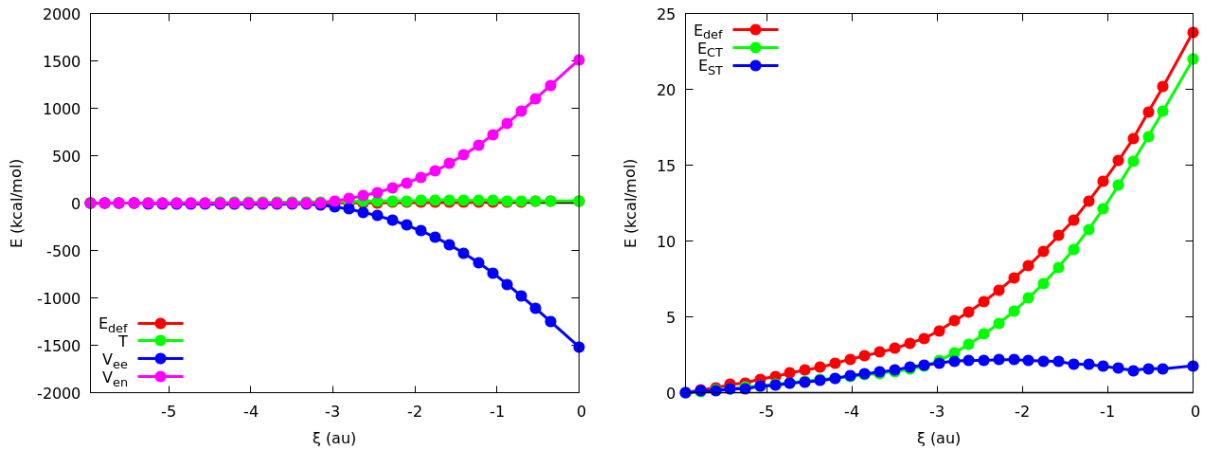

Figure 80: Deformation energy, E_{def}, kinetic energy, T, electron-electron repulsion, V_{ee}, and electron-nucleus attraction, V_{en}, of the nucleophile along the forward part of the reaction path.

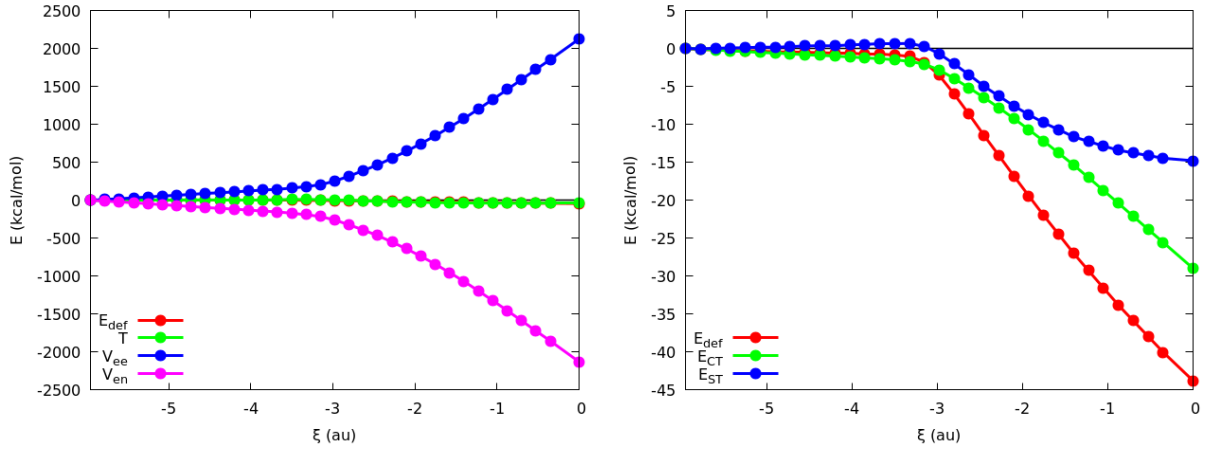

Figure 81: Deformation energy, E_{def}, kinetic energy, T, electron-electron repulsion, V_{ee}, and electron-nucleus attraction, V_{en}, of the leaving group along the forward part of the reaction path.

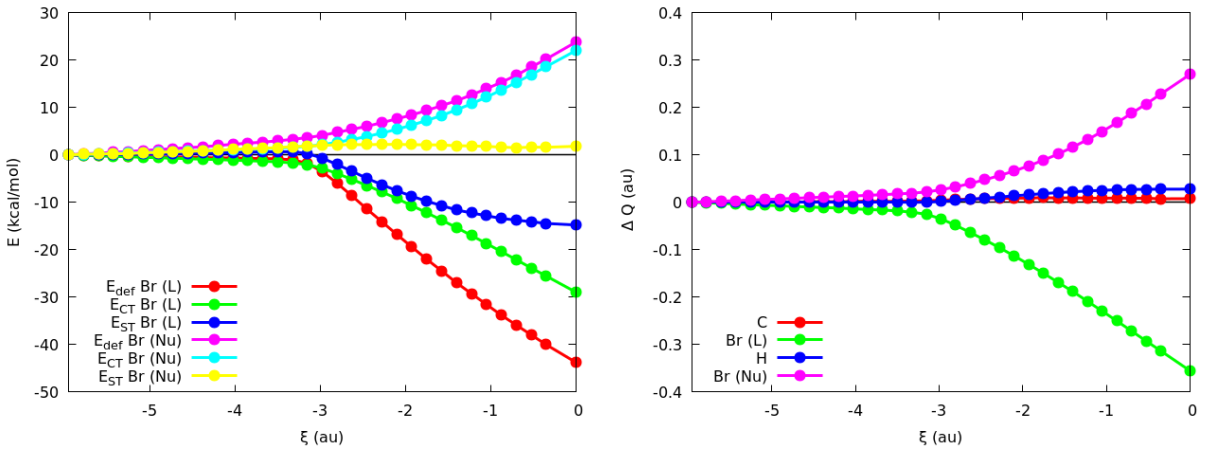

Figure 82: Energetic components for the nucleophile and leaving group participating in the reaction (left) and change in the atomic charges, ΔQ, (right) along the forward part of the reaction path.

5.3.3 Comparison

The following figures show the change in the net atomic charges (ΔQ) of the different atoms involved in the self-substitution reactions. It has been computed using the original reactive complex as reference system.

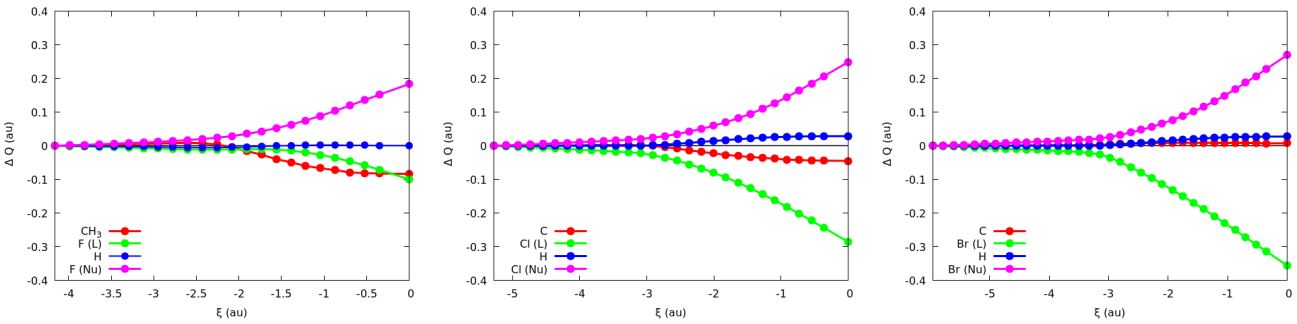

Figure 83: Change in the atomic charges along the self-substitution reactions with different halogens (F (left), Cl (center), Br (right)).

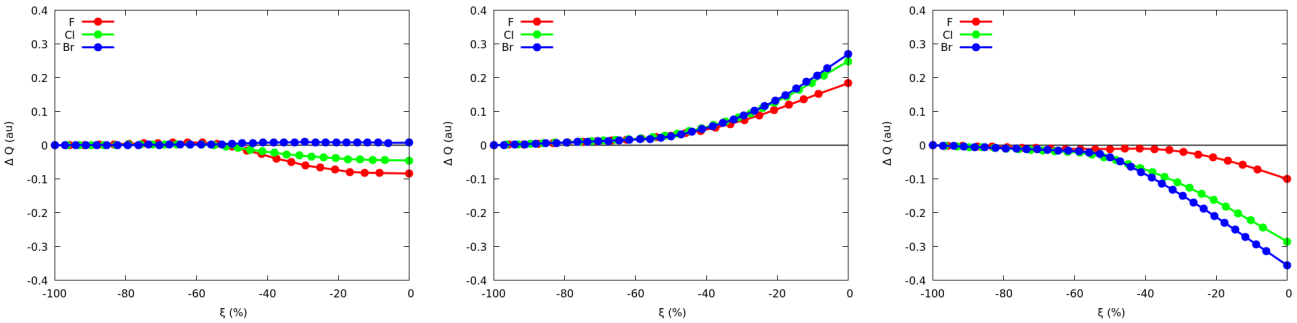

Figure 84: Change in the atomic charges for the main atoms involved in the reaction (C (left), nucleophile (center) and leaving group (right)) along the self-substitution reactions with different halogens (X = F (violet), Cl (green), Br (blue)).

Halogen (X)	Q(C)(au)	Q(H)(au)	Q(Nu) (au)	Q(L) (au)
F	0.55	0.03	-0.96	-0.68
Cl	0.19	0.06	-0.95	-0.41
Br	0.05	0.07	-0.94	-0.31

Table 5: Atomic charges of the different atoms involved in the self-substitution reactions under study. The values correspond to the reactive complex structure. Nu refers to the nucleophile and L to the leaving group for a given system.

As it can be seen from the previous graphs, the total change in the charge of the central carbon atom along the reaction generally decreases through the halogen series, leading to almost negligible changes in the C atom when X=Br. Similarly, the change in the atomic charge of the H atoms is nearly constant and relatively small along the whole processes. ΔQ(X) is, on the other hand, significant, increasing as the series F-Cl-Br proceeds. More specifically, the charge of the nucleophile and leaving groups remain nearly constant during the preparation stage of the reaction. From this point on, the nucleophile progressively reduces its charge, leading to a positive value of ΔQ along this second stage of the reaction. Though such a trend if very similar for any system, the value of ΔQ increases slightly along the halogen series. The opposite behavior can be observed for the leaving group, which experiences a significant increase in its atomic charge along the second stage of the process, resulting in negative ΔQ's.

The following figures show the evolution of the different energetic components of the various deformation energies on changing the halogen X = F, Cl and Br, represented in violet, green and blue colors, respectively.

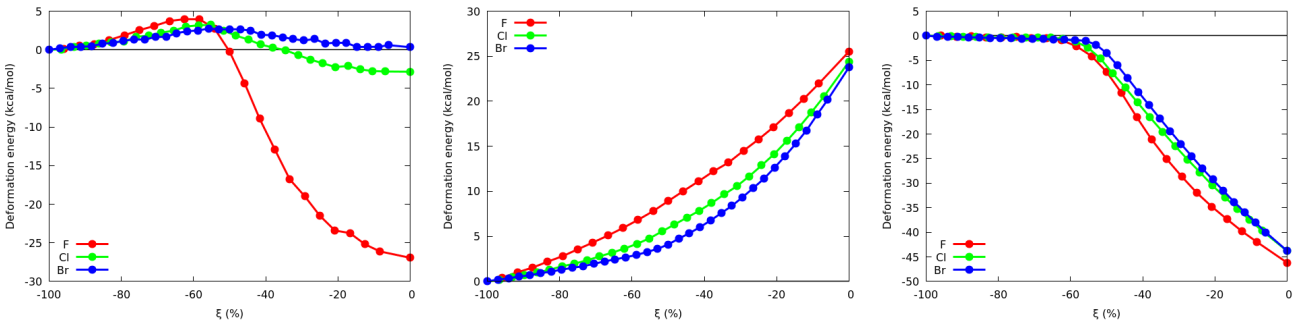

Figure 85: Deformation energies of the C (left), nucleophile (center) and leaving group (right) along the self-substitution reactions with different halogens.

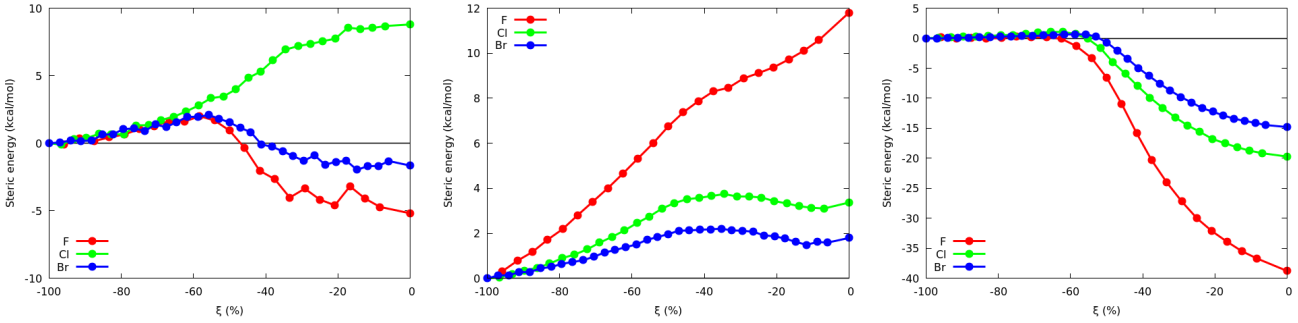

Figure 86: Steric energies of the C (left), nucleophile (center) and leaving group (right) along the self-substitution reactions with different halogens.

5.4 Reaction Force and Activation Energies

The reaction force is defined[6] as :

$$F(\xi) = -\frac{dV(\xi)}{d\xi}, \tag{2}$$

where ξ is the intrinsic reaction coordinate and V the potential energy profile of the reaction.

The reaction force was computed by means of two-point numerical differentiation as follows :

$$F(\xi') = -\frac{\Delta E(\xi)}{\Delta \xi} = -\frac{E(\xi^b) - E(\xi^a)}{\xi^b - \xi^a}, \tag{3}$$

The following figures show the evolution of the reaction force in our reactions.

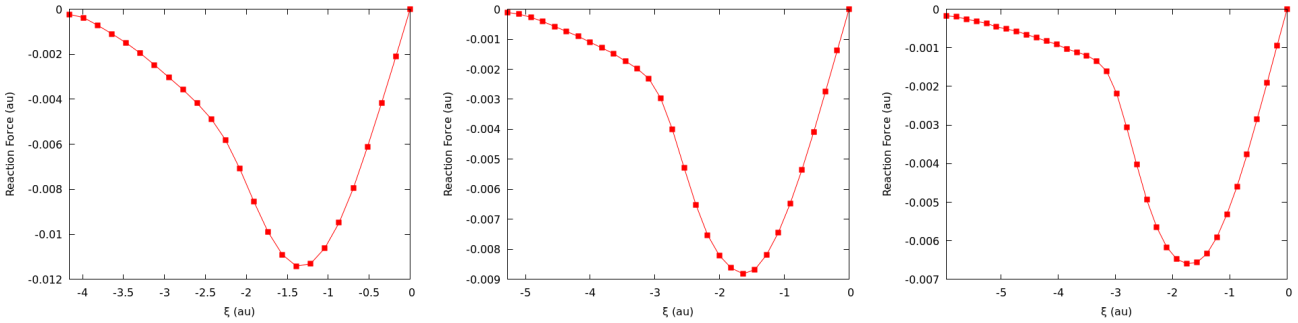

Figure 87: Reaction force along the forward part of the IRC paths (M062X/aug-cc-pVDZ) for the gas phase self-substitution reaction of CH_3X for X = F (left), Cl (center), Br (right).

Although all the reactions proceed in one step, clear processes taking place which can be identified by the different trends experienced by the reaction force along the chemical transformation. Initially, the attacking halogen approaches the reactive electrophilic center, a stage which is characterized by a quasi-linear change in the reaction force. This "preparation step" is followed by the actual bond breaking and formation process during which a strong deformation of the local geometry of the electrophile occurs.

The following table collects the activation energies for the self-substitution reaction of the different halo-methanes (CH_3X) computed at the M06-2X/aug-cc-pVDZ level of theory in the gas phase:

Halogen	$\Delta E^{\ddagger}$ (kcal/mol)	C-X distance (Å)	Q (au)
F	14.12	1.800	-0.775
Cl	12.52	2.308	-0.699
Br	9.86	2.461	-0.667

Table 6: Activation energy, C-X distance at the transition state and charge of the leaving group and nucleophile Q at the TS structure. The activation energies are purely electronic, lacking any thermal correction.

5.5 Activation Strain Model (ASM) calculations

The Activation Strain Model (ASM) as developed by Bickelhaupt and co-workers[7] is a model used to analyze the different contributions to the total potential energy of a system along the progress of a chemical reaction on the basis of chemically meaningful terms. Under this scheme, the total reaction energy is decomposed into strain, E_{str}, and interaction, E_{int}, components at any point along the reaction coordinate (ξ) as:

$$\Delta E(\xi) = \Delta E_{str}(\xi) + \Delta E_{int}(\xi) \tag{4}$$

The first term, E_{str}, accounts for the energetic cost associated to taking the isolated interacting fragments at their equilibrium geometries to those found in the reacting system at each ξ. The second leads to the total ΔE, and thus accounts for all possible relaxation and interaction processes. In order to perform the ASM analysis, a set of single

point calculations were performed on the reactants, defined as nucleophile (X^-) and electrophile (CH_3X), at the frozen geometry found at each of the points of the IRC calculations. From such calculations, the E_{str} was computed and the E_{int} was consequently reconstructed from the total potential energy. All the reported magnitudes are given as relative values referenced with respect to the starting reactive complex structure.

The following figures show the evolution of the E_{str} and E_{int} contributions in our reactions.

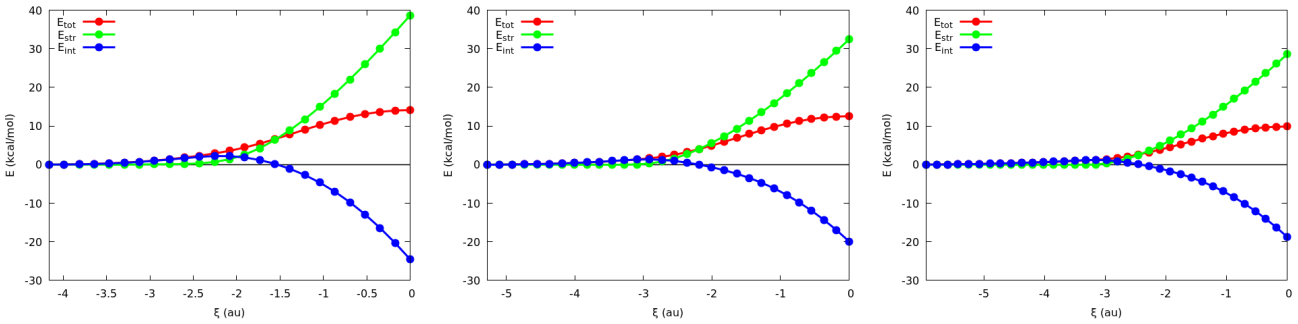

Figure 88: Evolution of the strain, E_{str}, and interaction, E_{int}, components to the total potential energy along the progress of the self-substitution reactions of CH_3X with X^- for X = F (left), Cl (center), Br (right). Since the reaction profile is symmetric with respect to the TS, only the forward part of the reaction is shown. Calculations performed at the M062X/aug-cc-pVDZ level of theory in the gas phase.

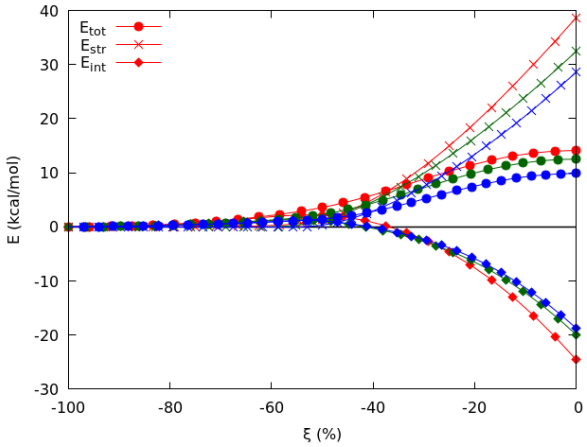

Figure 89: Comparison of the E_{str} and E_{int} along the reaction coordinate for the self-substitution processes under study with X = F (blue), Cl (green) and Br (violet). Calculations performed at the M062X/aug-cc-pVDZ level of theory in the gas phase.

As it can be seen from the previous figures, the behavior exhibited by the total potential energy along the reaction coordinate arises from the interplay of the drastically different E_{str} and E_{int} contributions. On a general basis, along the preparation stage of the reaction, both the interaction E_{int} and E_{str} are relatively small, being the former term slightly more dominating than the later. Such an smooth and slowly varying trend in the energetic components changes from this point forward. More specifically, as the reactants get deformed, the strain, E_{str}, energy increases exponentially resulting in a significant energetic penalty along the reaction which is partially counteracted by the stabilizing E_{int} term arising from the interaction between the nucleophile (X^-) and the electrophile (CH_3X). Overall, the slightly more dominating character of the destabilizing energy contribution associated with the deformation suffered by the reagents after the preparation step leads to the overall behavior observed in the reaction energy profile. These results are, in general, in good agreement with already reported data [8,9]. Moreover, as it can be seen from figure 89, the decrease observed in the activation energies for the substitution reactions along the halogen series can be mainly attributed to the decrease in the total E_{str} experienced by the system along the reaction, something which is partially counteracted by the decrease of the stabilizing contribution associated to the interaction term. These trends can also be rationalized attending to the progressively increasing C-X bond distance of the CH_3X

moiety as the X = F, Cl, Br series proceeds, which would involve a considerably smaller geometrical deformation on going from the reactants to the activated complex structure and consequently a lower strain penalty.

Though the ASM analysis (as used so far in this work) provides chemically meaningful information of a reaction profile and its mechanism at a low computational cost, slightly more complex approximations can be implemented. More specifically, energetic decomposition or partition schemes can be used to further divide the different ASM components. Such an approach has been extensively used in combination with energy decomposition analysis (EDA) strategies[7–11] which are commonly employed to decompose the interaction term ,E_{int}, as follows :

$$E_{int} = \Delta E_{elst} + \Delta E_{Pauli} + \Delta E_{orb} \tag{5}$$

Where the E_{elst} term represents the electrostatic interaction between the interacting moieties and the E_{Pauli} and E_{orb} terms account respectively for the Pauli repulsion and orbital interactions.

The ASM+EDA analysis is prone to a well described and stressed[12–14] problem stemming from the use of non-stationary intermediate in EDA. This arbitrariness can be, however, avoided by using real space partitioning strategies (such as IQA), as already pointed out in one of our recent works.[15] The total energy along the reaction can be reconstructed as :

$$\Delta E = \Delta E_{def} + \Delta E_{int} = \Delta E_{def,geom} + \Delta E_{def,el} + \Delta V_{cl} + \Delta V_{xc} \tag{6}$$

Where E_{def} represents the IQA deformation energy, which can be expressed as a sum of a purely geometrical deformation term $E_{def,geom}$ (analogous to the E_{str} in the ASM model) and an electronic deformation counterpart $E_{def,el}$. On the other hand, the ΔE_{int} term is simply the IQA interaction energy between the interacting fragments which, can be further decomposed into a sum of classical V_{cl} and exchange-correlation V_{xc} contributions.

5.6 Rigid scans

Here we collect the IQA results obtained along the rigid analysis of the model reaction (CH_3F and F^-) computed at the M06-2X/aug-cc-pVDZ level of theory in the gas phase. The following figures show the evolution of the deformation energies, E_{def}, along with their E_{CT} and E_{ST} contributions for the different chemical groups involved in the reaction, both for the frozen and relaxed channels.

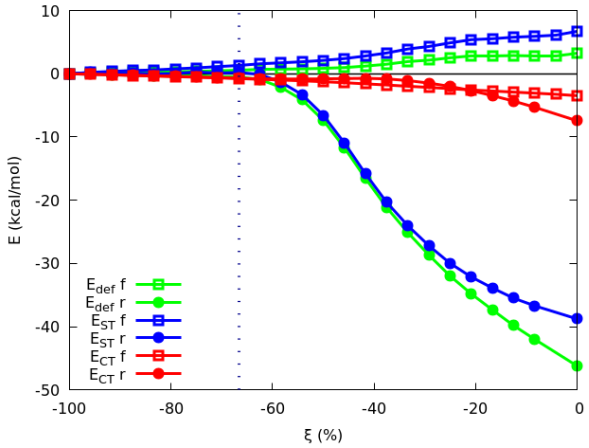

Figure 90: Deformation energy, E_{def}, along with the steric, E_{ST}, and charge transfer, E_{CT}, contributions for the leaving group along the self-substitution reaction of CH_3F and F^-. Calculations done in the gas phase at the M06-2X/aug-cc-pVDZ level of theory. The labels r and f correspond to the relaxed and frozen approximations, respectively.

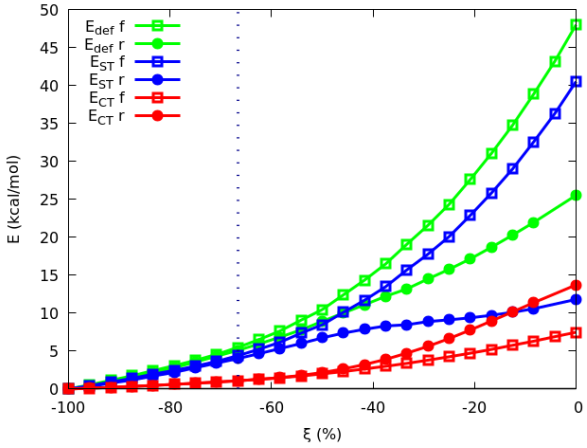

Figure 91: Deformation energy, E_{def}, along with the steric, E_{ST}, and charge transfer, E_{CT}, contributions for the nucleophile along the self-substitution reaction of CH_3F and F^-. Calculations done in the gas phase at the M06-2X/aug-cc-pVDZ level of theory. The labels r and f correspond to the relaxed and frozen approximations, respectively.

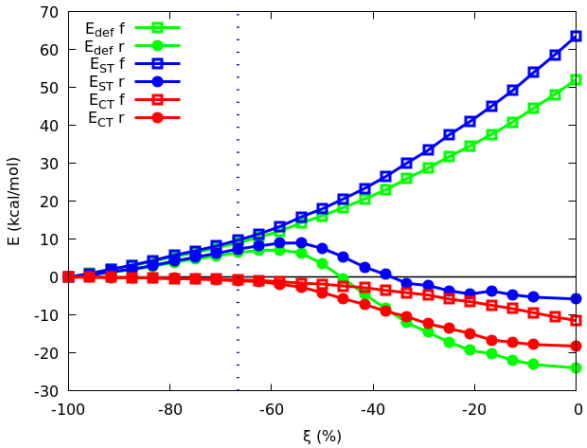

Figure 92: Deformation energy, E_{def}, along with the steric, E_{ST}, and charge transfer, E_{CT}, contributions for the methyl moiety along the self-substitution reaction of CH_3F and F^-. Calculations done in the gas phase at the M06-2X/aug-cc-pVDZ level of theory. The labels r and f correspond to the relaxed and frozen approximations, respectively.

The results obtained for the frozen approximation channel agree reasonably well with the ones corresponding to the relaxed reaction path during the preparation stage. Such a result indicates that in this first stage of the reaction only minor structural changes in the local geometry of the haloalkane take place. From this point on, the results of the relaxed and frozen approximations differ due to the large geometrical changes undergone by the reactive species. Regarding the leaving group (L), both the E_{def} and the E_{ST} terms decay significantly after the preparation stage, something which can be attributed to the relaxation associated with the C-F bond breaking process. These results contrast obviously with the ones obtained in the frozen scan, for which both the E_{def} and E_{ST} increase slightly as a result of the compression of the attacking F atom and the lack of relaxation associated to the C-F rupture. An analogous trend can be observed for the nucleophile, for which the frozen scans yield much larger deformation and steric energies as a result of the compression against the rigid halomethane. These compression is partially counteracted in the fully relaxed reaction as a result of the planarization of the methyl moiety, which reduces the deformation experienced by the attacking atom in comparison with the frozen approximation. Furthermore, both the E_{def} and E_{ST} of the methyl group slowly decrease after the initial stage. Such a behavior can be considered the result of the interplay between the energy penalty of the compression with the attacking halide atom and the relaxation due to planarization. Finally, it is interesting to notice that the steric and deformation energies of the groups being directly compressed (the CH_3 and the nucleophile groups) computed in the frozen scan increase exponentially along the progress of the reaction, following a similar trend to the one obtained for the rigid compression of the dimeric systems.

6 Cartesian coordinates of relevant structures

6.1 Methane (CH_4) monomer

Atom	X	Y	Z
C	0.00000	0.00000	0.00000
H	0.63338	0.63338	0.63338
H	-0.63338	-0.63338	0.63338
H	0.63338	-0.63338	-0.63338
H	-0.63338	0.63338	-0.63338

Table 7: Energetically minimized geometry of the methane monomer (CH_4) in the gas phase computed at the B3LYP/aug-cc-pVDZ level of theory. Coordinates in Å.

6.2 Ammonia (NH_3) monomer

Atom	X	Y	Z
N	0.00000	0.00000	0.11474
H	0.00000	0.94398	-0.26772
H	0.81751	-0.47199	-0.26772
H	-0.81751	-0.47199	-0.26772

Table 8: Energetically minimized geometry of the ammonia monomer (NH_3) in the gas phase computed at the B3LYP/aug-cc-pVDZ level of theory. Coordinates in Å.

6.3 SN2 reaction between CH_3F and F^- at the HF/aug-cc-pVDZ

Atom	X	Y	Z
C	0.46212100	0.00027600	0.00010800
F	-2.16266400	-0.00197900	-0.00132000
H	0.14809100	-0.46583300	-0.91006800
H	0.13584300	-0.55566100	0.86115600
H	0.12411300	1.02627100	0.05171200
F	1.87464800	-0.00219500	-0.00138200

Table 9: Energetically minimized geometry of the reactant complex for the reaction between CH_3F and F^- in the gas phase computed at the HF/aug-cc-pVDZ level of theory. Coordinates in Å.

Atom	X	Y	Z
C	0.00003800	-0.00012400	-0.00006600
F	-1.84814600	0.00006000	0.00002700
H	0.00051600	-0.48685900	-0.94972800
H	0.00022000	-0.57941200	0.89613400
H	-0.00015300	1.06563700	0.05334500
F	1.84805600	0.00009300	0.00004500

Table 10: Energetically minimized geometry of the transition state complex for the reaction between CH_3F and F^- in the gas phase computed at the HF/aug-cc-pVDZ level of theory. Coordinates in Å.

Atom	X	Y	Z
C	-0.46223600	0.00086600	0.00026200
F	-1.87794500	0.00327600	0.00177600
H	-0.11975500	-0.46806100	-0.91501300
H	-0.13003400	-0.55602000	0.86192300
H	-0.14577200	1.02220900	0.05136700
F	2.16068900	0.00264800	0.00127900

Table 11: Energetically minimized geometry of the product for the reaction between CH_3F and F^- in the gas phase computed at the HF/aug-cc-pVDZ level of theory. Coordinates in Å.

6.4 SN2 reaction between CH_3F and F^- at the B3LYP/aug-cc-pVDZ

Atom	X	Y	Z
C	0.41226100	0.00012500	0.00010200
F	-2.14359000	-0.00022800	-0.00014800
H	0.07504700	-0.47293800	-0.92281100
H	0.07511900	-0.56262800	0.87126600
H	0.07510200	1.03594800	0.05188600
F	1.87124300	0.00012900	0.00006600

Table 12: Energetically minimized geometry of the reactant complex for the reaction between CH_3F and F^- in the gas phase computed at the B3LYP/aug-cc-pVDZ level of theory. Coordinates in Å.

Atom	X	Y	Z
C	0.00000005	-0.00011970	0.00001239
F	-1.85256195	-0.00008170	-0.00007561
H	0.00008405	-0.49224270	-0.96046761
H	0.00001105	-0.58585070	0.90645539
H	-0.00007895	1.07771630	0.05403839
F	1.85256105	0.00017730	0.00006639

Table 13: Energetically minimized geometry of the transition state complex for the reaction between CH_3F and F^- in the gas phase computed at the B3LYP/aug-cc-pVDZ level of theory. Coordinates in Å.

Atom	X	Y	Z
C	-0.41224400	0.00006800	0.00007100
F	-1.87122800	-0.00013200	-0.00007800
H	-0.07489600	-0.47295000	-0.92281700
H	-0.07509400	-0.56263700	0.87126100
H	-0.07523700	1.03593900	0.05187900
F	2.14356300	0.00007100	0.00001600

Table 14: Energetically minimized geometry of the product for the reaction between CH_3F and F^- in the gas phase computed at the B3LYP/aug-cc-pVDZ level of theory. Coordinates in Å.

6.5 SN2 reaction between CH_3F and F^- at the M06-2X/aug-cc-pVDZ

Atom	X	Y	Z
C	0.40799000	0.00011500	0.00001400
F	-2.10820800	0.00003800	0.00027200
H	0.05926000	0.39584600	0.95376200
H	0.05874400	0.62820800	-0.81937500
H	0.05843700	-1.02346100	-0.13405700
F	1.84114900	-0.00014200	-0.00029900

Table 15: Energetically minimized geometry of the reactant complex for the reaction between CH_3F and F^- in the gas phase computed at the M06-2X/aug-cc-pVDZ level of theory. Coordinates in Å.

Atom	X	Y	Z
C	-0.00000023	-0.00018869	0.00008575
F	-1.80041823	0.00005331	-0.00004725
H	-0.00000123	0.41334931	0.99875975
H	-0.00000223	0.65852431	-0.85675825
H	-0.00000423	-1.07163669	-0.14124125
F	1.80041877	0.00005331	-0.00004725

Table 16: Energetically minimized geometry of the transition state complex for the reaction between CH_3F and F^- in the gas phase computed at the M06-2X/aug-cc-pVDZ level of theory. Coordinates in Å.

Atom	X	Y	Z
C	-0.40798400	0.00011600	0.00001400
F	-1.84114200	-0.00014100	-0.00029900
H	-0.05925400	0.39584600	0.95376200
H	-0.05873800	0.62820900	-0.81937500
H	-0.05843100	-1.02346000	-0.13405900
F	2.10819600	0.00003600	0.00027200

Table 17: Energetically minimized geometry of the product for the reaction between CH_3F and F^- in the gas phase computed at the M06-2X/aug-cc-pVDZ level of theory. Coordinates in Å.

6.6 SN2 reaction between CH_3Cl and Cl^- at the M06-2X/aug-cc-pVDZ

Atom	X	Y	Z
C	0.52480800	0.00239400	0.00023400
Cl	-2.55411300	-0.00232000	-0.00041900
H	0.18656700	-0.47120700	-0.91962600
H	0.18640200	-0.55713500	0.87042800
H	0.18739700	1.03614100	0.04989600
Cl	2.35786800	0.00127400	0.00031800

Table 18: Energetically minimized geometry of the reactant complex for the reaction between CH_3Cl and Cl^- in the gas phase computed at the M06-2X/aug-cc-pVDZ level of theory. Coordinates in Å.

Atom	X	Y	Z
C	0.00000131	0.00276173	0.00005435
Cl	-2.30769369	-0.00070927	-0.00007965
H	0.00005431	-0.48965627	-0.96018865
H	0.00000431	-0.58322427	0.90620335
H	-0.00006069	1.08061173	0.05407735
Cl	2.30769331	-0.00046127	0.00005835

Table 19: Energetically minimized geometry of the transition state complex for the reaction between CH_3Cl and Cl^- in the gas phase computed at the M06-2X/aug-cc-pVDZ level of theory. Coordinates in Å.

Atom	X	Y	Z
C	-0.52480800	0.00230500	0.00019700
Cl	-2.35786800	0.00102400	0.00018200
H	-0.18647400	-0.47125600	-0.91965000
H	-0.18640000	-0.55720200	0.87040400
H	-0.18749000	1.03608100	0.04988900
Cl	2.55411200	-0.00203500	-0.00026800

Table 20: Energetically minimized geometry of the product for the reaction between CH_3Cl and Cl^- in the gas phase computed at the M06-2X/aug-cc-pVDZ level of theory. Coordinates in Å.

6.7 SN2 reaction between CH_3Br and Br^- at the M06-2X/aug-cc-pVDZ

Atom	X	Y	Z
C	0.55158300	-0.00802400	-0.00207900
Br	-2.63273100	0.00146500	0.00015400
H	0.23049000	-0.47956200	-0.92824100
H	0.22868300	-0.57557000	0.86786400
H	0.22291100	1.02731700	0.05307600
Br	2.54014900	0.00011000	0.00025500

Table 21: Energetically minimized geometry of the reactant complex for the reaction between CH_3Br and Br^- in the gas phase computed at the M06-2X/aug-cc-pVDZ level of theory. Coordinates in Å.

Atom	X	Y	Z
C	0.00000091	-0.00872062	-0.00023248
Br	-2.46105909	0.00073138	-0.00004448
H	0.00005091	-0.50260662	-0.96032748
H	0.00000591	-0.59611962	0.90579652
H	-0.00005409	1.06922538	0.05392952
Br	2.46105891	0.00097138	0.00008752

Table 22: Energetically minimized geometry of the transition state complex for the reaction between CH_3Br and Br^- in the gas phase computed at the M06-2X/aug-cc-pVDZ level of theory. Coordinates in Å.

Atom	X	Y	Z
C	-0.55157300	-0.00802000	-0.00210600
Br	-2.54014100	-0.00014100	0.00011700
H	-0.23036900	-0.47952000	-0.92824800
H	-0.22864900	-0.57552300	0.86785500
H	-0.22303800	1.02736400	0.05306300
Br	2.63272100	0.00171400	0.00029700

Table 23: Energetically minimized geometry of the product for the reaction between CH_3Br and Br^- in the gas phase computed at the M06-2X/aug-cc-pVDZ level of theory. Coordinates in Å.

7 Ionization potentials

The following table collects the ionization potentials of the different atoms involved in the study, computed at different levels of theory.

Atom	Methodology	Initial	Final	IP (kcal/mol)	IP_{exp} (kcal/mol)
C	HF/aug-cc-pVDZ	C (0)	C (+1)	+249.08	+259.93
C	B3LYP/aug-cc-pVDZ	C (0)	C (+1)	+265.24	+259.93
C	M062X/aug-cc-pVDZ	C (0)	C (+1)	+260.66	+259.93
H	HF/aug-cc-pVDZ	H (0)	H (+1)	+313.34	+313.88
H	B3LYP/aug-cc-pVDZ	H (0)	H (+1)	+314.79	+313.88
H	M062X/aug-cc-pVDZ	H (0)	H (+1)	+312.44	+313.88
H	HF/aug-cc-pVDZ	H (-1)	H (0)	-7.87	+17.41
H	B3LYP/aug-cc-pVDZ	H (-1)	H (0)	+20.45	+17.41
F	HF/aug-cc-pVDZ	F (-1)	F (0)	+32.14	+78.51
F	B3LYP/aug-cc-pVDZ	F (-1)	F (0)	+83.05	+78.51
F	M062X/aug-cc-pVDZ	F (-1)	F (0)	+74.74	+78.51
Cl	M062X/aug-cc-pVDZ	Cl (-1)	Cl (0)	+84.57	+83.39
Br	M062X/aug-cc-pVDZ	Br (-1)	Br (0)	+81.56	+77.64
N	HF/aug-cc-pVDZ	N (-1)	N (0)	-46.45	+1.63
N	B3LYP/aug-cc-pVDZ	N (-1)	N (0)	+4.94	+1.63
N	HF/aug-cc-pVDZ	N (-2)	N (-1)	-204.23	–
N	B3LYP/aug-cc-pVDZ	N (-2)	N (-1)	-153.8	–

Table 24: Ionization potentials for the different species involved in the calculations evaluated at different levels of theory

The estimated IPs are in reasonable agreement with the values reported in the literature. It is worth to mention, however, that the errors committed in the estimation of the IPs involving anionic species are significantly greater than those corresponding to proper cationic species (with respect to the neutral atom), something which is even more pronounced for the IPs computed at the HF level of theory. Such a result can be attributed to the well known limitations of the HF theory in the evaluation of electron affinities (the orbital relaxation errors and the lack of electron correlation are additive and do not generally cancel each other as for the case of ionization potentials (IP)).Experimental values were obtained from the literature[16].

References

[1] A. Martín Pendás and E. Francisco, *Promolden. A QTAIM/IQA code (Avaliable from the authors upon request).*

[2] A. Heßelmann and G. Jansen, *Phys. Chem. Chem. Phys.*, 2003, **5**, 5010–5014.

[3] Q. Sun, T. C. Berkelbach, N. S. Blunt, G. H. Booth, S. Guo, Z. Li, J. Liu, J. D. McClain, E. R. Sayfutyarova, S. Sharma, S. Wouters and G. K. Chan, *PySCF: the Python based simulations of chemistry framework*, 2017, https://onlinelibrary.wiley.com/doi/abs/10.1002/wcms.1340.

[4] J. Laerdahl and E. Uggerud, *Int. J. Mass Spectrom.*, 2002, **214**, 277–314.

[5] M. J. Frisch, G. W. Trucks, H. B. Schlegel, G. E. Scuseria, M. A. Robb, J. R. Cheeseman, G. Scalmani, V. Barone, B. Mennucci, G. A. Petersson, H. Nakatsuji, M. Caricato, X. Li, H. P. Hratchian, A. F. Izmaylov, J. Bloino, G. Zheng, J. L. Sonnenberg, M. Hada, M. Ehara, K. Toyota, R. Fukuda, J. Hasegawa, M. Ishida, T. Nakajima, Y. Honda, O. Kitao, H. Nakai, T. Vreven, J. A. Montgomery, Jr., J. E. Peralta, F. Ogliaro, M. Bearpark, J. J. Heyd, E. Brothers, K. N. Kudin, V. N. Staroverov, R. Kobayashi, J. Normand, K. Raghavachari, A. Rendell, J. C. Burant, S. S. Iyengar, J. Tomasi, M. Cossi, N. Rega, J. M. Millam, M. Klene, J. E. Knox, J. B. Cross, V. Bakken, C. Adamo, J. Jaramillo, R. Gomperts, R. E. Stratmann, O. Yazyev, A. J. Austin, R. Cammi, C. Pomelli, J. W. Ochterski, R. L. Martin, K. Morokuma, V. G. Zakrzewski, G. A. Voth, P. Salvador, J. J. Dannenberg, S. Dapprich, A. D. Daniels, O. Farkas, J. B. Foresman, J. V. Ortiz, J. Cioslowski and D. J. Fox, *Gaussian 09 Revision E.01*, Gaussian Inc. Wallingford CT 2009.

[6] P. Politzer, A. Toro-Labbé, S. Gutiérrez-Oliva, B. Herrera, P. Jaque, M. C. Concha and J. S. Murray, *J. Chem. Sci.*, 2005, **117**, 467–472.

[7] I. Fernández and F. M. Bickelhaupt, *Chem. Soc. Rev.*, 2014, **43**, 4953–4967.

[8] J. Kubelka and F. M. Bickelhaupt, *J. Phys. Chem. A*, 2017, **121**, 885–891.

[9] L. P. Wolters and F. M. Bickelhaupt, *Wiley Interdiscip. Rev. Comput. Mol. Sci.*, 2015, **5**, 324–343.

[10] W. J. van Zeist and F. M. Bickelhaupt, *Org. Biomol. Chem.*, 2010, **8**, 3118–3127.

[11] F. M. Bickelhaupt and K. N. Houk, *Angew. Chem. Int. Ed.*, 2017, **56**, 10070–10086.

[12] W. H. E. Schwarz and H. Schmidbaur, *Chem. Eur. J.*, 2012, **18**, 4470–4479.

[13] T. Bitter, S. G. Wang, K. Ruedenberg and W. H. E. Schwarz, *Theor. Chem. Acc.*, 2010, **127**, 237–257.

[14] S. G. Wang and W. Schwarz, *Angew. Chem. Int. Ed.*, 2009, **48**, 3404–3415.

[15] J. L. Casals-Sainz, E. Francisco and Á. Martín Pendás, *Z. Anorg. Allg. Chem.*, 2020, **646**, 1062–1072.

[16] *Biochem. Educ.*, 1993, **21**, 109–110.